UNIVERSITY OF GRONINGEN

FACULTY OF SCIENCE AND ENGINEERING

An ALMA archival exploitation of Herbig group I and II protoplanetary disks

Author:
Alexandru-Daniel Taun

Supervisor:
Prof. dr. Inga Kamp

A thesis submitted for the degree of

MSc Astronomy

September 12, 2019

Abstract

In the last years, exoplanet observations have shown a wide variety of planetary systems. Observing and understanding the evolution of protoplanetary disks, the early stages of planet formation, can shed light on the processes that shape this diversity. The first evolutionary track proposed for protoplanetary disks around Herbig Ae/Be stars, the more massive counterparts of T Tauri stars, has been the evolution from a flared disk (Group I) into a flat disk (Group II) through dust settling. However, this scenario has been dismissed since it was found that Group I disks have a large inner cavity while Group II do not, which discards the evolution from a Group I into a Group II. In this thesis, we have defined a sample of dust and gas observations of protoplanetary disks around Herbig Ae/Be stars using the ALMA Archive and measured the outer radii and the fluxes for the continuum and the ^{13}CO line. Fluxes for ^{12}CO and C^{18}O lines were also measured were data was available . After combining information about the stellar parameters from the literature with our results, we attempt a disk taxonomy and distinguish between possible evolutionary tracks. We find that Group I disks span a wide range in radii. We divide them into small Group I ($<$200 AU, 5 disks) and large Group I disks ($>$300 AU, 3 disks), however it is not clear if there is a real distinction between them or our sample is missing the intermediate size Group I disks that would fill in the missing gap. Group II disks (5 disks) are on average smaller ($<$150 AU) with low continuum and CO gas fluxes and span a wide range in ages. We conclude that an evolution from a Group II disk into a small Group I is very unlikely. However, the Group I/II (2 disks) disks which have low scattered light emission (continuous disk, no gap - a Group II feature) show similar features in sub-mm with small Group I disks such as radial extent and continuum and CO fluxes. Since these Group I/II disks are relatively young, we consider a possible evolution from a Group I/II to a small Group I disk through a mechanism that carves an inner cavity (e.g. a planet). Nonetheless, the current sample size and quality of data, especially on Group II disks, is too small to draw at this stage statistically significant conclusions similar to those for T Tauri observations, where we have sample sizes of 100s from various star forming regions.

Acknowledgements

Contents

List of Figures

Chapter 1

Introduction

Since the beginning of humanity, people were drawn to the night skies to answer the questions about their origin and purpose. For many centuries, mythology and astrology were the key to answering these questions, however with time they were dethroned by scientific research, starting from Aristotle's Spherical Earth to Copernicus' Heliocentric model, from Galileo's observations of Jupiter's moons to Kepler's Laws and Newton's Gravity, to the Hubble's Expansion of the Universe and the Big Bang model and recently, the ΛCDM model. All of these discoveries were large steps in our understanding of the universe. None of these would have been possible without the development of theoretical frameworks and technological innovations, such as the telescope, since the timescales and distances of astrophysical objects and processes are tremendous compared to human perception. The universe can be a pretty exotic place with phenomena that we cannot reproduce here on Earth, however there is one concept that connects us and everything around us to distant galaxies and stars, and that is the circle of life. Stars, like humans, are born, live and die. This idea dates back to the 18th century, known as The Solar Nebular Hypothesis, developed by Emanuel Swdenborg and later developed by Immanuel Kant. By now we know that during the formation of the central star, a revolving planetary system is created as well from the remaining material.

To have a better understanding of the planetary system formation, humans have sent numerous probes across our solar system (Voyager, Pioneer, Rosetta etc.), however we are limited since we can only observe our solar system as it is now and not how it formed. On this day there are thousands of exoplanets (4009 confirmed on 08.07.2019, NASA Exoplanet Archive) discovered in hundreds of planetary systems that differ from ours. In order to shed light on different mechanisms of planetary system formation we have to observe the primordial stages of star and planet formation. The aim of this thesis is to determine and analyze properties of two types of protoplanetary disks around intermediate mass stars, using submillimeter data from ALMA. This research will help in understanding if different initial conditions of the protoplanetary disks might result in different planetary systems.

1.1 Star Formation

Star formation begins in molecular clouds present in the Interstellar Medium (ISM). These clouds are dense regions with sizes of a few parsecs and consist mostly of hydrogen and helium with trace amounts of other atoms and molecules. Dust is present as well in small amounts but it plays a crucial role in the planet formation. From observations and analysis using the SED (Spectral Energy Distribution, plot of energy versus frequency or wavelength of light), this process can be

divided into 5 main phases (see Figure 1.1):

1. **The prestellar core**: When the gas becomes turbulent due to external factors (e.g. shockwaves from supernovae), the balance between gravitational forces pulling inwards and internal pressure pushing outwards is broken and the cloud starts to collapse under its own gravity. The timescale of the collapse depends on the initial density of the cloud and can be approximated to the first order by the free fall timescale:

$$t_{\mathrm{ff}} = (\frac{3\pi}{32G\rho})^{1/2} \tag{1.1}$$

   where G is the gravitational constant and ρ is the density.

2. **Class 0**: Due to conservation of angular momentum, during the collapse of the cloud, a rotating disk of gas and dust will start to appear around the central protostar. During this stage, the protostar is still embedded in the cloud, surrounded by an in-falling envelope, thus not visible yet. These type of objects can be observed through far infrared (FIR) and millimeter wavelength emission from the dust.

3. **Class I**: Matter is still falling onto the protostar from the disk in periodic bursts. During this stage, the protostar also expels matter via bipolar jets and outflows.

4. **Class II**: During this stage, the surrounding gas will be cleared by jets and outflows, reducing the accretion rate onto the pre-main sequence star ($\dot{M}_{\mathrm{acc}} \sim 10^{-7}\,\mathrm{M_\odot yr^{-1}}$). The central pre-main sequence star will be surrounded by an optically thick circumstellar disk which is observed as an IR excess in the SED.

5. **Class III**: In this stage, the gas has been cleared out. The star is dominating the SED and the infrared excess from the dust is no longer present. The dust is present only in the debris disk, ring-like structures where planets are believed to form. At this stage, the star surrounded by the low-mass debris disk or the planetary system, is ready to start hydrogen fusion and join the main-sequence where it will spend most of its lifetime.

Protoplanetary disks are observed in earlier phases as well (Class I [Segura-Cox et al., 2016]), however most of the studies are focused on Class II objects. In earlier stages the accretion rate is higher which causes outflows and jets. These outflows/jets interfere with the observations of protoplanetary disks. There is also another class of disks called transitional disks which represent the objects between Class II and Class III. In these transitional disks, large cavities of around 15 to 75 AU [Espaillat et al., 2014] might be formed by protoplanets which clear the inner regions. If a protoplanetary disk (Class II) shows presence of gaps, it is called a pre-transitional disk.

A pre main sequence star (PMS), depending on the mass, can either be a T Tauri (0.5-1.5 $\mathrm{M_\odot}$) or a Herbig Ae/Be star (1.5-8 $\mathrm{M_\odot}$). Stars more massive than 8 $\mathrm{M_\odot}$ are not visible during their pre-main sequence stage because they quickly contract and start hydrogen fusion while still embedded in the molecular cloud. When they become visible, these massive stars are already main-sequence objects. These classes of objects do not only differ in mass but they also follow distinct evolutionary pathways. The T Tauri star formation and evolution has been thoroughly studied compared to the Herbig Ae/Be stars. In this thesis, I focus on the disks around the Herbig Ae/Be stars.

1.2   The Herbig Ae/Be stars

The Herbig Ae/Be stars are young (<10 Myr) pre-main sequence objects with mass between 1.5-8 $\mathrm{M_\odot}$ and are named after George Herbig [Herbig, 1960] who was the first to systematically study
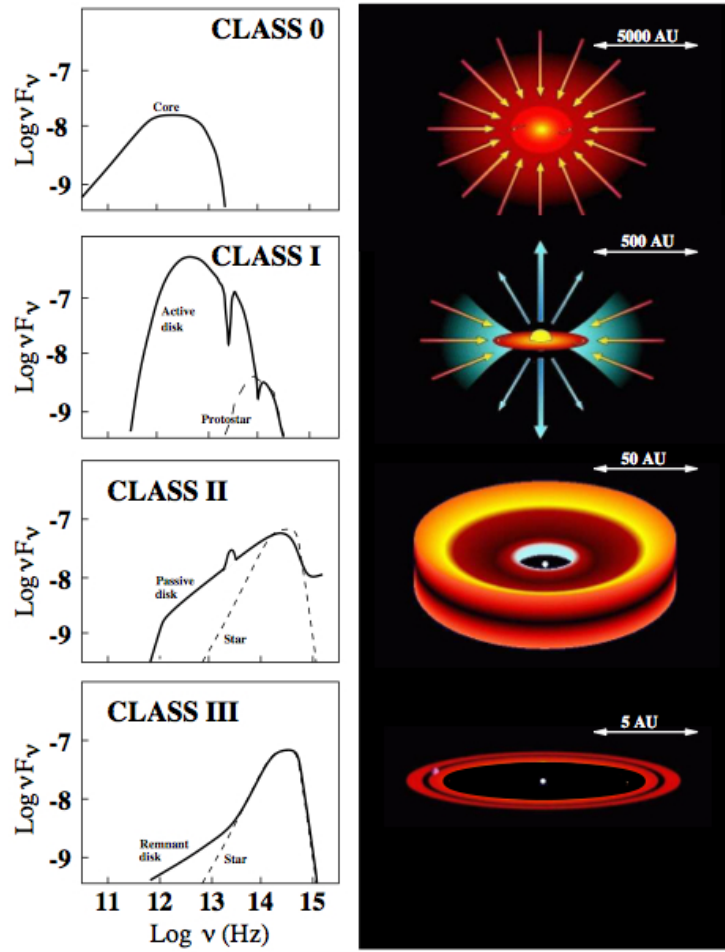
Figure 1.1: A graphical overview of the four stages of protostar evolution taken from Andrea Isella's thesis (2006) [Isella, 2006]. A typical SED of each class is shown in the left column and a schematic of the corresponding geometry is shown in the right column.

this group of objects and empirically defined the main classification criteria: spectral type A or B, Balmer emission lines in the stellar spectrum, IR emission from an accretion/protoplanetary disk heated by the central star and illumination of nearby reflection nebula. Since then, these criteria have been modified, [Waters and Waelkens, 1998] added the luminosity class III to V criterion and several studies [Hu et al., 1991, Oudmaijer et al., 1992, Hillenbrand, 1994, Waelkens et al., 1998] have found isolated Herbig Ae/Be stars, therefore discarding the association with reflection nebulae criterion. Since Herbig Ae/Be stars are more massive than the T Tauri stars, they can only form in large molecular clouds while T Tauri stars can form in both large and small molecular clouds. Therefore, Herbig Ae/Be stars are less numerous and dispersed across the star-forming regions, however their relative proximity (few 100s AU) allows for detailed analysis of their environment. Nowadays, there are almost 300 Herbig Ae/Be stars confirmed. Spectroscopic studies [Meeus et al., 2001, van den Ancker et al., 2000] in the IR have shown a

rich diversity of solid state band such as: silicates (amorphus and crystalline), FeO, crystalline H_2O and polycyclic aromatic hydrocarbons (PAHs), see Figure 1.2. There are also few physical processes that are associated with the Herbig Ae/Be stars, such as bipolar outflows or variability [Sitko et al., 1994, Eiroa et al., 2002, Brittain et al., 2013]. However, the focus of this work will be on protoplanetary disks which I will discuss in the next section.
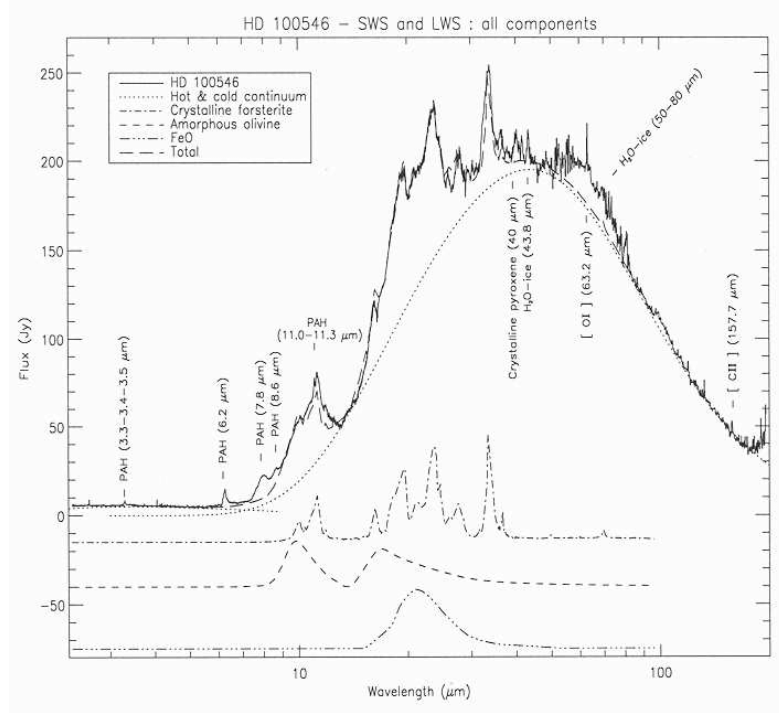
Figure 1.2: Taken from [Brandl and IRS Team, 2001]: ISO-SWS/LWS spectrum of the Herbig Ae star HD 100546 (Malfait et al. 1998). Note the wealth of spectral features including PAHs (polycyclic aromatic hydrocarbons), amorphous and crystalline silicates, rust, etc.

1.3 Protoplanetary Disks

Protoplanetary disks are formed around pre-main sequence stars as a consequence of the conservation of angular momentum in the collapse of the molecular cloud. These disks consist mostly of gas (99%) by mass and only 1% dust. The structure and kinematics of the disk are a consequence of the interplay between the gas and the dust. Even if the dust is not dominating in mass, it still plays an important role in determining the gas and dust temperature across the disk. Due to conservation of angular momentum in the disk, the densities will decrease with radial separation r from the central star [Lynden-Bell and Pringle, 1974, Terebey et al., 1984], while the vertical component of gravity, turbulence and thermal pressure dictate how densities fall off with vertical height from the midplane z [Dubrulle et al., 1995]. In the earlier stages of evolution when the disk is still accreting, viscous heating plays a key role in warming up the midplane of the disk, however in the Class II phase, the accretion rate is low and other mechanisms come into play. The main source of heating in the protoplanetary disk comes from the stellar radiation field, thus

the temperature will decrease with r. The stellar radiation field heats the dust grains in the disk surface layers which then re-emit some of the energy. Part of this energy is emitted deeper into the disk which heats the interior and will result in a thermal inversion, with the midplane being cooler than the surface [Calvet et al., 1991, Chiang and Goldreich, 1997, D'Alessio et al., 1998]. A schematic of a disk structure is shown in Figure 1.3.
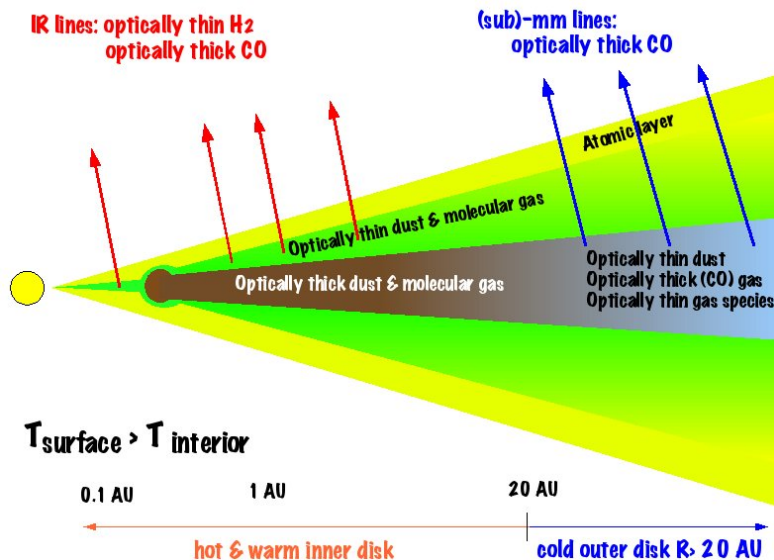
Figure 1.3: Taken from [Carmona, 2010]: Cartoon of the structure of an optically thick disk. The disk has a hot inner region (T>100 K, R<20 AU) and a cold outer region (T<20 K, R>20 AU). Near-IR and mid-IR diagnostics probe the inner disk, (sub)-mm diagnostics probe the outer disk. The disk has a vertical structure: a dense mid-plane and a hotter less dense surface layer. Near-IR and mid-IR gas and dust emission features originate in the optically thin surface layer of the inner disk. Near-IR and mid-IR continuum originates from the optically thick interior layer. At (sub)-mm wavelengths we observe line emission from optically thick CO gas and optically thin emission of cold dust located in the outer disk.

1.3.1 Dust

The grains of dust in the protoplanetary disks are very different from those found in the interstellar medium (ISM). The grains in the ISM are very small with a size distribution starting from ~ 100 Å up to ~ 0.3 μm. These grains are composed of a mixture of silicates and carbons. The same is observed for molecular clouds [Draine, 2003], however major changes occurs to dust in protoplanetary disks since the grains have to grow from micron-sized bodies to meter-sized and eventually to planets. Given this framework, the emission from the dust (continuum) has two contributions: thermal emission from reprocessed stellar light and scattered light reflected by the disk surface. Scattered light is visible in optical and near-infrared and is a powerful diagnostic, however I will not discuss it here since it does not play a role in this research project. The equation that dictates how the dust will emit based on its properties is the radiative transfer

13

equation:

$$dI_\nu = \rho\kappa_\nu(S_\nu - I_\nu)ds \qquad (1.2)$$

where ρ is the density, κ_ν is the (absorption plus scattering) opacity per gram of the solid material and S_ν is the source function. If we recast equation 1.2 in terms of the optical depth defined as $d\tau_\nu = \rho\kappa_\nu ds$, we integrate to get:

$$I_\nu = B_\nu(T)(1 - e^{-\tau_\nu}) \qquad (1.3)$$

Therefore, optically thick emission ($\tau_\nu \gg 1$) will give $I_\nu \sim B_\nu$ while optically thin emission ($\tau_\nu \ll 1$) will give $I_\nu \sim \tau_\nu B_\nu$, in other words the product of temperature, column density and opacity.

The thermal emission of a disk can be divided into two parts: the optically thick hot inner regions probed in the mid/far-infrared and optically thin outer regions probed in the sub-mm/mm. In the SED, the energy density of the thermal emission from the disk will be higher than that of the star starting from >2-5 μm. In this mid/far-infrared regime, the emission is optically thick and the luminosity will probe the temperature of the emitting area and the slope will measure the radial temperature gradient. However, in this project we observe the disks in the sub-mm regime. In this regime the thermal emission from the dust is assumed to be optically thin, therefore the luminosity will scale with $\kappa_\nu B_\nu M_{\text{dust}}$ and the slope measures the shape of the opacity spectrum, as shown in Equation 1.3. An SED of a Herbig Ae/Be star and disk is shown in Figure 1.4.
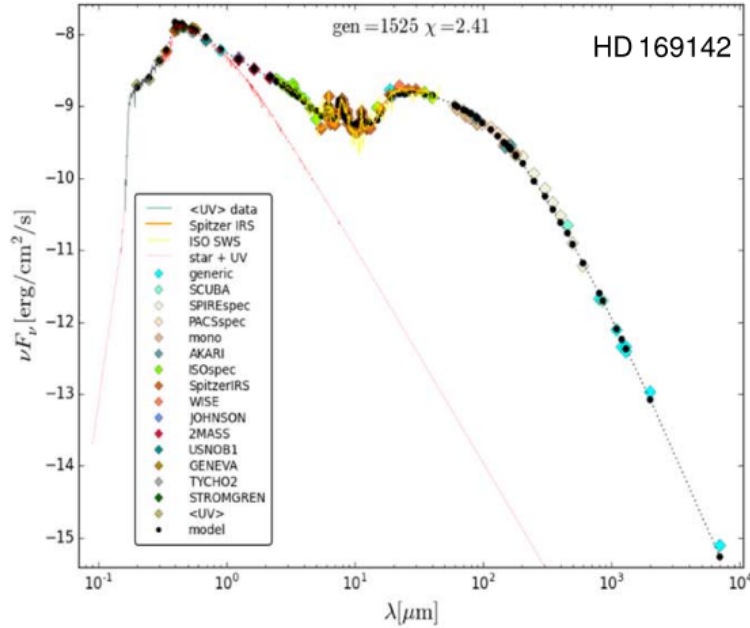
Figure 1.4: Taken from [Woitke et al., 2019], Figure 1: SED of HD 169142 and its disk. The photometric and spectroscopic data points are gathered from various observations as shown in the legend. The red line is the fitted photospheric + UV spectrum of the star and the black dotted line is the disk fit.

14

Since temperature drops with radial separation from the host star, the higher temperatures will be found closer to the star while the outer regions will have lower temperatures (see Figure 1.3). Therefore, the SED will provide a $\lambda \rightarrow r$ mapping. This is shown in Figure 1.5, where near-infrared emission probes the inner 0.1 AU region plus the stellar photosphere. In this regions, the density and the opacity of dust are high resulting in a very optically thick emission. The case for mid-infrared is comparable, only that the scales are larger (few AU). However, this changes for far-infrared emission where the outer parts of the disk can become optically thin, at scales of few tens of AU. For sub-mm/mm emission, the optical depths are low and the emission is optically thin. This probes the midplane on scales of few hundreds of AU making it the perfect tool to analyze the outer regions of the dust disk.

1.3.2 Gas

Temperatures and densities in protoplanetary disks range from 10^4 K and 10^{14} cm^{-3} in the inner (<20 AU) regions to ∼20 K and 10^6 - 10^4 cm^{-3} in the outer (>20 AU) regions resulting in a variety of molecules. Therefore, different molecules and transitions will probe different regions (see Figure 1.3). The gas in the high surface layers interacts with the stellar radiation field and is dissociated, resulting in only atomic gas. The deeper regions will be shielded against the stellar radiation field and therefore will be cooler, down to the midplane where the disk will be fully opaque. Thus, molecules can exist in the midplane but most species are optically thick and their emission lines originate from regions closer to the surface. Molecular hydrogen (H_2) is the most abundant molecule in protoplanetary disks. In the mid-IR, the rotational transitions of H_2 trace gas temperatures of ∼200 K while in near-IR, the ro-vibrational transitions trace the inner, hotter (1000K) regions. However, the issue with H_2 is that it does not have a permanent dipole moment resulting in very weak transitions. For T Tauri disks, the ro-vibrational lines have been detected in a handful of occasions [Bary et al., 2000, Bary et al., 2002, Bary et al., 2003, Carmona et al., 2007], for Herbig AeBe disks however, only in a few cases [Bary et al., 2008, Carmona et al., 2011]. Nonetheless, the H_2 is not a good tracer for the outer disk since it only probes the hot inner regions due to its high excitation energy levels. The second most abundant molecule is carbon monoxide (CO) and because of its many possible transitions, is an exceptional tracer of various disk properties. Firstly, there are the ro-vibrational lines of hot CO which trace the inner disk (<10 AU). Secondly, there are the pure rotational ($\Delta\nu$=0) lines which trace gas temperatures of 50 K to ∼ 1000 K. This includes the higher transitions (J>3) which trace the smaller radii and are detectable from space (from ground up to J=6 in great weather conditions) [Meeus et al., 2001, Meeus et al., 2012, Meeus et al., 2013, van der Wiel et al., 2013], and the low J transitions (J<3) which trace the outer disk and are detectable from the ground at submm/radio wavelengths [Dent et al., 2005, Öberg et al., 2010, Guilloteau et al., 2013]. Therefore, observing and analyzing the entire CO ladder (see Figure 1.6) can be used as a tool to decompose the entire physical structure of the disk.

^{12}CO is a very abundant molecule and cannot be used to probe the midplane or measure the disk mass since its lines become optically thick at the surface of the disk. However, the less abundant CO isotopologues, such as ^{13}CO and C^{18}O, have optically thinner lines and can probe deeper in the disk. For example, since the ^{13}CO is less abundant than ^{12}CO, the ^{13}CO has a lower column density and will reach the sensitivity limit of the observation at a smaller radial separation. Thus, the difference between the two radii will depend on the shape of the density profile (see Figure 1.7). A sharp cut-off in the outer regions will result in a small difference. Measurements of the disk sizes in various isotopologues can be used to understand the slope of the density profile in the outer regions. However, the main issue of using the isotopologues is that the isotope ratio of ^{12}C/^{13}C(∼80) and ^{16}O/^{18}O(∼600) [Wielen and Wilson, 1997] are high
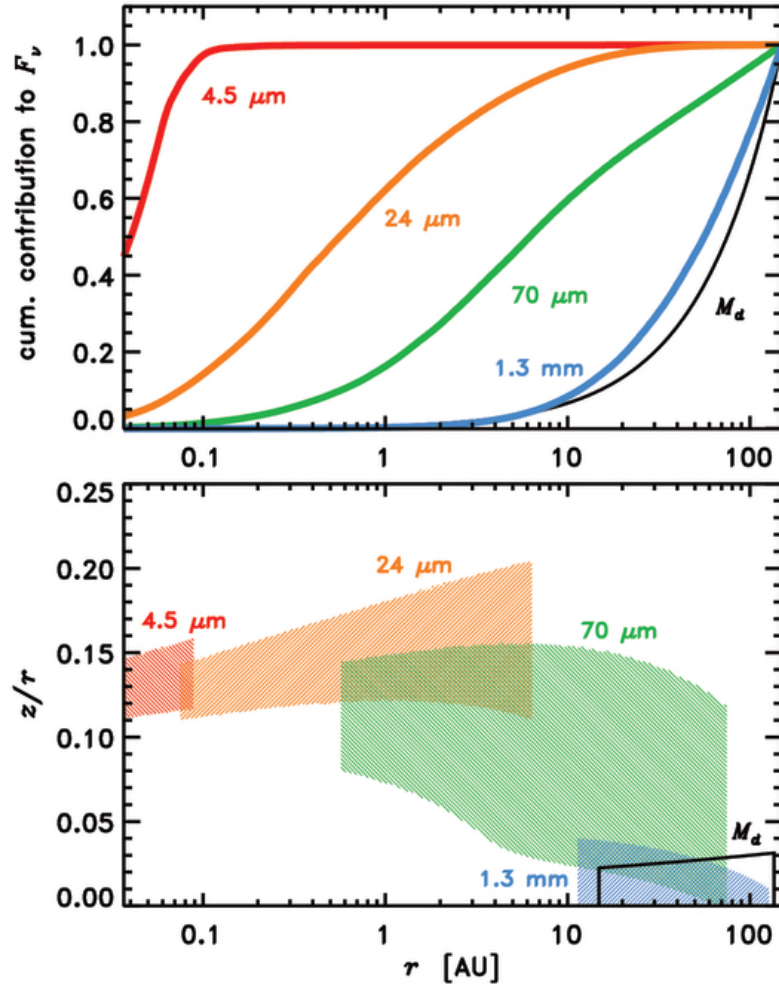
Figure 1.5: Taken from [Andrews, 2015], Figure 3: Top: Cumulative contributions to F_ν at four representative wavelengths as a function of r for the SED model of GO Tau. The cumulative distribution of M_d is also shown (*black curve*). Note that the 4.5 and 24 μm curves are not zero at the inner edge, due to the stellar contribution. Bottom: Two-dimensional map of the regions that emit 80% of the flux (or enclose 0.8 M_d).
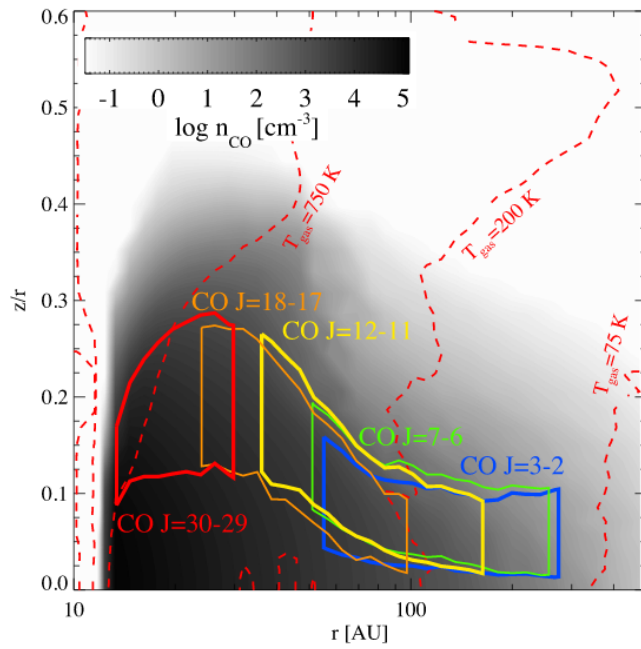
Figure 1.6: Taken from [van der Wiel et al., 2014], Figure 6: Illustration of the origin of several CO rotational lines in a model of the HD 100546 disc. Solid outlines represent areas delimited by the cumulative 15 and 85 per cent line flux contribution of each transition, both vertically and radially. The grey-scale indicates number density of CO molecules. Dashed contours mark gas temperature. The inner disc, at <10 au, is not shown, since it does not contribute significantly to the total amount of line flux from pure rotational transitions of CO.
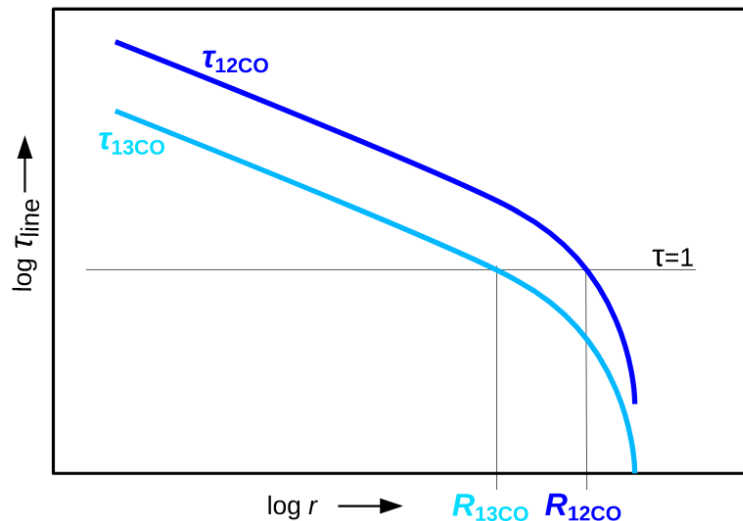
Figure 1.7: Taken from [Woitke et al., 2016], Figure 16: CO isotopologue line ratios. The ^{13}CO line is weaker because it approaches $\tau = 1$ line at smaller radii.

resulting in the abundance of ^{13}CO to be much lower than that of ^{12}CO and the abundance of C^{18}O to be even lower than that of ^{13}CO. In the ALMA Lupus Survey (CO J=2-1) [Ansdell et al., 2018], out of 95 targets, 48 were detected in ^{12}CO, 20 in ^{13}CO and only 8 in C^{18}O. In the ALMA Chamaeleon I Survey (J=3-2) [Long et al., 2017], out of 93 targets, 17 were detected in ^{13}CO and only one in C^{18}O. Observing these isotopologues with ALMA at this moment is a difficult task since it requires very long integration times. In this research, I focus on the CO J=2-1 line in three isotopologues (^{12}CO,^{13}CO & C^{18}O) and I measure the outer gas disk radii using the ^{13}CO line. More details will be given in Section 2.

Measuring the size of a disk seems like a straightforward task to do, however resolved observations have shown the contrary. The apparent size will depend on the tracer used. The early radio interferometric data suggested that line emission from abundant molecules appeared to be spatially extended compared to the continuum emission from dust. Initially, it was believed that limited continuum sensitivity [Dutrey et al., 1998, Guilloteau and Dutrey, 1998] was accountable for the smaller apparent size of the dust disk. Emission lines from molecular gas are optically thick even at large separation from the central star resulting in detectable emission while continuum emission is optically thin, therefore too faint to be observed. With time, the sensitivity of interferometers improved but the discrepancy was still present [Piétu et al., 2005, Piétu et al., 2007, Isella et al., 2007]. This led to the hypothesis that there should be a physical difference in the radial distribution of gas and dust, where the dust-to-gas ratio decreases with radial separation from the host star [Panić and Hogerheijde, 2009, de Gregorio-Monsalvo et al., 2013, Rosenfeld et al., 2013]. The mechanisms that dictate this evolution are discussed in the next section.

1.4 Disk Evolution

Various physical processes affect the structure and kinematics of protoplanetary disks. The gas evolution is affected by the viscous forces and planets that form in the disk. The latter will be

ignored since it only affects the inner regions but also because of simplicity. To understand the gas evolution, one has to solve the viscous equations. [Dominik, 2015b] gives a simple analytic model to compute the time evolution of gas. Assuming a simple axisymmetric disk, the surface density $\Sigma(r,t)$ is the integral of the mass density $\rho_{\mathrm{gas}}(r,z)$ over the disk height z:

$$\Sigma(r,t) = \int_{-\infty}^{+\infty} \rho_{\mathrm{gas}}(r,t,z)dz \qquad (1.4)$$

Using the surface density and the time dependent viscous equation (see [Dominik, 2015a]), we get:

$$\frac{\partial \Sigma}{\partial t} = \frac{3}{r}\frac{\partial}{\partial r}[\sqrt{r}\frac{\partial}{\partial r}(\nu\Sigma\sqrt{r})] \qquad (1.5)$$

where ν is the kinematic viscosity of the gas and r the radial variable. The complete derivation and solution are given in [Dominik, 2015b]. In Figure 1.8, the gas surface density is plotted as a function of radius for different time steps. It can be seen that the disk dissipates in time and grows in size. However, when observing these disks, one has to keep in mind that the column density decreases with time and the observations have limited sensitivity. Thus, it is expected that the observed outer gas disk radii will shrink.
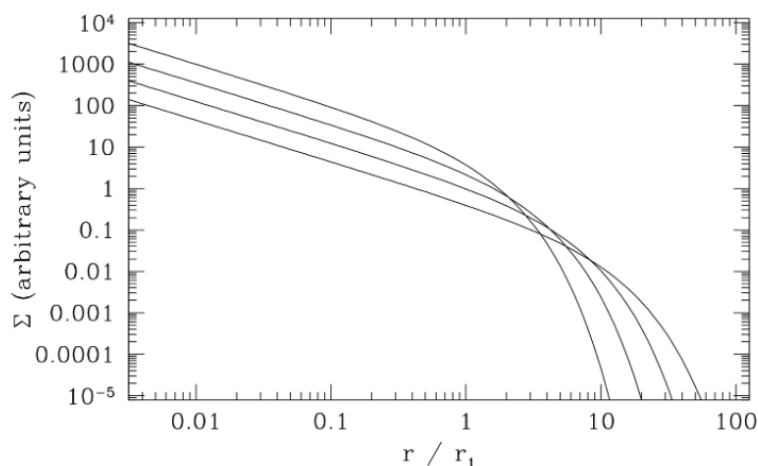
Figure 1.8: Taken from [Armitage, 2010], Figure 3.4: The self-similar solution to the gas disk evolution equation is plotted for a viscosity $\nu \propto r$. The initial surface density tracks the profile for a steady-state disk ($\Sigma \propto r^{-1}$) before cutting off exponentially beyond $r/r_1 = 1$. The curves show the surface density at the initial value of the scaled time variable $\theta=1$ and at subsequent times $\theta=2$, $\theta=4$, and $\theta=8$

.

Even if the gas (99%) dominates the mass budget of the disk, the dust plays a key role in the evolution of the disk. The main mechanisms of dust evolution are dust settling and radial drift. The disks are assumed to be formed with an initial population of small dust grains hydrostatically supported by the gas. The random motions of the dust particles will result in collisions at low speeds. The particles will stick together and form larger grains. The small grains are still hydrostatically supported by the gas while the large grains experience less influence from

19

the gas and will settle towards the midplane [Adachi et al., 1976, Weidenschilling, 1977]. Thus, the density of large grains will increase towards the midplane resulting in an increased collision rate. However, this dust settling and growth process are not entirely efficient. Physical processes such as electrostatic repulsion [Okuzumi, 2009] and bouncing [Zsom et al., 2010] can slow the growth while erosion [Seizinger et al., 2013, Krijt et al., 2015] or fragmentation [Brauer et al., 2008, Birnstiel et al., 2009] can even reverse it. Overall, the processes involved will create a size-layered dust disk with dust-to-gas ratio (ζ) decreasing with vertical distance from the midplane (z).

The other evolutionary mechanism that affects the dust is radial drift. As previously mentioned, the small dust grains are coupled to the gas and will follow its viscous flow. At small radii, the dust will move inwards accreting onto the host star while at large radii it will diffuse and drift outwards. On the other hand, the large grains are not considerably affected by the viscous drag of the gas. In the general picture of a disk, densities and temperature decrease with r resulting in a negative pressure gradient and the gas will rotate with sub-Keplerian velocities. The larger dust grains will feel a drag force which will drain their orbital energy and send them spiraling inwards to the pressure maximum [Whipple, 1972, Adachi et al., 1976, Weidenschilling, 1977]. Therefore, the radial drift will deplete large grains from the outer disk and concentrate them in the inner disk resulting in a dust-to-gas ratio ζ decreasing with r. In Figure 1.9[1] taken from [Andrews, 2015] I present the radial velocity, the surface density and ζ as a function of radial distance for three time steps.

1.5   Group I vs. Group II

Meeus [Meeus et al., 2001] measured the mid/far-IR excess in the SED and found two different types of protoplanetary disks: Group I and Group II SEDs which differ by their mid-IR (15 to 45 μm) slope (see Figure 1.10). They found that in the case of Group II SEDs, the mid-IR excess slope can be fitted by a power-law continuum while Group I SEDs require an additional cold blackbody. Originally, it was thought that the difference comes from dust settling, therefore suggesting that we observe different stages in the evolution of the disk, with Group I being flared disks and when the dust settles, these disks become Group II flat disks [Dullemond and Dominik, 2004]. More recent observations (Q-band resolved images) [Maaskant et al., 2013] have shown that large dust gaps separating the inner and outer disk were present in Group I sources. Introducing the inner cavities in the disk model gives consistent Group I SEDs. The current view on disk geometry interprets Group I disks as being flared disks with large cavities inside and Group II being flatter disks with no inner gap (see Figure 1.11). [Maaskant et al., 2013] also shows two disks, HD 163296 and HD 31648, that have previously been categorized as Group II sources by their mid-IR slope, as being transitional between flaring and flat. This is due to the fact that these disks are resolved in the sub-mm [Sandell et al., 2011] and observed in scattered light [Kusakabe et al., 2012, Wisniewski et al., 2008] with no inner cavities observed. They also show the highest sub-mm excess among the Group II objects. In this thesis we refer to these objects as being Group I/II. Several studies [Blake and Boogert, 2004, Brittain et al., 2007, van der Plas et al., 2014] have investigated the CO ro-vibrational lines in Group I and II disks to find possible differences. These studies have shown that Group I disk might emit CO from further out compared to Group II, however a strong conclusion cannot be drawn from their very small sample size.

---

[1]In the paper by [Andrews, 2015] the term "solids" is used instead of "dust".
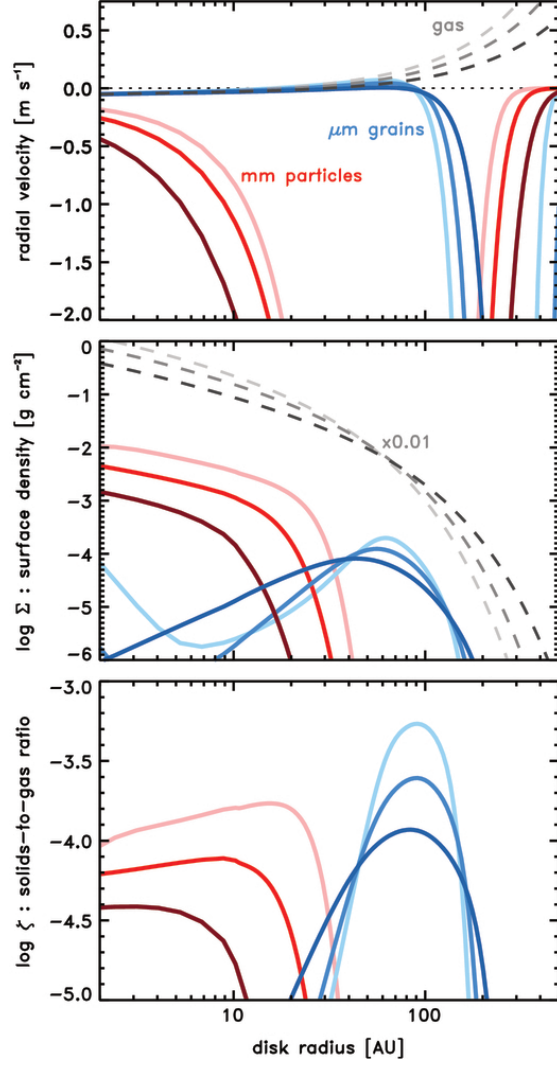
Figure 1.9: Taken from [Andrews, 2015], Figure 15: Demonstration of the evolution of solids embedded in a gas-rich disk. In each panel, gray refers to the gas, blue to approximately micron-sized grains, and red to approximately millimeter-sized particles. Three time steps are shown - 0.5, 1, and 2 Myr (from light to dark). Top: Radial velocities: large negative (inward) motions (up to ~ 0.1 km s^{-1} levels) due to radial drift are noted for millimeter-sized solids at tens of AU. (Middle) Surface densities (Σ): the millimeter solids are radially concentrated and have a relatively sharp "edge" well interior to the gas or small grain distributions. Bottom: Dust-to-gas mass ratio (ζ): a steep drop in ζ for millimeter-sized particles is produced by radial drift.

The recent exoplanets missions have shown a diversity of planetary systems that evolved from various protoplanetary disks. To understand these different evolutionary pathways and the link to the planetary systems, a first step would be to shed light on the taxonomy of protoplanetary disks. In this thesis, we investigate the 1.3mm dust continuum emission and ^{13}CO (J=2-1, 220.39 GHz) line for 15 Herbig AeBe disks (5 Group II, 2 Group I/II and 8 Group I) and
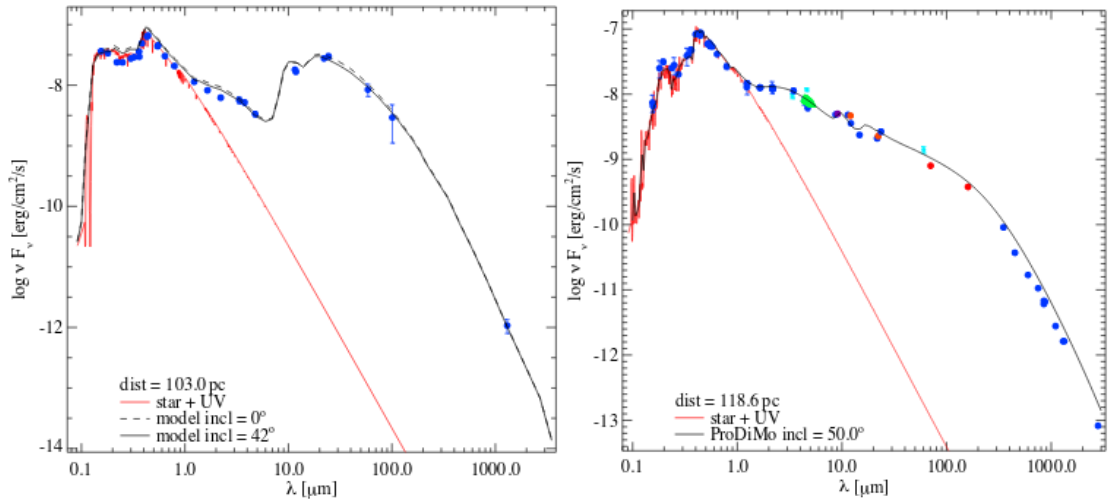
Figure 1.10: Taken from [Hein-Bertelsen, 2015] Figure 1.4: Examples of SEDs from two well studied protoplanetary discs. Left: A disc classified from the SED as group I (HD100546, model and observational points, [Hein Bertelsen et al., 2014]). Right: A disc classified form the SED as group II (HD163296, model and observational points, [Tilling et al., 2012])
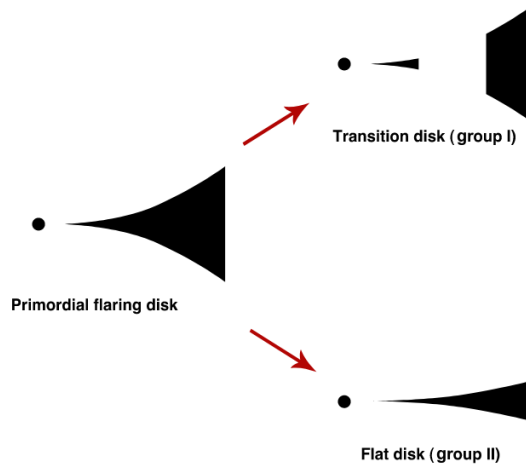
Figure 1.11: Taken from [Maaskant et al., 2013] Figure 11: Sketch of an evolutionary scenario for disk evolution in Herbig Ae/Be objects. Both groups have evolved from a common ancestor (i.e. primordial, possibly embedded, flaring disk structure). In transitional group I objects, gap formation follows the collapse of the outer disk. In group II objects, grain growth and dust settling have flattened the outer disk.

measure the outer radii of dust and gas disks to differentiate between processes that influence the evolution of these objects . In Chapter 2, I present the sample selection and general steps to analyze and measure the outer disk radii, in Chapter 3, I present the results for each individual disk, in Chapter 4, I present various correlations with the disk outer radii and discuss possible evolutionary links between the two Groups and in Chapter 5, I draw the conclusions.

Chapter 2

Data Analysis

2.1 Observations

The observations used for this project were done using the Atacama Large Millimeter/submillimeter Array (ALMA, see Figure 2.1), an interferometer consisting of 66 high-precision radio antennae grouped as follow: 50 antennae of 12-m diameter in the Main Array, 12 antennae of 7-m in the 7-m Array and 4 antennae of 12-m in the Total-Power Array (the latter two groups are known as Morita Array, see Figure 2.1). The antennae can be organized into 10 configurations, resulting in projected baselines ranging from 15 meters to 16 kilometers. ALMA covers the millimeter and submillimeter part of the spectrum, more precisely the wavelength range between 0.32 and 3.6 mm, divided between 8 different bands. The large collecting area, wavelength coverage and high resolving power make ALMA an ideal instrument to observe the distribution of dust and gas in protoplanetary disks down to few AU in spatial resolution. A good example of ALMA's power is the popular image of the disk around HL Tauri (see Figure 2.2), the highest spatial resolution image taken by this array (0.019", corresponding to ≈ 2.7 AU), which showed for the first time, the presence of a multiple ring-like structure in the dust disk.

Figure 2.1: A group of antennas of the Morita Array in ALMA. Credit: ALMA (ESO/NAOJ/N-RAO)

Different ALMA bands cover different specific line transitions from different energy levels in various molecules. Out of all 8 ALMA bands, band 6 turned out to be the most commonly used band for protoplanetary disk dust and gas studies from archival research. ALMA Band 6 is a SIS (Semiconductor-Insulator-Semiconductor) receiver and it was developed and manufactured by the National Radio Astronomy Observatory (NRAO). It covers the 1.1-1.4 mm wavelength range or 211-275 GHz frequency range, optimal for observing J=2-1 line emission of ^{12}CO at 230.538 GHz, ^{13}CO at 220.398 GHz and C^{18}O at 219.560 GHz. The ^{13}CO and C^{18}O J=2-1 line emissions, due to their proximity, can be covered in a single receiver setting.
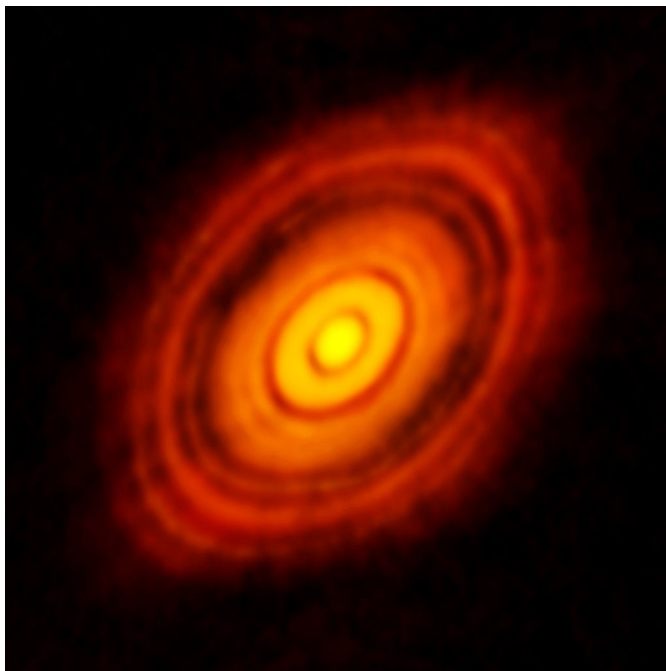
Figure 2.2: The protoplanetary disk surrounding the T Tauri (Class II) star HL Tau. FOV: 0.03 × 0.03 arcminutes, spatial resolution: 0.019 arcseconds , 2014 ALMA Long Baseline Campaign, Credit: ALMA (ESO/NAOJ/NRAO)

2.2   Interferometry

ALMA, like any other interferometer, does not measure directly the brightness of sources. Instead, it measures the interference pattern of all antennas in what is known as the visibility function $V(u,v)$. The visibility function is basically the Fourier transform of the brightness distribution of the source. In Figure 2.3, I present the visibility as a function of baseline for three different sky brightness distributions.

In order to get the real brightness distribution, one would take the visibility function $V(u,v)$ and then Fourier transform back using:

$$I(x,y) = \int_0^\infty \int_0^\infty V(u,v)e^{2\pi i(ux+vy)}dudv \tag{2.1}$$
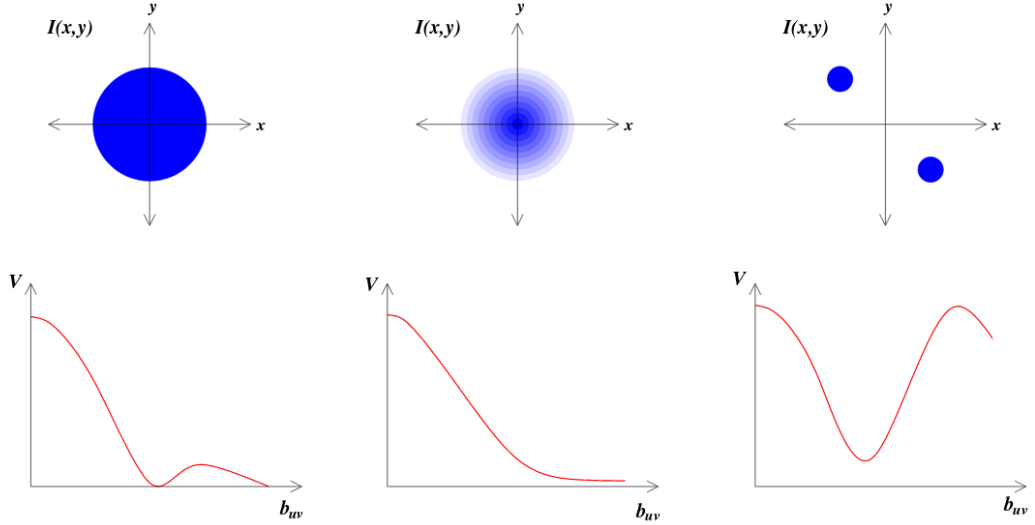
Figure 2.3: Taken from [Ilee and Greaves, 2015] Figure 4: Visibility as a function of baseline for three examples of brightness distributions. *Left*: A uniform disk geometry produces a sinc-like function in visibility, due to the sharp edge of the disk. *Middle*: A Gaussian disk geometry produces a smoothly declining visibility curve. *Right*: A binary source produces a sinusoidal-like visibility curve.

where (x,y) corresponds to the coordinates of the sky brightness distribution, centered on the source, and (u,v) corresponds to the coordinates of the interferometer baseline, measured in units of wavelength for each pair of antennas as seen from the source. However, to get a perfect brightness distribution of the source, the (u,v) plane needs to be fully filled which is never the case. The interferometer is composed of a finite number of antennas that create a finite number of fixed baseline pairs, (u,v) plane points. The not-fully-sampled (u,v) plane can introduce artefacts in the image. To minimize this, different techniques can be used to increase the (u,v) plane sampling. One involves the rotation of the Earth such that the source would rotate with respect to the array, therefore rotating the (u,v) plane as well (see Figure 2.4).

The next step is to calibrate the visibilities using standard objects such as Solar System bodies or quasars. The objects are used to calibrate for non-uniform response across the receiver band and to correct the flux measured by the antennas, but also for effects such as atmospheric variations. After the (u,v) plane is sampled and calibrated, the visibilites are ready to be Fourier transformed into an image. Interferometers are a great tool to achieve the very small angular scales needed to resolve protoplanetary disks. However, since the antennas cannot be placed infinitely close, observations have a smallest baseline which translates into a maximum angular scale beyond which extended sources cannot be resolved anymore. With the aim of measuring the disk sizes, the observations have to be performed in such a way that the angular scale of the disk is between the minimum and maximum angular scale of the observations. If the angular scale of the disk is smaller than the minimum angular scale of the observation, the disk will not be resolved and if it is larger than the maximum angular scale, the disk will be resolved but the large scale emission for the outer parts of the disk will be lost.
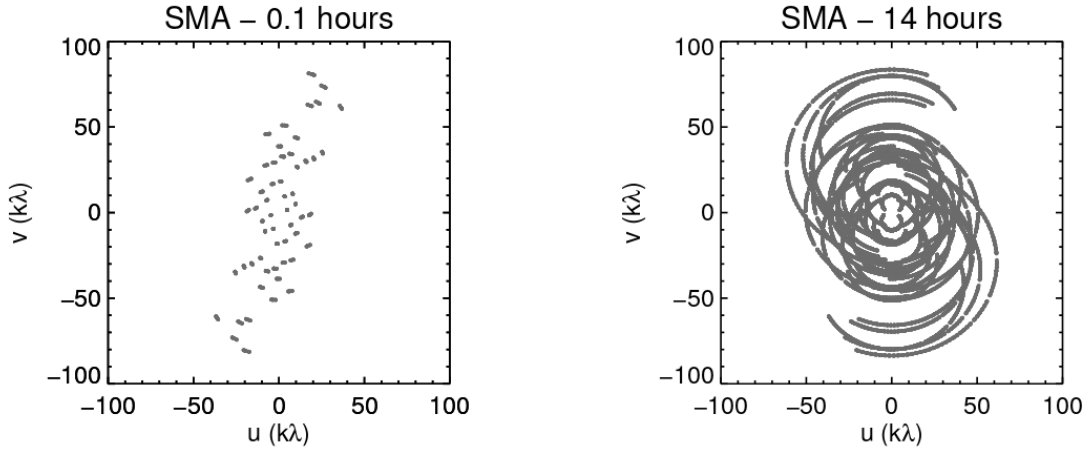
Figure 2.4: Taken from [Ilee and Greaves, 2015] Figure 5: Examples of the (u,v) plane coverage for the Sub-Millimeter Array (SMA). Left: Example of a relatively sparsely sampled (u,v) plane, taken over approximately 5 minutes. Right: Example of a more complete (u,v) coverage, taken over 14 hours, due to the rotation of the Earth. Credits: [Maud et al., 2013].

2.3   Sample

Since the focus of this project is to compare Group I and II disks, the sample needs to be as homogeneous as possible. A list of all observations on Herbig Ae/Be stars available in the ALMA Archive was compiled by R. Upham & O. Panic, which contains information about the band used, wavelength range covered and spatial resolution. Following a thorough analysis of this list in the archive, it was found that most of the observations were done in Band 6. By inspecting the spectral windows used in each observation, it was found that generally, these covered the J=2-1 line transition in the 3 isotopologues of CO: ^{12}CO, ^{13}CO and $C^{18}O$. As mentioned in Chapter 1.3.2, observing the protoplanetary disks in various isotopologues can be used to understand the physical structure of the gas. Hence, observations done in Band 6 covering the 3 isotopologues of CO were selected as an initial sample.

In order to measure the radii, the protoplanetary disks have to be resolved, therefore the sample was narrowed down to observations with spatial resolutions between 20 and 100 AU. These values were chosen to minimize the effects of not resolving sources at low resolution and not detecting outer parts of the disk at high resolution as discussed in Section 2.2. A smaller interval in the spatial resolution could have been chosen to increase the homogeneity of the sample, however the sample size would have been drastically reduced. Nonetheless, the resulted sample size is too small to have a large statistical significance since the amount of ALMA observations of Herbig Ae/Be stars is still limited. In the efforts to enhance the sample size, observations from 2015.1.01600.S (PI: O. Panic) were included which only contain ^{13}CO and $C^{18}O$ observations and have lower spatial resolution on average. In Table 2.1 information about the final sample is presented. The upper half represents the objects with all 3 CO isotopologues observed while the lower half, only the objects with ^{13}CO and $C^{18}O$ observed from 2015.1.01600.S. The quality and size of Group I disks data exceeds the one on GII disks. However, in Chapter 4 I will discuss the results for the sample as a whole and what conclusions we can draw from the limited existing data. In the next section, I will discuss how this data was analyzed.

Object	Project code	Group	Distance (pc)	Beam size ("/AU)	Spectral Resolution ¹³CO (kHz) (km/s)
HD 34282	2015.1.00192.S	I	311.5	0.25 / 77.8	244.17 (0.32)
HD 97048	2015.1.00192.S	I	184.8	0.87 / 160	244.16 (0.32)
HD 163296	2013.1.00601.S	I/II	101.5	0.27 / 27.4	30.52 (0.04)
HD 31648	2016.1.00724.S	I/II	161.7	0.4 & 1.1 / 65 & 178	122.08 (0.16)
HD 169142	2015.1.00490.S	I	113.9	0.19 / 21.7	122.08 (0.16)
HD 100546	2016.1.00344.S	I	110	0.25 / 27.5	244.15 (0.32)
AK Sco	2016.1.00204.S	II	140.6	0.13 / 18.3	61.04 (0.08)
HD 142527	2015.1.01353.S	I	157.3	0.27 / 42.5	122.08 (0.16)
HD 36112	2015.1.01600.S	I	160.2	0.5 / 80	122.07 (0.16)
HD 104237	2015.1.01600.S	II	108.4	1.31 / 142	122.07 (0.16)
HD 142666	2015.1.01600.S	II	148.2	0.95 / 141	122.07 (0.16)
HD 135344B	2015.1.01600.S	I	142.1	0.87 / 124	122.07 (0.16)
HD 139614	2015.1.01600.S	I	134.7	0.75 / 101	122.07 (0.16)
HD 145718	2015.1.01600.S	II	152.5	0.9 / 137	122.07 (0.16)
HD 97048	2015.1.01600.S	I	184.8	0.88 / 163	122.07 (0.16)
HD 100546	2015.1.01600.S	I	110	1.08 / 119	122.07 (0.16)
KK Oph	2015.1.01600.S	II	221	0.6 / 133	122.07 (0.16)

Table 2.1: Sample overview. For Group classification I used [Juhász et al., 2010]. Beam size here refers to the semi-major axis of the gaussian beam (b_{maj}). HD 97048 & HD 100546 appear twice in here because I used both observations, details will be given in the Results section. The distances are Gaia distances, Data release 2 [Gaia Collaboration, 2018].

2.4 Analysis

In this section, I describe all the steps taken to analyze the ALMA data. I only show the general approach and do not present any calculations. These will be presented in the Chapter 4. The examples given here are for illustrative purposes only.

2.4.1 Data reduction

The data reduction took place at Leiden University, ALLEGRO (ALMA Arcnode), under the supervision of L. Guzman and M. Hogerheijde. The first step was to download all the products which includes the final calibrated images and spectral cubes and inspect them. With the exception of AK Sco's ^{13}CO spectral cube, all products were available and the analysis could be performed on them. To get the AK Sco ^{13}CO spectral cube, the raw data was downloaded which comes in the *.asdm* format (ALMA Science Data Model) together with the necessary scripts to get the images. The main script is *scriptForPI.py* which does the entire reduction using various functions and other scripts. Firstly, it loads the raw data and based on information about the atmosphere, antennas, front-ends, connectivity and back-ends (reported by the observers), it returns the *.ms* files (measurement sets). It then runs the *scriptForCalibration.py* and *scriptForFluxCalibration.py* which use the phase and flux calibrator to calibrate the final images. At the end of this step the *.ms* files are calibrated and ready for imaging. To create the images, *scriptForImaging.py* is used. It creates the continuum image which is done by investigating the *.ms* files for line-free channels. The channels with no line emission are added together to create the continuum image. This continuum image is then used by the script to remove the continuum emission from the channels that have line emission. At the end of this processes, the images can be saved as *.fits* files and used for the analysis.

2.4.2 Integrated moment 0 maps

The first step in the analysis was to create the integrated value of the spectrum, in other words, to stack the CO emission from each channel where there was a detection in the image cube. This was achieved by using the CASA (Common Astronomy Software Applications) task: *immoments*. The *immoments* task takes as input the image name, the axis on which to calculate the moments, in this case spectral axis and the channels that contain emission. To find the right channels to compute the moments, I used the spectral profile tool which calculates the total flux for each channel in a circular aperture drawn around the continuum emission. An example is shown in Figure 2.5.

This process was repeated for each object, for all the lines that had a detection. As an example, I show in Figure 2.6 the moment 0 maps of HD 169142 (114 AU [Gaia Collaboration, 2018], i=13° [Raman et al., 2006]), a Group I disk with very clear ring structure [Fedele et al., 2017]. Having created all moment 0 maps, the next step was to devise a method to measure the disks' outer radii.

2.4.3 Flux profiles

Measuring outer radii of extended objects (galaxies, disks, etc.) is a tricky task. The signal at the outskirts gradually blends in with the noise, thus making it impossible to define an edge. Some methods involve fitting a model to the data to extract the outer radius, however the models require a lot of computational power, therefore not efficient to use for large samples. Other techniques involve fitting a model to the data in the uv-plane which is more desirable than fitting in the image plane due to artefacts generated in the imaging process. However, the
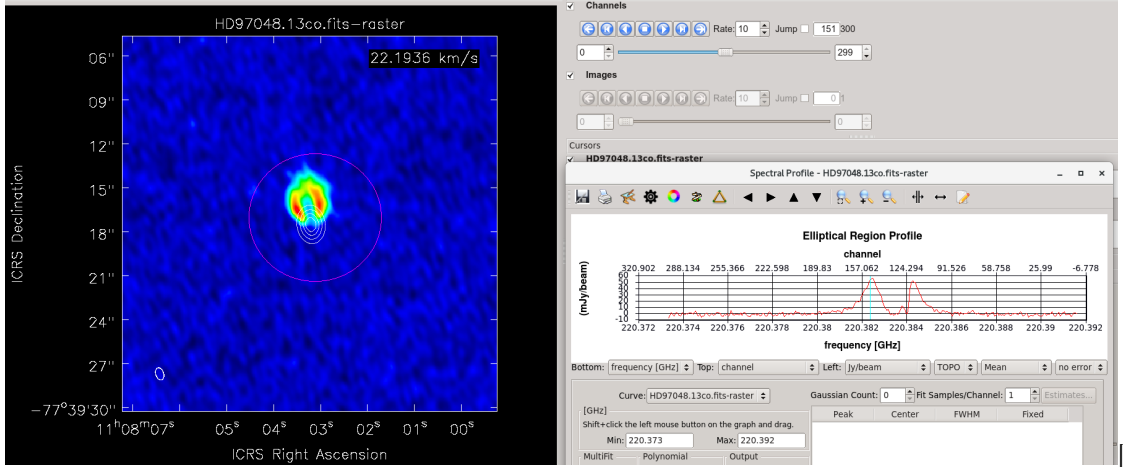
Figure 2.5: Left: Emission from a channel in the ^{13}CO spectral cube of HD 97048. The white contour map is the continuum emission and the red circle is the aperture used by the spectral profile tool; Right: The spectral profile of the HD 97048 ^{13}CO spectral cube.

models in the uv-plane are restricted to a point source, a smooth disk or a Gaussian profile which limits the analysis of more complex disks that show presence of rings and gaps. Nonetheless, objects from the 2015.1.01600.S project were used to compare how a Gaussian fit in the uv-plane compares to a fit in the image plane. It was found that the difference between the two fits is less than 5%, therefore showing that fitting in the image plane is a reliable tool. For this project I adopt a simple but efficient method used by Ansdell et al. (2018), where they measure the outer radii using a curve-of-growth method. On the continuum and CO integrated moment 0 maps, increasingly larger photometric elliptical apertures are applied based on position angle (PA) and inclination (i) of the disk (see Section 3). The flux is measured in each aperture and the outer radius is defined as the radius at which 90% of the maximum flux is measured (F_{90}). The value of 90% is used to enclose most of the dust and gas mass but also to avoid adding noise as described in [Trapman et al., 2019]. The apertures are drawn large enough to enclose all emission. This task was achieved by writing a python script which calculates the cumulative flux distribution as a function of radius. The inputs of this script are: image name, PA, i, central coordinates and distance to the source. The other two parameters which can be tuned are num, number of apertures and $step$, the difference by which the next ellipse is larger than the previous one. The $step$ was tuned to be ≈ 1 AU and num was chosen in such a way that the last aperture would be at a large enough distance so that only noise would be added. As an example, I show in Figure 2.7 the elliptical apertures drawn around the ^{13}CO disk of HD 169142.

The output of the script returns, for each aperture, the semi-major axis of the ellipse in AU, the continuum flux in units of Jy and the line flux in units of Jy km/s. The fluxes are plotted as a function of radius to create the cumulative flux profiles. The profiles of HD 169142 can be seen in Figure 2.8. For illustrative purposes only, the fluxes in continuum, ^{13}CO and C^{18}O are scaled to the level of the ^{12}CO flux. This is due to fact that fluxes of ^{13}CO and C^{18}O are always smaller than the ^{12}CO flux and the continuum flux is in Jy.
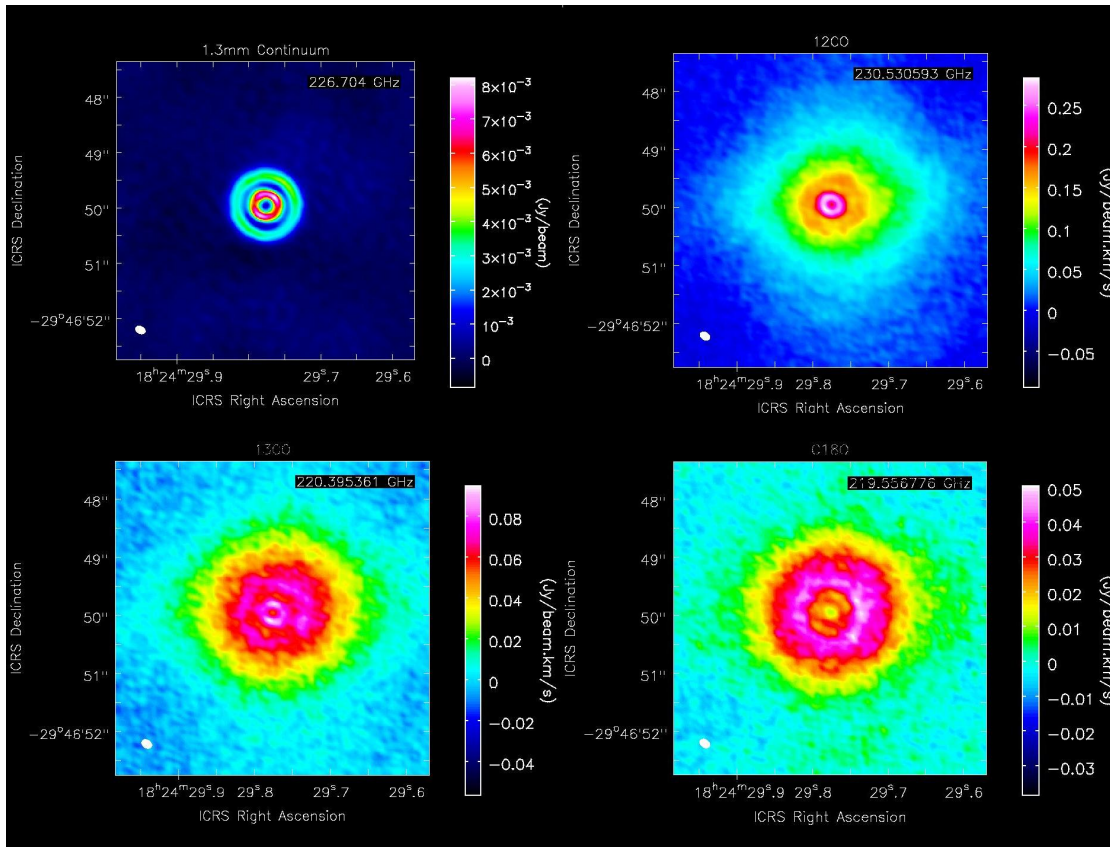
Figure 2.6: 1.3 mm continuum and moment 0 images of ^{12}CO, ^{13}CO and C^{18}O J=2-1 of the HD 169142. The beam size is displayed in white in the bottom left corner of each image.
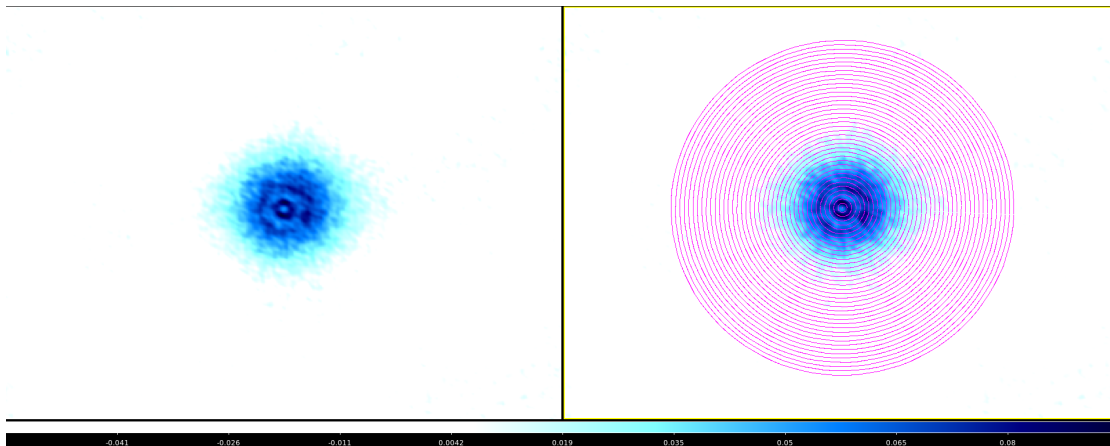
Figure 2.7: Left: ^{13}CO image of HD 169142; Right: the same but with elliptical apertures drawn on top.

31
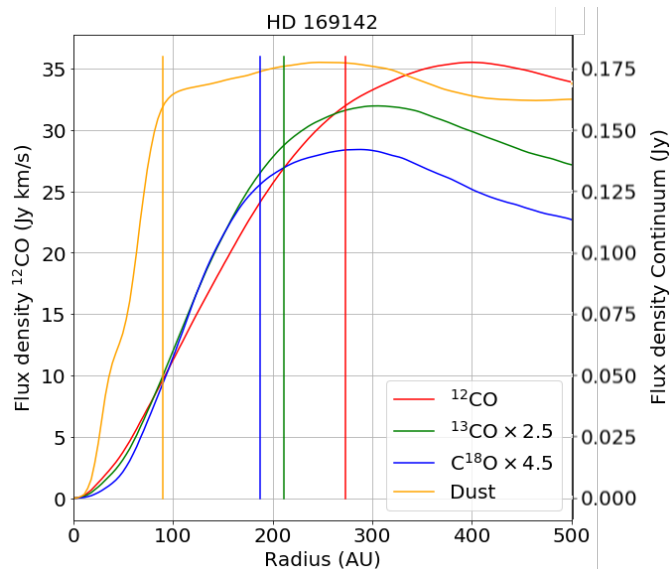
Figure 2.8: Cumulative flux profiles in HD 169142. The vertical lines correspond to R_{out} at which F_{90} is measured. The fluxes of Dust, ^{13}CO and $C^{18}O$ are scaled to ^{12}CO flux to fit in the same diagram.

2.5 The Disks's Outer Radii

To estimate the outer radii (R_{out}), as described by the curve-of-growth method, I find the maximum flux and then interpolate inwards to 90% of that value to find the corresponding radii. In Figure 2.8, vertical lines correspond to the radii at which the 90% value is reached. The same process is repeated for all sources. The continuum flux profiles reach a maximum value and stay constant afterwards since only noise will be added which has a mean value of 0. However, this is not the case for the line profiles which peak at a maximum radius but then start to decline since the noise is, on average, negative. All interferometric images have this problem of negative flux areas around the source but when creating the moment 0 maps by stacking all channels, this effect is amplified. As will be shown in Section 3, some sources were resolved while others were unresolved or marginally resolved. To classify these objects in a systematic way, sources with R_{out} smaller than the resolution are defined as unresolved, sources with R_{out} between 1 and 1.3 the resolution are defined as marginally resolved and sources with R_{out} greater than 1.3 the resolution are defined as resolved.

2.5.1 Error Analysis

To find the uncertainties in the outer radii, we first need to calculate the uncertainties in the flux measurements. Using the *imstat* task in CASA, we draw a region outside the disk and compute the *rms* of that region. The CASA task outputs the *rms* value in units of Jy/beam (continuum) or Jy/beam km/s (line). We use the *rms* together with the beam area (number of pixels/beam) to write a script which inputs the elliptical aperture corresponding to the 90% of the maximum flux and calculates the *rms* in that aperture, thus the uncertainty in the 90% flux measurement (F_σ). We use the error to find the lower radius R_{low} corresponding to $F_{90} - F_\sigma$ (see Figure 2.9) and the upper radius R_{up} corresponding to $F_{90} + F_\sigma$. The error in outer radius is defined as:

$(R_{up} - R_{low})/2$, in other words, the average separation with respect to R_{out}. The data quality for some sources is poor, resulting in a large uncertainty in the flux. For these cases, the R_{up}, corresponding to $F_{90} + F_{\sigma}$, cannot be calculated since $F_{90} + F_{\sigma}$ will be higher than the total flux. Therefore, we only use $(R_{out} - R_{low})$ as our uncertainty in the radius. Overall, the quality of ^{13}CO images is lower compared to the continuum images. This is due to the fact that most of the data in the archive is taken simultaneously for both gas and dust. Given an exposure time, the SNR is higher for the continuum than for the CO line. Usually, the prime focus of an observation is to have a dust detection and thus, not enough time is spent on achieving a high SNR for the CO lines as well. Detailed calculations and examples will be shown in Section 3.
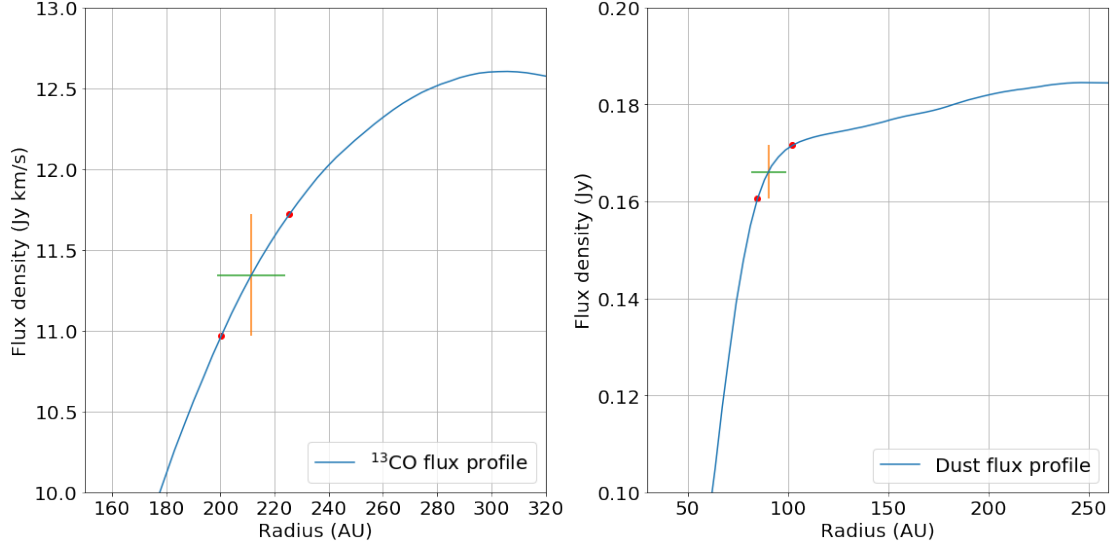
Figure 2.9: Error analysis in HD 169142. The yellow bar is the uncertainty in the line/continuum flux, the red dots are the corresponding R_{low} and R_{up} and the green bar is the uncertainty in the R_{out}. The spatial resolution of the observation is $0.19''$ (22 AU at 114 pc). Left: ^{13}CO; Right: Dust.

Chapter 3

Results

In this section I present the results for each source separately and discuss their uncertainties. For each source, a graph is shown consisting of the 1.3 mm continuum and the ^{13}CO images with their corresponding cumulative flux profiles, as well as an overview table of stellar parameters, observational data, and derived quantities from the analysis. The spatial resolution (in AU) is defined as the semi-major axis of the Gaussian beam multiplied by the distance, and the position angle (PA) and axis ratio (b/a) of the disk are found using CASA task $imfit$. Note that the values for the position angle are taken to be between $0°$ and $180°$ since we are only interested in the apparent position. For the sources that were not resolved, the Gaussian beam's PA and axis ratio were used. In general, the stellar parameters, such as luminosity, age, mass and temperature are taken from [Vioque et al., 2018], the distances are taken from [Gaia Collaboration, 2018] and the group classification from [Juhász et al., 2010]. Table 3.1 presents the overview of the 1.3mm continuum fluxes, ^{13}CO line fluxes as well as the corresponding dust and gas outer radii for all sources in my sample.

Name	R_{out} Dust AU	R_{out} ^{13}CO AU	Continuum Flux Jy	^{13}CO Flux Jy km/s
HD34282	351±53	866±194	0.100±0.005	5.24±0.75
HD169142	90.34±8.74	211±54	0.184±0.005	11.4±0.4
HD142527	283±10	463±77	1.16±0.03	10.7±0.7
HD100546	76.4±5.8	284±12	0.383±0.001	6.0±0.3
HD97048	314.3±2.8	572±80	0.716±0.003	13.8±1.2
HD36112	130.4±9.5	241±81	0.069±0.003	2.3±0.5
HD135344B	137.5±8.5	211±95	0.0170±0.0005	0.32±0.10
HD139614	105.2±0.7	176±20	0.2000±0.0005	2.7±0.2
HD163296	133±17.0	267±97	0.553±0.027	6.1±1.9
HD31648	117±9	385±45	0.265±0.006	5.90±0.37
AK Sco	66±4	101±25	0.026±0.001	0.610±0.036
HD145718	<126	149±18	0.049±0.0001	0.426±0.080
HD142666	<133	158±8	0.125±0.0001	0.640±0.051
HD104237	<173	<175	0.09±0.0001	0.150±0.01
KK Oph	<149	<128	0.029±0.0001	0.15±0.03

Table 3.1: Overview of outer radii and flux measurements. Upper, middle and bottom sections represent Group I, Group I/II and Group II disks, respectively.

3.1 HD 34282

As can be seen in the continuum image, the method slightly overestimates the outer radius of the disk, while in the ^{13}CO image, the outer parts of the disk gradually blend in with the noise resulting in a large uncertainty in the outer radius determination. The data set has a good SNR, however the products given in the archive are poorly reduced, especially the cleaning of the ^{13}CO data cube was not done perfectly created artefacts, such as artificial copies of the disk's emission around the main disk, that limit the effectiveness of the method.

Figure 3.1: Left: Dust and ^{13}CO images of HD 34282. The red ellipse corresponds to our outer radii measurement. Right: Cumulative flux profiles for dust and ^{13}CO gas. The yellow and green error bar correspond to the uncertainties in the flux and outer radii measurements, respectively. The red dots are the corresponding lower and upper limit on the outer radii measurement. The black line indicates the size of the semi-major axis of the beam.

Name	HD 34282		Log L (L$_\odot$)	$0.980^{+0.049}_{-0.039}$		Continuum Flux (Jy)	0.1 ± 0.0055
Project Code	2015.1.00192.S		Age (Gyr)	$6.5^{+2.4}_{-0.6}$		^{13}CO Flux (Jy km/s)	5.24 ± 0.755
RA (h:m:s)	05:16:00.5		Mass (M$_\odot$)	$1.450^{+0.072}_{-0.072}$		Spatial Resolution (AU)	77.8
Dec (deg:m:s)	-09:48:35		T$_{\rm eff}$ (K)	9500^{+250}_{-250}		Spectral Resolution ^{13}CO	244.17 kHz
Distance (pc)	$311.5^{+7.9}_{-7.2}$		R$_{\rm dust}$ (AU)	351 ± 53		Position Angle (°)	40
Group	I		R$_{^{13}\rm CO}$ (AU)	866.4 ± 194		Axial Ratio	0.56

Table 3.2: Overview of stellar parameters, observational data, and derived quantities from this thesis of HD 34282.

3.2 HD 169142

The data set of HD 169142 has a very high SNR with a very small beam size (22 AU) which results in a very clear and resolved dust disk. However, the high spatial resolution of the observation also generates a lot of noise at the outer edges of the ^{13}CO image since the emission per channel is much weaker there and when integrated over all channels (see Section 2.4.2) the noise is also added which results in a low SNR. As a test for the method used, I compare my calculation of the outer radii in the C^{18}O disk (187±40 AU, not shown here) with the results from a model fit from [Fedele et al., 2017] (180 AU) and I found that they agree well within 1σ.

Figure 3.2: Left: Dust and ^{13}CO images of HD 169142. The red ellipse corresponds to our outer radii measurement. Right: Cumulative flux profiles for dust and ^{13}CO gas. The yellow and green error bar correspond to the uncertainties in the flux and outer radii measurements, respectively. The red dots are the corresponding lower and upper limit on the outer radii measurement. The black line indicates the size of the semi-major axis of the beam.

Name	HD 169142	Log L (L$_\odot$)	$1.31^{+0.12}_{-0.22}$	Continuum Flux (Jy)	0.184±0.005
Project Code	2015.1.00490.S	Age (Gyr)	9^{+11}_{-4}	^{13}CO Flux (Jy km/s)	11.4±0.377
RA (h:m:s)	18:24:29.7	Mass (M$_\odot$)	$2.00^{+0.13}_{-0.13}$	Spatial Resolution (AU)	22
Dec (deg:m:s)	-29:46:49.9	T$_{\text{eff}}$ (K)	10700^{+800}_{-900}	Spectral Resolution ^{13}CO	122.08 kHz
Distance (pc)	$114^{+1.4}_{-1.3}$	R$_{\text{dust}}$ (AU)	90.34±8.74	Position Angle (°)	5
Group	I	R$_{^{13}\text{CO}}$ (AU)	211±54	Axial Ratio	0.97

Table 3.3: Overview of stellar parameters, observational data, and derived quantities from this thesis of HD 169142.

3.3   HD 142527

Both continuum and ^{13}CO images of the disk are well resolved with high SNR (>10) leading to accurate ($<17\%$ error for the $R_{^{13}CO}$ and $<4\%$ error for R_{dust}) calculations of the outer disk radii.

Figure 3.3: Left: Dust and ^{13}CO images of HD 142527. The red ellipse corresponds to our outer radii measurement. Right: Cumulative flux profiles for dust and ^{13}CO gas. The yellow and green error bar correspond to the uncertainties in the flux and outer radii measurements, respectively. The red dots are the corresponding lower and upper limit on the outer radii measurement. The black line indicates the size of the semi-major axis of the beam.

Name	HD 142527	Log L (L$_\odot$)	$0.963^{+0.026}_{-0.005}$	Continuum Flux (Jy)	1.161 ± 0.03
Project Code	2015.1.01353.S	Age (Gyr)	$6.6^{+0.3}_{-1.5}$	^{13}CO Flux (Jy km/s)	10.7 ± 0.67
RA (h:m:s)	15:56:41.8	Mass (M$_\odot$)	$1.61^{+0.12}_{-0.08}$	Spatial Resolution (AU)	42.4
Dec (deg:m:s)	-42:19:23.7	T$_{eff}$ (K)	6500^{+250}_{-250}	Spectral Resolution ^{13}CO	122.08 kHz
Distance (pc)	$157.3^{+2}_{-1.9}$	R$_{dust}$ (AU)	283 ± 9.53	Position Angle (°)	108
Group	I	R$_{^{13}CO}$ (AU)	463 ± 77.5	Axial Ratio	0.91

Table 3.4: Overview of stellar parameters, observational data, and derived quantities from this thesis of HD 142527.

3.4 HD 100546

For HD 100546, I used the continuum image from 2016.1.00344.S because the resolution ($\approx$27.5 AU) was small enough to resolve the dust disk ($\approx$80 AU), however the SNR was very low for the ^{13}CO line emission for this observation and the integrated moment 0 ^{13}CO image was very noisy. Therefore, I used another observation from 2015.1.01600.S which has a good SNR and resolved ^{13}CO line emission. The issue with the latter observation is the lower spatial resolution ($\approx$120 AU) which was not enough to resolve the dust disk, therefore it was only used for the ^{13}CO disk ($\approx$280 AU).

Figure 3.4: Left: Dust and ^{13}CO images of HD 100546. The red ellipse corresponds to our outer radii measurement. Right: Cumulative flux profiles for dust and ^{13}CO gas. The yellow and green error bar correspond to the uncertainties in the flux and outer radii measurements, respectively. The red dots are the corresponding lower and upper limit on the outer radii measurement. The black line indicates the size of the semi-major axis of the beam.

Name	HD 100546	Log L (L$_\odot$)	$1.371^{+0.069}_{-0.046}$	Continuum Flux (Jy)	0.383$\pm$0.0096
Project Code	2016.1.00344.S, 2015.1.01600.S	Age (Gyr)	$5.5^{+1.4}_{-0.8}$	^{13}CO Flux (Jy km/s)	6$\pm$0.263
RA (h:m:s)	11:33:25.3	Mass (M$_\odot$)	$2.05^{+0.10}_{-0.12}$	Spatial Resolution (AU)	27.5 &118
Dec (deg:m:s)	-70:11:41	T$_{\text{eff}}$ (K)	9750^{+500}_{-500}	Spectral Resolution ^{13}CO	244.17 kHz
Distance (pc)	110^{+1}_{-1}	R$_{\text{dust}}$ (AU)	76.4$\pm$5.84	Position Angle ($^\circ$)	55
Group	I	R$_{^{13}\text{CO}}$ (AU)	284$\pm$12.4	Axial Ratio	0.73

Table 3.5: Overview of stellar parameters, observational data, and derived quantities from this thesis of HD 100546.

3.5 HD 97048

The observations of HD 97048 are well resolved and have a high SNR. The line emission from the velocity channels centered around the LSR (local standard of rest) is suppressed which is due to absorption by foreground material as shown in [van der Plas et al., 2017]. They looked at ^{12}CO J=2-1 and J=3-2 and HCO^+ J=4-3 line emissions in HD 97048 and found an absorption feature between 3.4 and 5.7 km/s that completely blocks the line emission of ^{12}CO. This feature was not seen in the HCO^+ J=4-3 line, concluding that this line is not affected by the foreground absorption. It seems that the same feature is present in ^{13}CO J=2-1 line emission and can be seen as the missing emission from the west and east side of the ^{13}CO disk. It is not yet clear how the missing emission affects the outer radius measurement but given that the absorption is present in only few channels, the difference produced would be smaller than the large uncertainty in the outer radius measurement of 80 AU.

Figure 3.5: Left: Dust and ^{13}CO images of HD 97048. The red ellipse corresponds to our outer radii measurement. Right: Cumulative flux profiles for dust and ^{13}CO gas. The yellow and green error bar correspond to the uncertainties in the flux and outer radii measurements, respectively. The red dots are the corresponding lower and upper limit on the outer radii measurement. The black line indicates the size of the semi-major axis of the beam.

Name	HD 97048	Log L ($L_\odot$)	$1.174^{+0.093}_{-0.020}$	Continuum Flux (Jy)	0.716 ± 0.003
Project Code	2015.1.01600.S	Age (Gyr)	$4.4^{+1.1}_{-0.3}$	^{13}CO Flux (Jy km/s)	13.8 ± 1.22
RA (h:m:s)	11:08:03.2	Mass ($M_\odot$)	$2.25^{+0.11}_{-0.13}$	Spatial Resolution (AU)	161
Dec (deg:m:s)	-77:39:17	T_{eff} (K)	10500^{+500}_{-500}	Spectral Resolution ^{13}CO	122.07 kHz
Distance (pc)	$184.8^{+2.2}_{-2.1}$	R_{dust} (AU)	314.3 ± 2.82	Position Angle ($^\circ$)	98
Group	I	$R_{^{13}CO}$ (AU)	572 ± 80	Axial Ratio	0.73

Table 3.6: Overview of stellar parameters, observational data, and derived quantities from this thesis of HD 97048.

3.6   HD 36112

The observations of HD 36112 are well resolved. The continuum has a high SNR and a well defined outer edge. That is not the case for the ^{13}CO image which has low SNR resulting in a large uncertainty in the outer radius measurement.
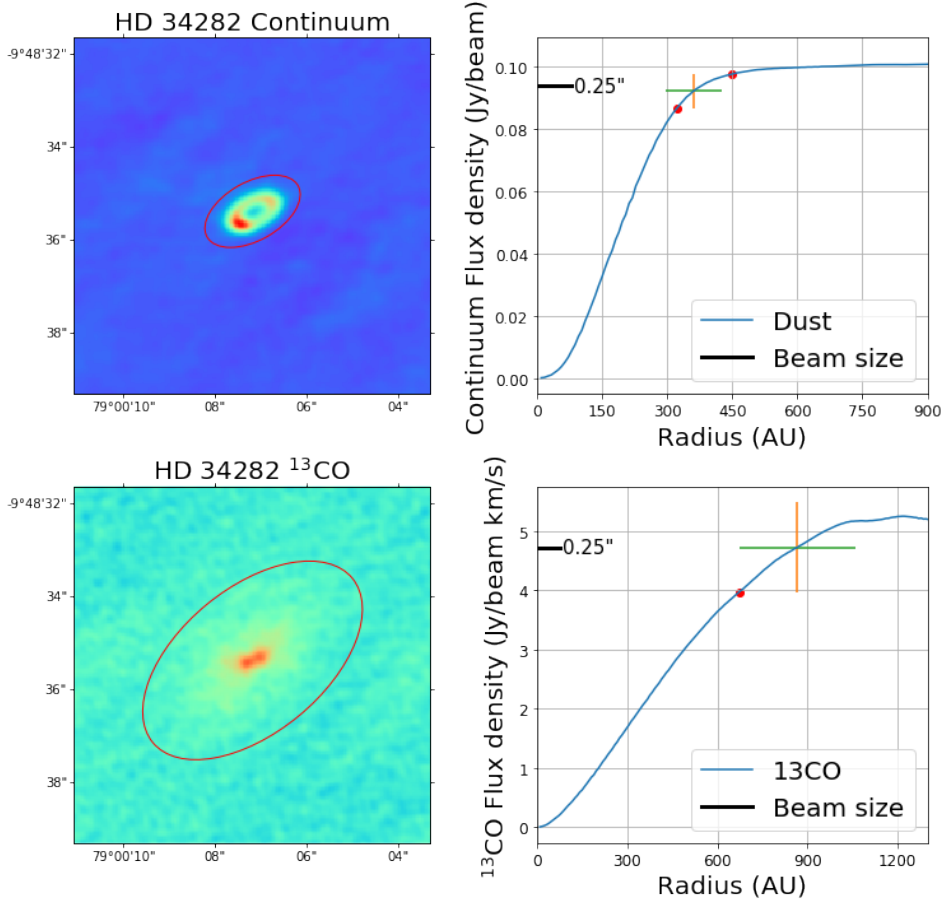

Figure 3.6: Left: Dust and ^{13}CO images of HD 36112. The red ellipse corresponds to our outer radii measurement. Right: Cumulative flux profiles for dust and ^{13}CO gas. The yellow and green error bar correspond to the uncertainties in the flux and outer radii measurements, respectively. The red dots are the corresponding lower and upper limit on the outer radii measurement. The black line indicates the size of the semi-major axis of the beam.

Name	HD 36112	Log L (L$_\odot$)	$1.04^{+0.12}_{-0.08}$	Continuum Flux (Jy)	0.069±0.0027
Project Code	2015.1.01600.S	Age (Gyr)	$8.3^{+0.4}_{-1.4}$	^{13}CO Flux (Jy km/s)	2.3±0.51
RA (h:m:s)	05:30:27.5	Mass (M$_\odot$)	$1.560^{+0.11}_{-0.08}$	Spatial Resolution (AU)	80
Dec (deg:m:s)	+25:19:57	T$_{\mathrm{eff}}$ (K)	7600^{+220}_{-300}	Spectral Resolution ^{13}CO	122.07 kHz
Distance (pc)	$160.3^{+2.9}_{-2.8}$	R$_{\mathrm{dust}}$ (AU)	130.4±9.54	Position Angle (°)	78
Group	I	R$_{^{13}\mathrm{CO}}$ (AU)	241±81	Axial Ratio	0.80

Table 3.7: Overview of stellar parameters, observational data, and derived quantities from this thesis of HD 36112.

3.7   HD 135344B

The dust disk of HD 135344B is marginally resolved (Figure 3.7, top left panel), therefore the outer radius measurement is an upper limit. The ^{13}CO emission is partially resolved but has a low SNR. As can be seen in Figure 3.7, the outer edge blends in with the noise resulting in a high uncertainty in the outer disk radius calculation.
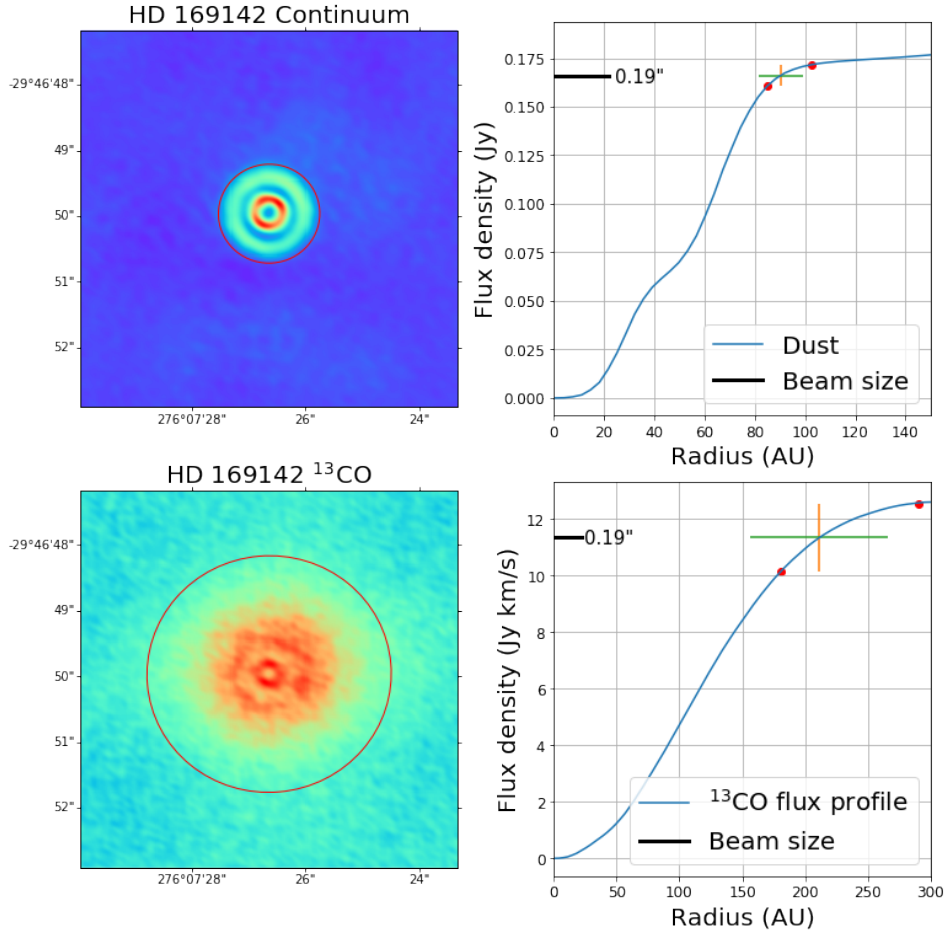

Figure 3.7: Left: Dust and ^{13}CO images of HD 135344B. The red ellipse corresponds to our outer radii measurement. Right: Cumulative flux profiles for dust and ^{13}CO gas. The yellow and green error bar correspond to the uncertainties in the flux and outer radii measurements, respectively. The red dots are the corresponding lower and upper limit on the outer radii measurement. The black line indicates the size of the semi-major axis of the beam.

Name	HD 135344B	Log L ($L_\odot$)	$0.786^{+0.033}_{-0.035}$	Continuum Flux (Jy)	0.017 ± 0.0005
Project Code	2015.1.01600.S	Age (Gyr)	$8.93^{+0.45}_{-0.91}$	^{13}CO Flux (Jy km/s)	0.32 ± 0.105
RA (h:m:s)	15:15:48.4	Mass ($M_\odot$)	$1.432^{+0.072}_{-0.072}$	Spatial Resolution (AU)	123.5
Dec (deg:m:s)	-37:09:16	$T_{\rm eff}$ (K)	6380^{+120}_{-120}	Spectral Resolution ^{13}CO	122.07 kHz
Distance (pc)	$135.8^{+2.4}_{-2.3}$	$R_{\rm dust}$ (AU)	137.5 ± 8.54	Position Angle ($^\circ$)	24.3
Group	I	$R_{^{13}CO}$ (AU)	211 ± 94.5	Axial Ratio	≈ 1

Table 3.8: Overview of stellar parameters, observational data, and derived quantities from this thesis of HD 135344B.

3.8 HD 139614

The dust disk of HD 139614 is not fully resolved as can be seen below, therefore the outer radius measurement is an upper limit. The ^{13}CO image is resolved and has a high SNR.
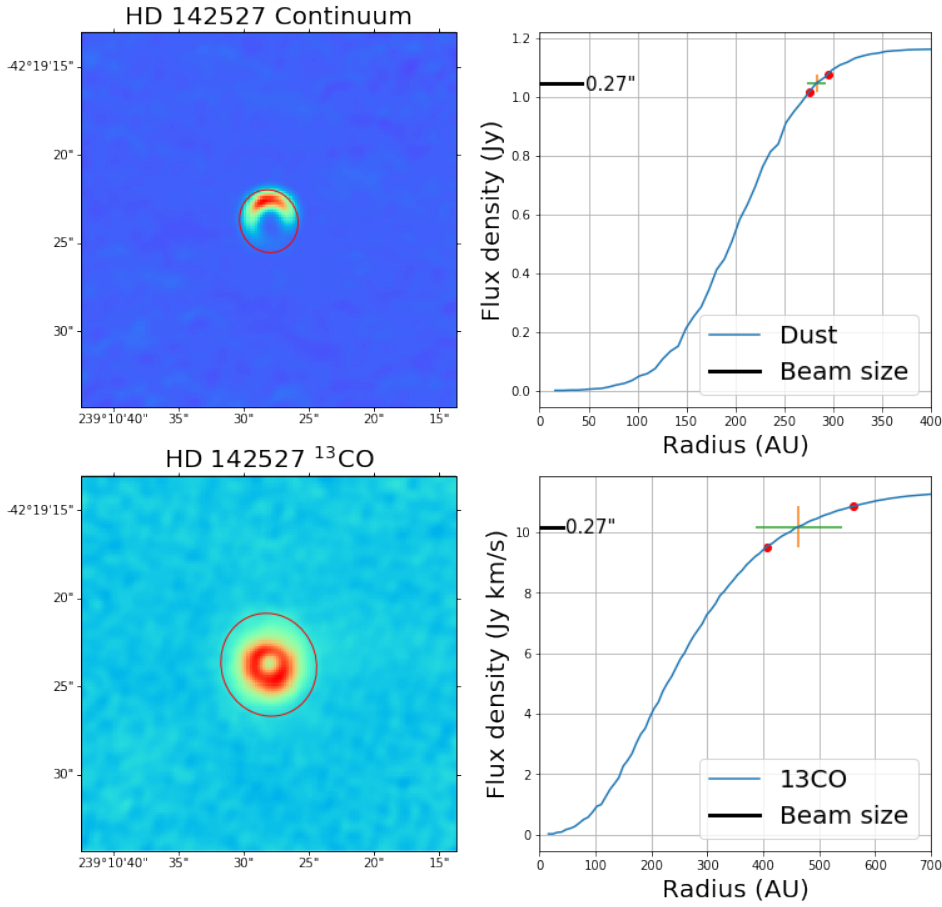

Figure 3.8: Left: Dust and ^{13}CO images of HD 139614. The red ellipse corresponds to our outer radii measurement. Right: Cumulative flux profiles for dust and ^{13}CO gas. The yellow and green error bar correspond to the uncertainties in the flux and outer radii measurements, respectively. The red dots are the corresponding lower and upper limit on the outer radii measurement. The black line indicates the size of the semi-major axis of the beam.

Name	HD 139614	Log L (L$_\odot$)	$0.773^{+0.032}_{-0.010}$	Continuum Flux (Jy)	0.2±0.0005
Project Code	2015.1.01600.S	Age (Gyr)	$14.5^{+1.4}_{-3.6}$	^{13}CO Flux (Jy km/s)	2.7±0.17
RA (h:m:s)	15:40:46.4	Mass (M$_\odot$)	$1.481^{+0.072}_{-0.072}$	Spatial Resolution (AU)	101
Dec (deg:m:s)	-42:29:54	T$_{\text{eff}}$ (K)	7750^{+250}_{-250}	Spectral Resolution ^{13}CO	122.07 kHz
Distance (pc)	$134.7^{+1.6}_{-1.6}$	R$_{\text{dust}}$ (AU)	105.2±0.7	Position Angle (°)	78
Group	I	R$_{^{13}\text{CO}}$ (AU)	176.6±20.6	Axial Ratio	0.92

Table 3.9: Overview of stellar parameters, observational data, and derived quantities from this thesis of HD 139614.

3.9 HD 163296

The continuum image of HD 163296 is well resolved and has a high SNR but the problems arise in the ^{13}CO image. The noisy features in the ^{13}CO image are the product of integrating over many velocity channels. The spectral resolution of this observation (30.52 kHz) is very high and therefore the line emission will be spread over a large number of channels. When integrating over all channels that contain emission, the noise is also added resulting in a poor image quality. To improve the SNR, one can use techniques such as Keplerian Masking. Based on the stellar paramaters (such as stellar mass, i, PA, LSR etc.), a mask is created for each channel around the line emission [Ansdell et al., 2018]. When the integrated moment 0 map is created (see Section 2.4.2), only the signal (both line emission and noise) inside the mask is considered, therefore reducing the total added noise. However, due to technical and time issues, this technique was not used in this work.
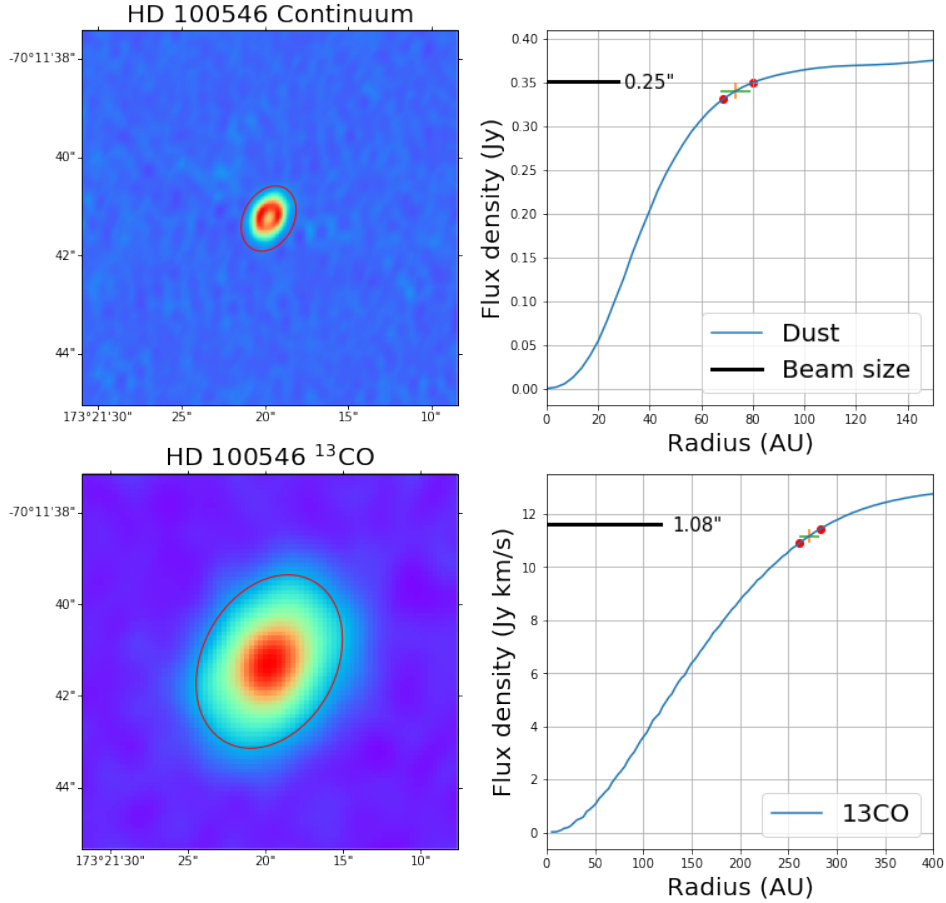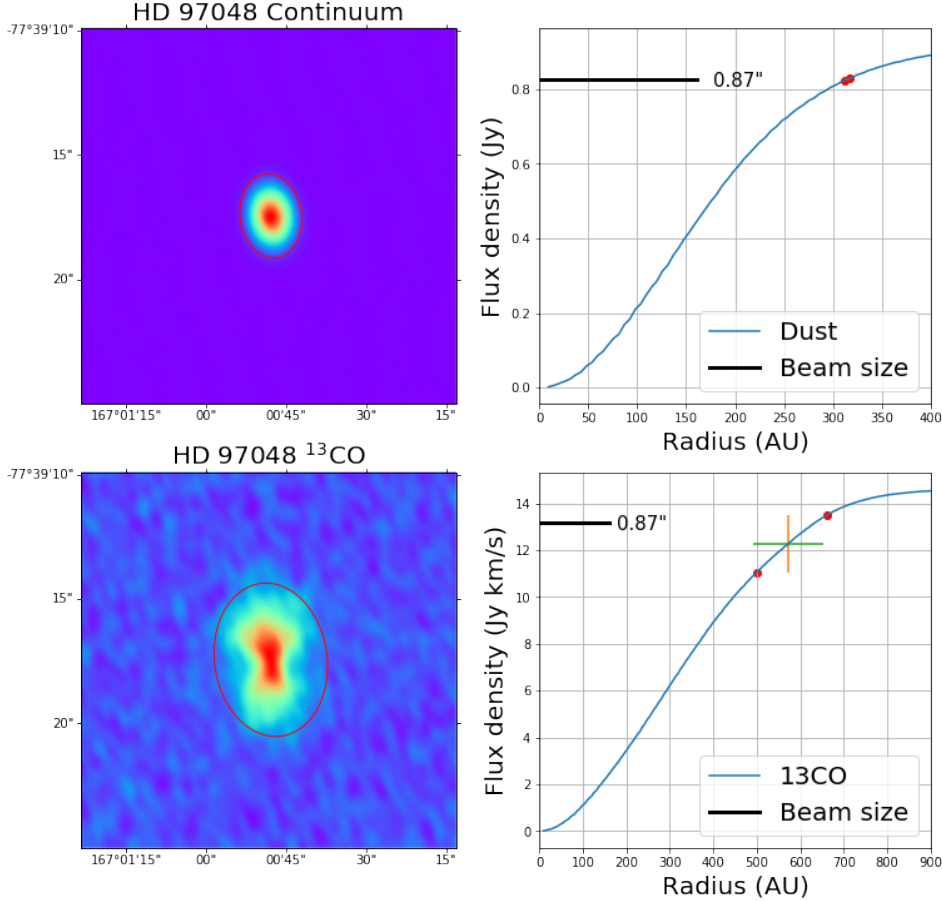

Figure 3.9: Left: Dust and ^{13}CO images of HD 163296. The red ellipse corresponds to our outer radii measurement. Right: Cumulative flux profiles for dust and ^{13}CO gas. The yellow and green error bar correspond to the uncertainties in the flux and outer radii measurements, respectively. The red dots are the corresponding lower and upper limit on the outer radii measurement. The black line indicates the size of the semi-major axis of the beam.

Name	HD 163296	Log L (L$_\odot$)	$1.199^{+0.055}_{-0.032}$	Continuum Flux (Jy)	0.553 ± 0.027
Project Code	2013.1.00601.S	Age (Gyr)	$7.6^{+1.1}_{-1.2}$	^{13}CO Flux (Jy km/s)	6.1 ± 1.94
RA (h:m:s)	17:56:21.3	Mass (M$_\odot$)	$1.833^{+0.092}_{-0.092}$	Spatial Resolution (AU)	27.4
Dec (deg:m:s)	-21:57:22	T$_{eff}$ (K)	9250^{+250}_{-250}	Spectral Resolution ^{13}CO	30.52 kHz
Distance (pc)	$101.5^{+2.0}_{-1.9}$	R$_{dust}$ (AU)	132.7 ± 17.0	Position Angle (°)	45
Group	I/II	R$_{^{13}CO}$ (AU)	267 ± 97	Axial Ratio	0.62

Table 3.10: Overview of stellar parameters, observational data, and derived quantities from this thesis of HD 163296.

3.10 HD 31648

The observation on HD 31648 has been performed with two different beam sizes. I used the smaller beam size continuum image to measure the dust outer disk radius since it was resolved, and the larger beam size to measure the ^{13}CO outer disk radius because of the high SNR. The ^{13}CO emission in the smaller beam size observation has a low SNR and therefore was not used while the dust disk was not resolved in the larger beam size observation.
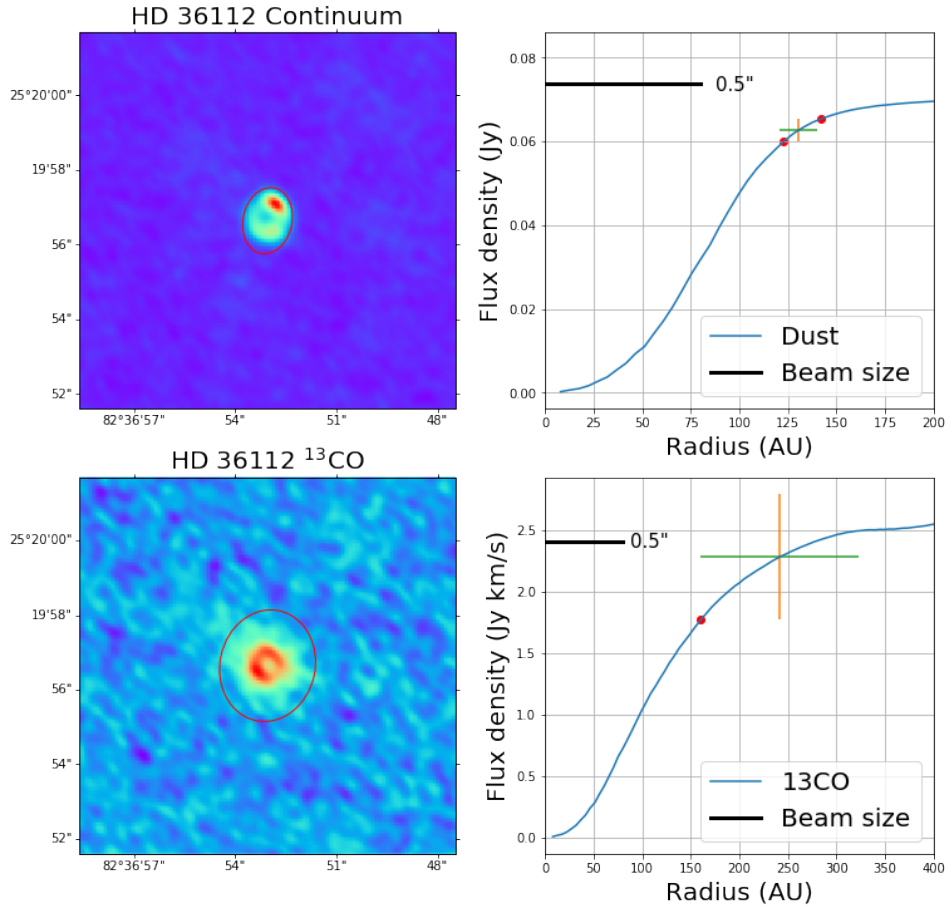

Figure 3.10: Left: Dust and ^{13}CO images of HD 31648. The red ellipse corresponds to our outer radii measurement. Right: Cumulative flux profiles for dust and ^{13}CO gas. The yellow and green error bar correspond to the uncertainties in the flux and outer radii measurements, respectively. The red dots are the corresponding lower and upper limit on the outer radii measurement. The black line indicates the size of the semi-major axis of the beam.

Name	HD 31648	Log L (L$_\odot$)	$1.27^{+0.14}_{-0.05}$	Continuum Flux (Jy)	0.265±0.006
Project Code	2016.1.00724.S	Age (Gyr)	$6.2^{+0.3}_{-1.1}$	^{13}CO Flux (Jy km/s)	5.9±0.375
RA (h:m:s)	04:58:46.3	Mass (M$_\odot$)	$1.78^{+0.13}_{-0.09}$	Spatial resolution (AU)	64.6 & 177.1
Dec (deg:m:s)	+29:50:37	T$_{\text{eff}}$ (K)	8250^{+200}_{-200}	Spectral resolution ^{13}CO	122.08 kHz
Distance (pc)	$161.8^{+3.4}_{-3.2}$	R$_{\text{dust}}$ (AU)	117±9	Position Angle (°)	83
Group	I/II	R$_{^{13}\text{CO}}$ (AU)	385±45	Axial Ratio	0.84

Table 3.11: Overview of stellar parameters, observational data, and derived quantities from this thesis of HD 31648.

3.11 AK Sco

For AK Sco, I used two observations. 2016.1.00204.S was used for the continuum since it has a small beam size that could resolve the dust disk. However, in that dataset, the ^{13}CO emission has a very low SNR, insufficient to perform a radius determination. Thus, the 2012.1.00496.S observation was used for the ^{13}CO outer radius determination. The dataset has a large beam size (177 AU), too large to resolve the ^{13}CO disk. Hence, I use the measured value as an upper limit.
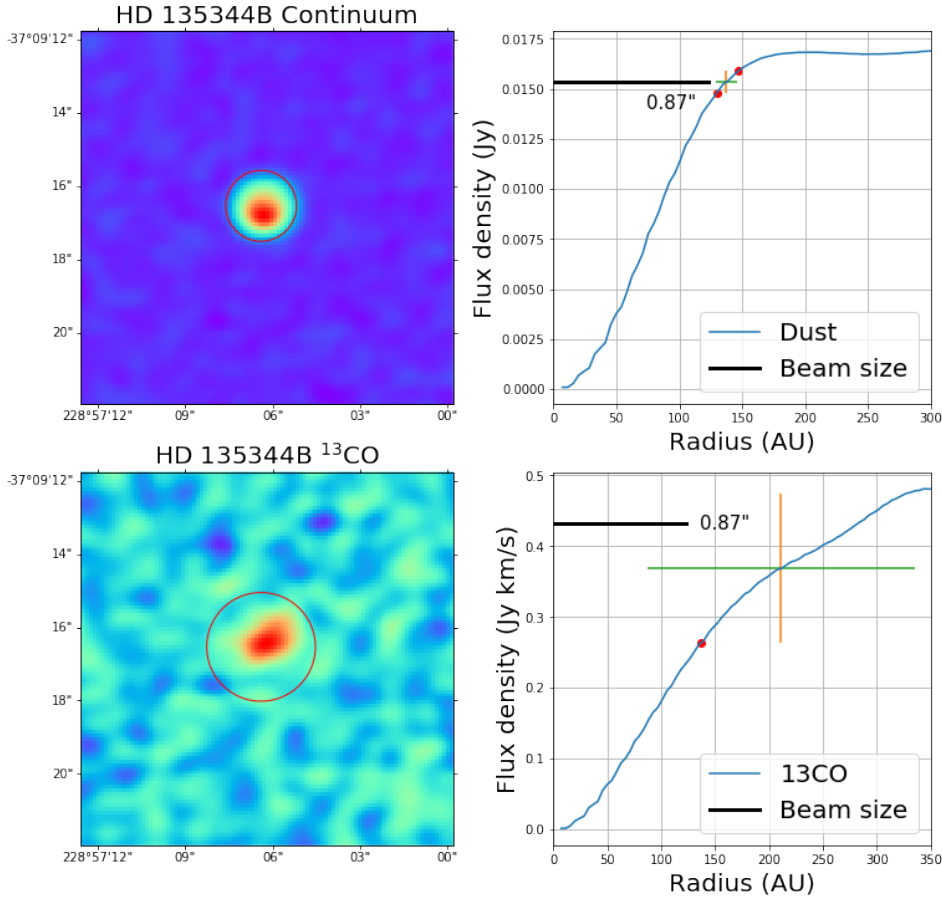

Figure 3.11: Left: Dust and ^{13}CO images of AK Sco. The red ellipse corresponds to our outer radii measurement. Right: Cumulative flux profiles for dust and ^{13}CO gas. The yellow and green error bar correspond to the uncertainties in the flux and outer radii measurements, respectively. The red dots are the corresponding lower and upper limit on the outer radii measurement. The black line indicates the size of the semi-major axis of the beam.

Name	AK Sco		Log L ($L_\odot$)	$0.623^{+0.028}_{-0.005}$	Continuum Flux (Jy)	0.026 ± 0.00095
Project Code	2016.1.00204.S & 2012.1.00496.S		Age (Gyr)	$8.4^{+1.7}_{-0.4}$	^{13}CO Flux (Jy km/s)	0.61 ± 0.0365
RA (h:m:s)	16:54:44.8		Mass ($M_\odot$)	$1.401^{+0.070}_{-0.070}$	Spatial Resolution (AU)	18.2 & 99.4
Dec (deg:m:s)	-36:53:19		T_{eff} (K)	6250^{+250}_{-250}	Spectral Resolution ^{13}CO	122.06 kHz
Distance (pc)	$140.6^{+2.1}_{-2.0}$		R_{dust} (AU)	66.17 ± 4	Position Angle (°)	143
Group	II		$R_{^{13}CO}$ (AU)	101.2 ± 25	Axial Ratio	0.60

Table 3.12: Overview of stellar parameters, observational data, and derived quantities from this thesis of AK Sco.

3.12 HD 145718

The observation on HD 145718 has a good SNR (>5 for ^{13}CO), however the dust disk is not resolved and the calculated outer dust radius will be used as an upper limit. The ^{13}CO image is marginally resolved.
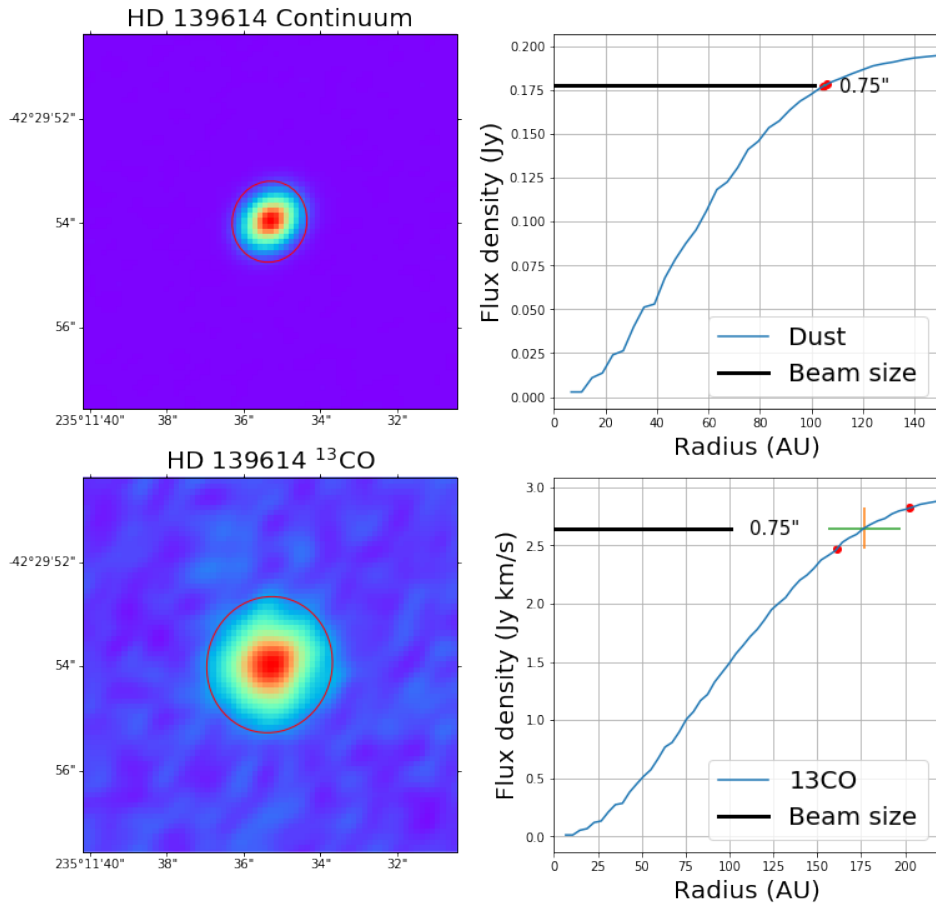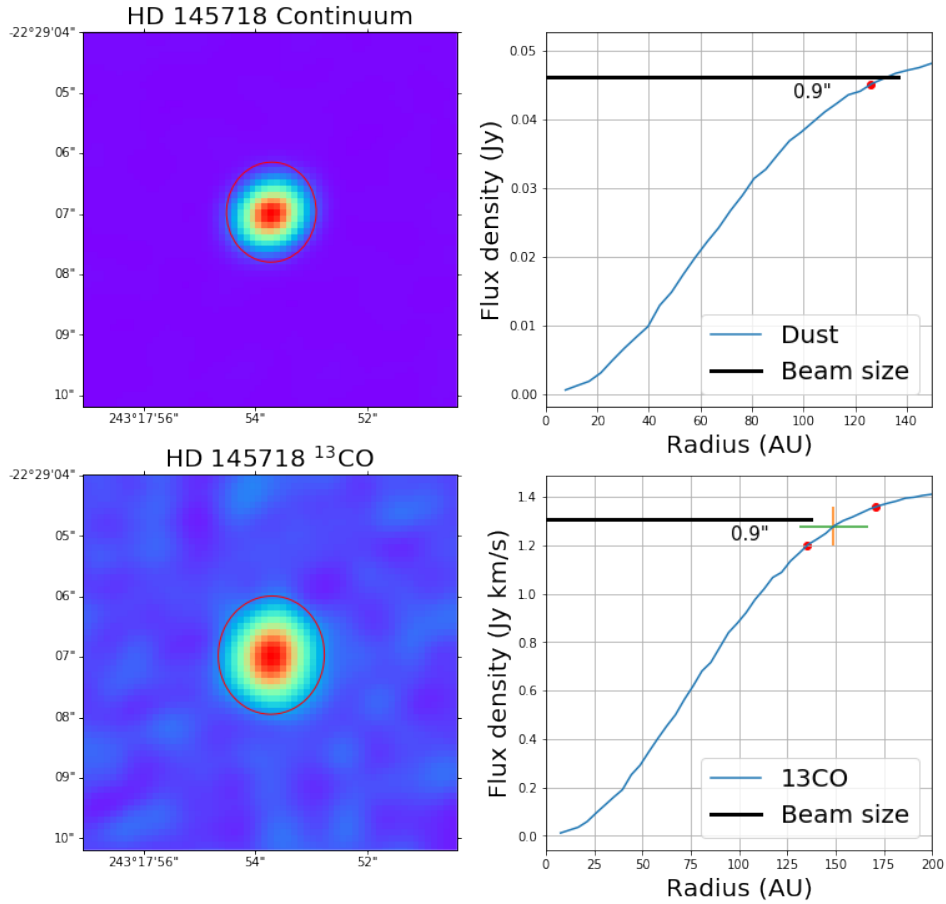

Figure 3.12: Left: Dust and ^{13}CO images of HD 145718. The red ellipse corresponds to our outer radii measurement. Right: Cumulative flux profiles for dust and ^{13}CO gas. The yellow and green error bar correspond to the uncertainties in the flux and outer radii measurements, respectively. The red dots are the corresponding lower and upper limit on the outer radii measurement. The black line indicates the size of the semi-major axis of the beam.

Name	HD 145718	Log L (L$_\odot$)	$0.899^{+0.046}_{-0.039}$	Continuum Flux (Jy)	0.049 ± 0.0001
Project Code	2015.1.01600.S	Age (Gyr)	$9.8^{+2.8}_{-0.5}$	^{13}CO Flux (Jy km/s)	0.426 ± 0.080
RA (h:m:s)	16:13:11.6	Mass (M$_\odot$)	$1.605^{+0.08}_{-0.08}$	Spatial Resolution (AU)	136.8
Dec (deg:m:s)	-22:29:07	T$_{eff}$ (K)	8000^{+250}_{-250}	Spectral Resolution ^{13}CO	122.07 kHz
Distance (pc)	$152.5^{+3.2}_{-3.0}$	R$_{dust}$ (AU)	126	Position Angle ($^\circ$)	87.1
Group	II	R$_{13CO}$ (AU)	149 ± 17.8	Axial Ratio	0.85

Table 3.13: Overview of stellar parameters, observational data, and derived quantities from this thesis of HD 145718.

3.13   HD 142666

The observation of HD 142666 has a good SNR ($>$10 for ^{13}CO), however the dust disk is not resolved and the calculated value will be used as an upper limit. The ^{13}CO image is resolved.
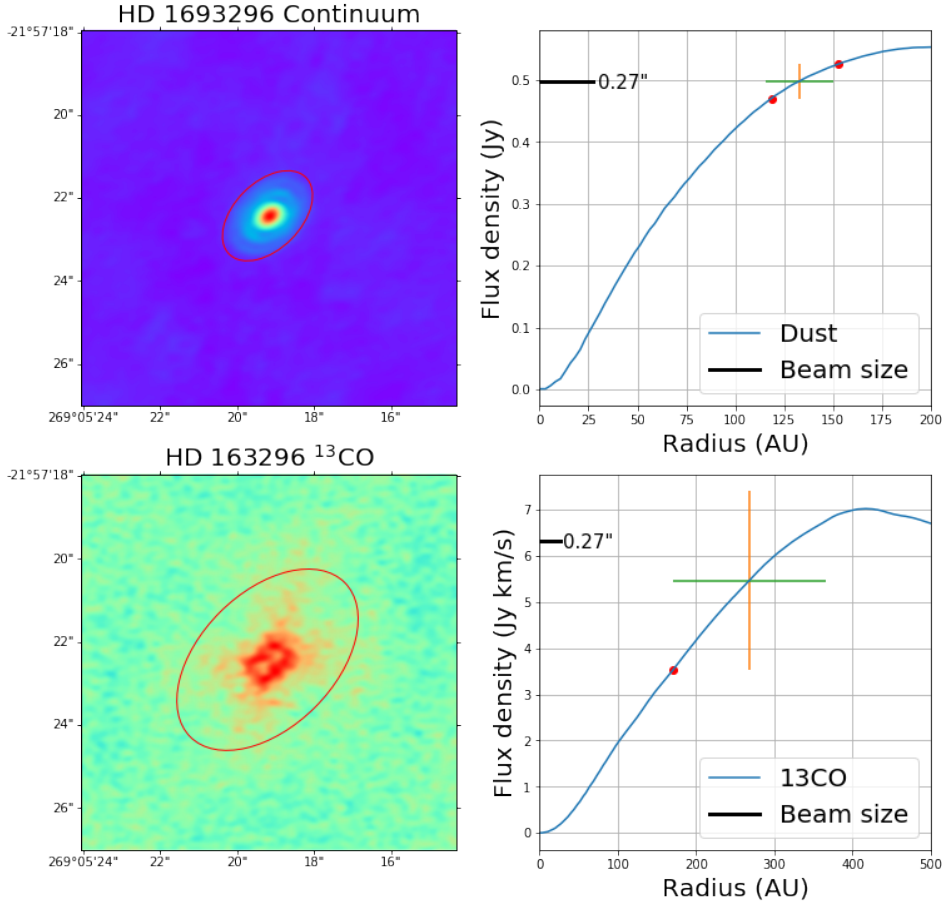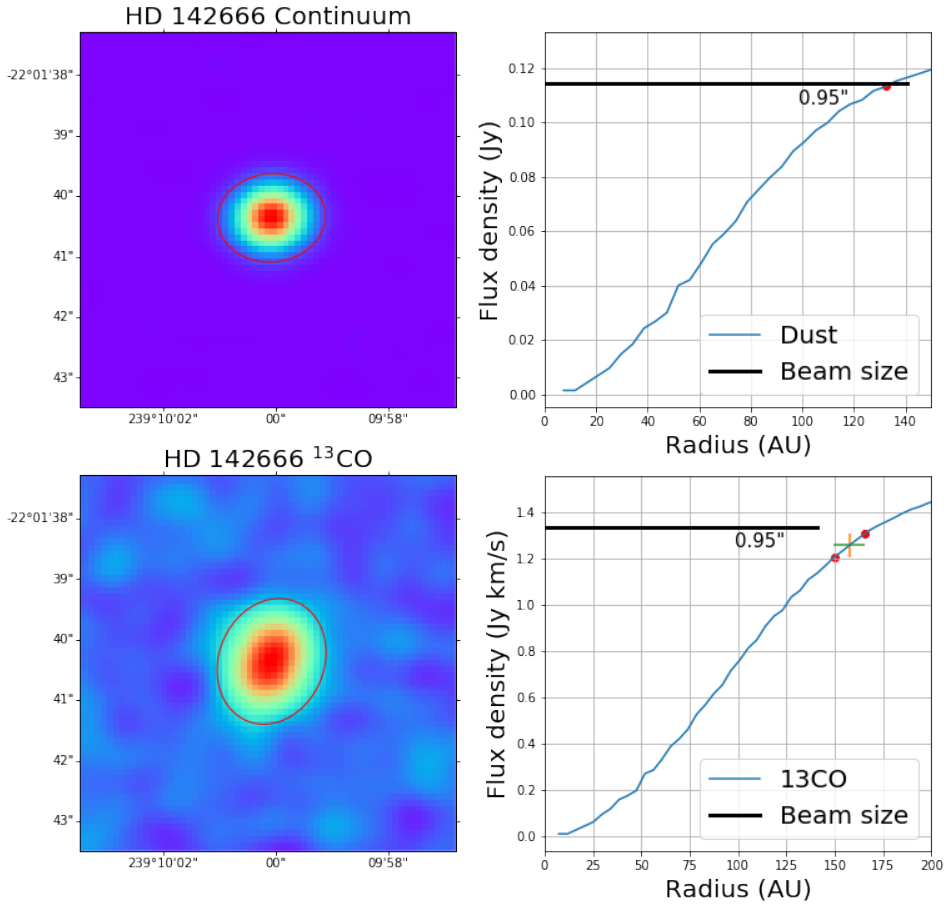

Figure 3.13: Left: Dust and ^{13}CO images of HD 142666. The red ellipse corresponds to our outer radii measurement. Right: Cumulative flux profiles for dust and ^{13}CO gas. The yellow and green error bar correspond to the uncertainties in the flux and outer radii measurements, respectively. The red dots are the corresponding lower and upper limit on the outer radii measurement. The black line indicates the size of the semi-major axis of the beam.

Name	HD 142666	Log L ($L_\odot$)	$0.939^{+0.043}_{-0.045}$	Continuum Flux (Jy)	0.125$\pm$0.0001
Project Code	2015.1.01600.S	Age (Gyr)	$9.33^{+0.77}_{-0.47}$	^{13}CO Flux (Jy km/s)	0.640$\pm$0.051
RA (h:m:s)	15:56:40.0	Mass ($M_\odot$)	$1.493^{+0.075}_{-0.075}$	Spatial Resolution (AU)	140.8
Dec (deg:m:s)	-22:01:40	T_{eff} (K)	7500^{+250}_{-250}	Spectral Resolution ^{13}CO	122.07 kHz
Distance (pc)	$148.3^{+2}_{-1.9}$	R_{dust} (AU)	133	Position Angle ($^\circ$)	67.5
Group	II	$R_{^{13}CO}$ (AU)	158$\pm$8	Axial Ratio	0.82

Table 3.14: Overview of stellar parameters, observational data, and derived quantities from this thesis of HD 142666.

3.14 HD 104237

The observation of HD 104237 has a good SNR (>10), however both dust and ^{13}CO disks are not resolved and therefore the outer disk radii for continuum and ^{13}CO will be used as upper limits.
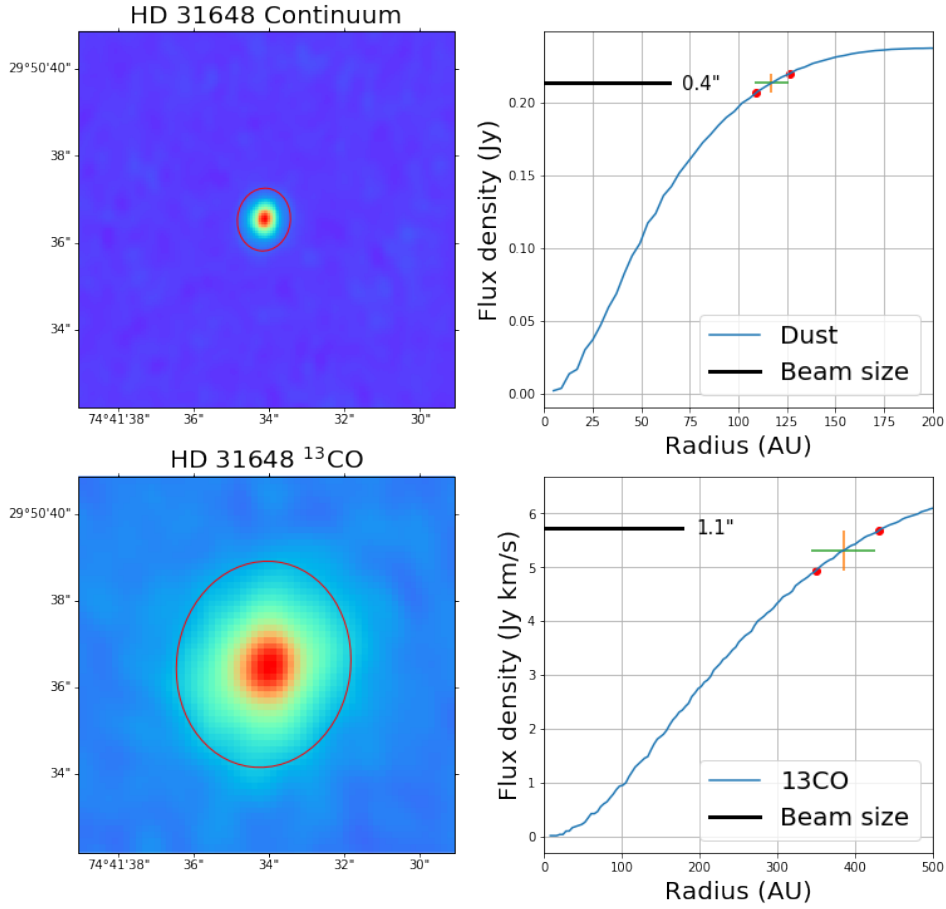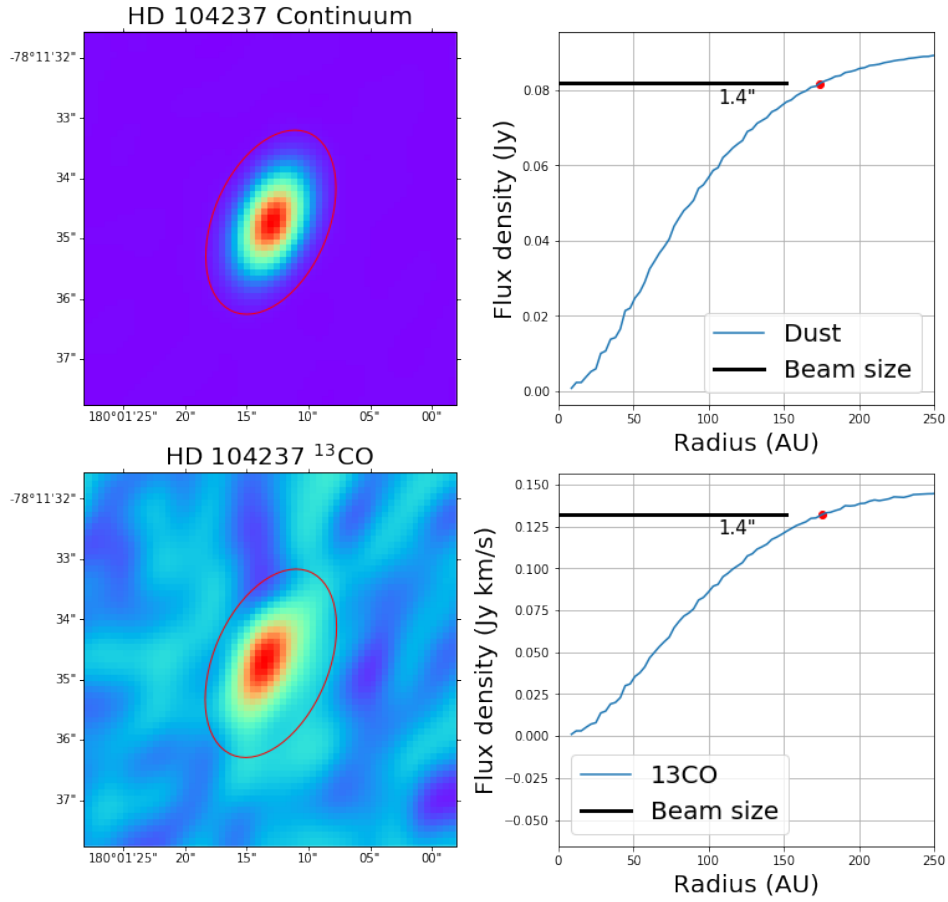

Figure 3.14: Left: Dust and ^{13}CO images of HD 104237. The red ellipse corresponds to our outer radii measurement. Right: Cumulative flux profiles for dust and ^{13}CO gas. The red dot is our outer radii measurement. The black line indicates the size of the semi-major axis of the beam.

Name	HD 104237	Log L (L$_\odot$)	$1.329^{+0.035}_{-0.011}$	Continuum Flux (Jy)	0.09±0.0001
Project Code	2015.1.01600.S	Age (Gyr)	$5.48^{+0.27}_{-0.4}$	^{13}CO Flux (Jy km/s)	0.15±0.01
RA (h:m:s)	12:00:04.9	Mass (M$_\odot$)	$1.849^{+0.092}_{-0.092}$	Spatial Resolution (AU)	151.8
Dec (deg:m:s)	-78:11:35	T$_{eff}$ (K)	8000^{+250}_{-250}	Spectral Resolution ^{13}CO	122.07 kHz
Distance (pc)	$108.4^{+1.1}_{-1.1}$	R$_{dust}$ (AU)	173	Position Angle (°)	67
Group	II	R$_{^{13}CO}$ (AU)	175	Axial Ratio	0.59

Table 3.15: Overview of stellar parameters, observational data, and derived quantities from this thesis of HD 104237.

3.15   KK Oph

The dust disk of KK Oph is not resolved and the value derived for the outer radius will be used as an upper limit. The ^{13}CO emission is marginally detected ($< 3\sigma$). This is somewhat expected since KK Oph is a very old object and might have most of its CO depleted. However, to test this hypothesis, we would need ^{12}CO data which not available at the moment. Nonetheless, I still measure the outer ^{13}CO disk radius and use it as an upper limit.
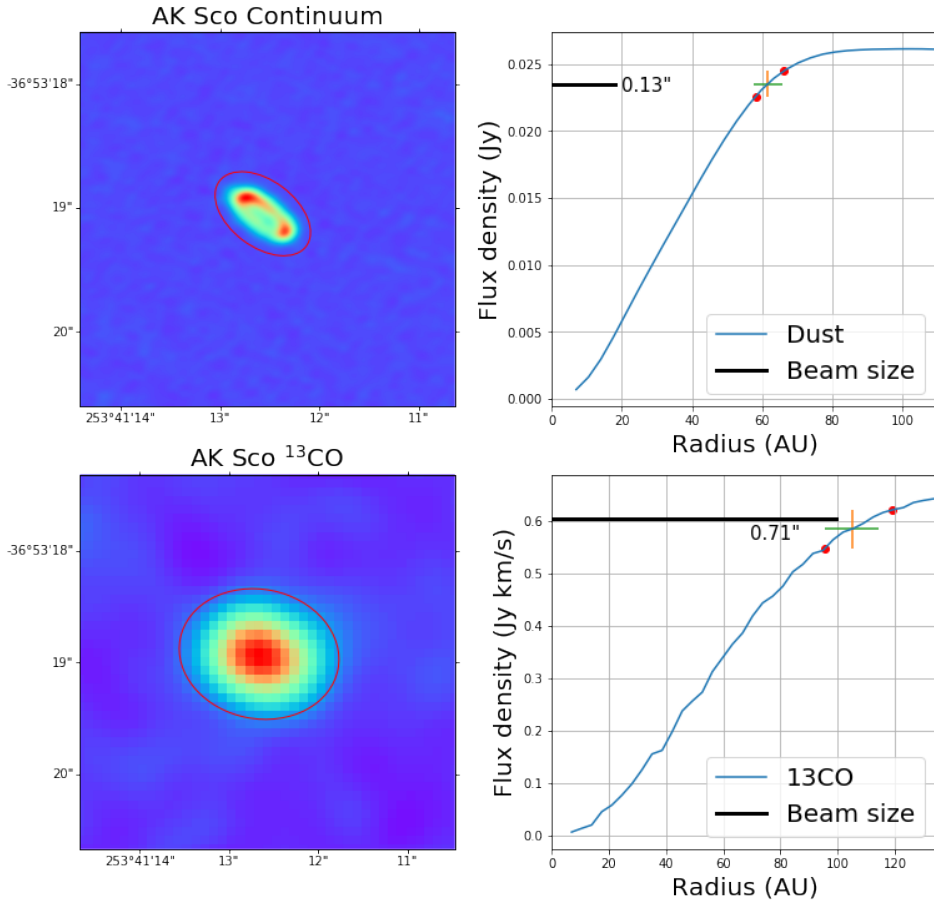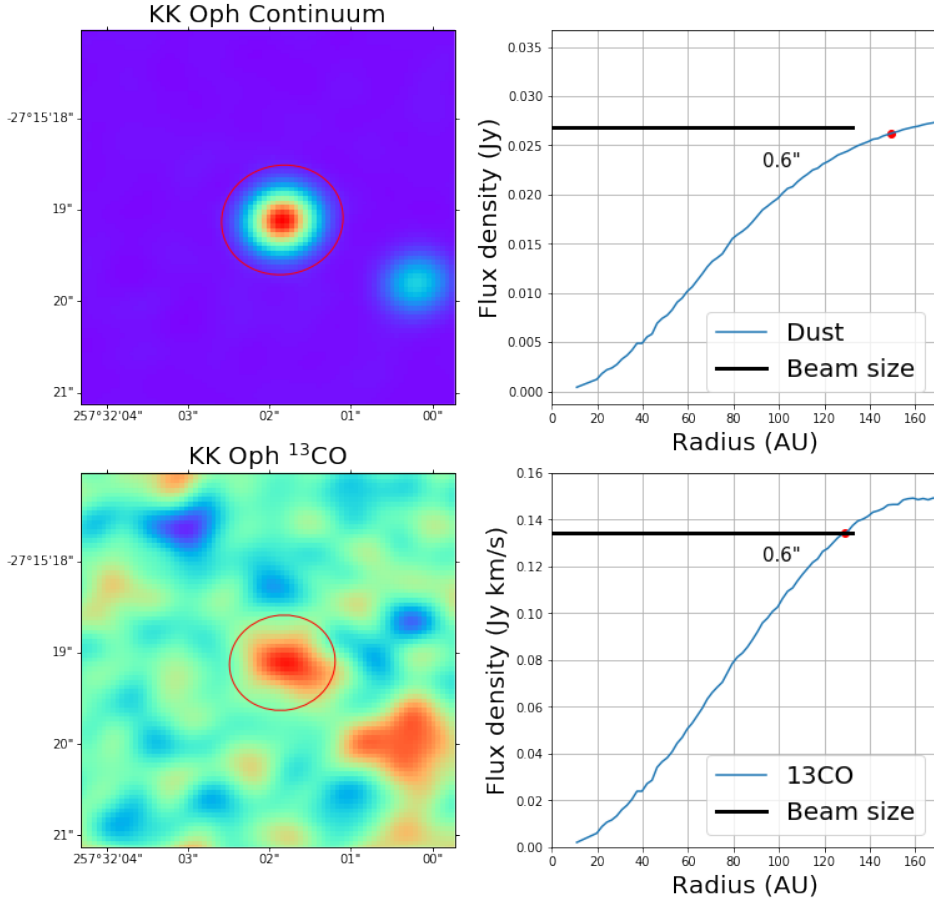

Figure 3.15: Left: Dust and ^{13}CO images of KK Oph. The red ellipse corresponds to our outer radii measurement. Right: Cumulative flux profiles for dust and ^{13}CO gas. The red dot is our outer radii measurement. The black line indicates the size of the semi-major axis of the beam.

Name	KK Oph	Log L ($L_\odot$)	$0.71^{+0.11}_{-0.11}$	Continuum Flux (Jy)	0.029 ± 0.0001
Project Code	2015.1.01600.S	Age (Gyr)	$18.5^{+1.5}_{-1.4}$	^{13}CO Flux (Jy km/s)	0.15 ± 0.03
RA (h:m:s)	17:10:08.1	Mass ($M_\odot$)	$1.513^{+0.076}_{-0.076}$	Spatial Resolution (AU)	132.6
Dec (deg:m:s)	-27:15:19	T_{eff} (K)	8500^{+500}_{-500}	Spectral Resolution ^{13}CO	122.07 kHz
Distance (pc)	221^{+12}_{-10}	R_{dust} (AU)	149	Position Angle (°)	154
Group	II	$R_{^{13}CO}$ (AU)	128	Axial Ratio	0.67

Table 3.16: Overview of stellar parameters, observational data, and derived quantities from this thesis of KK Oph.

Chapter 4

Discussion

The main goal of this thesis is to measure the outer gas and dust radii of protoplanetary disks around Herbig Ae/Be stars and compare between Group I and Group II disks. This research is a first step in understanding the evolutionary link between the different classes of protoplanetary disks and the various planetary systems discovered by the recent exoplanet missions. These planetary systems can vary from being very compact (see TRAPPIST-1, 7 $M_\oplus$ planets between 0.01-0.07 AU [Gillon et al., 2017]) to $M_{\rm jup}$ planets at large separations (>100 AU) [Nielsen et al., 2019]. In the Results section, I presented images and measurements of outer radii for each disk. It can be seen that Group I data surpasses the quality of Group II data (see Table 3.1). Out of 5 Group II disks, only one (AK Sco) has the dust emission spatially resolved and two (HD 145718 & HD 142666) have the ^{13}CO emission spatially resolved. Nonetheless, these results can still be used to uncover possible trends or differences between the two groups.

Initially, it was thought that Group I disks evolve into Group II in the framework of dust settling with time [Dullemond and Dominik, 2004]. However, [Maaskant et al., 2013] theorized that all Group I disks have large gaps which disconsiders this potential evolutionary pathway. Therefore, the question becomes: would it be possible for Group II disks to carve an inner gap (ex. through binary interaction) and evolve into Group I disks or there is no link between the two groups and they simply follow different evolutionary tracks. The points will be addressed in the following subsections.

4.1   Outer disk radii: Gas versus Dust

As discussed in Section 1.3.2, it was previously observed that CO sub-mm emission extended further than the continuum emission from dust [Dutrey et al., 1998, Guilloteau and Dutrey, 1998, Piétu et al., 2005, Piétu et al., 2007, Isella et al., 2007, Panić and Hogerheijde, 2009, de Gregorio-Monsalvo et al., 2013, Rosenfeld et al., 2013]. In Figure 4.1, I plot the outer gas disk radii ($R_{\rm out}$ ^{13}CO) versus the outer dust disk radii ($R_{\rm out}$ Dust). It can be seen that Group II disks are small (<150 AU gas & dust) while Group I disks span a larger range in disk sizes. Furthermore, for the spatially and marginally resolved sources, the $R_{\rm out}$ ^{13}CO ranges between ≈1.5-3 $R_{\rm out}$ Dust with an average of 2.17±0.21 (where the error is the standard deviation of the mean). We compare our results for Herbig Ae/Be disks with T Tauri disks from the ALMA Lupus survey [Ansdell et al., 2018]. The sample size of T Tauri disks is twice as large and [Ansdell et al., 2018] use ^{12}CO instead of ^{13}CO. Since ^{13}CO becomes optically thin at smaller radial distances than ^{12}CO, we expect the ratio of gas-to-dust outer radius to be higher for ^{12}CO. Also, the Lupus survey is homogeneous in age (1∼3 Myr [Comerón, 2008]), contrary to

our Herbig Ae/Be sample, since all of these objects are found in the same star-forming region. Using the same cumulative flux method, [Ansdell et al., 2018] find the ratio between the ^{12}CO gas and dust outer disk radii to be 1.96±0.04. If this ratio would be similar for the T Tauri and Herbig Ae/Be stars, then we would expect the ratio using the ^{12}CO gas to be larger than ^{13}CO ratio. Since this is not the case, it might be possible that on average, Herbig Ae/Be disks have the CO emission extended further compared to T Tauri stars. Nonetheless, our sample size is very limited and [Ansdell et al., 2018] observe only one star-forming region, resulting in a biased sample. Thus, it is not possible to draw strong conclusions given the current observations.
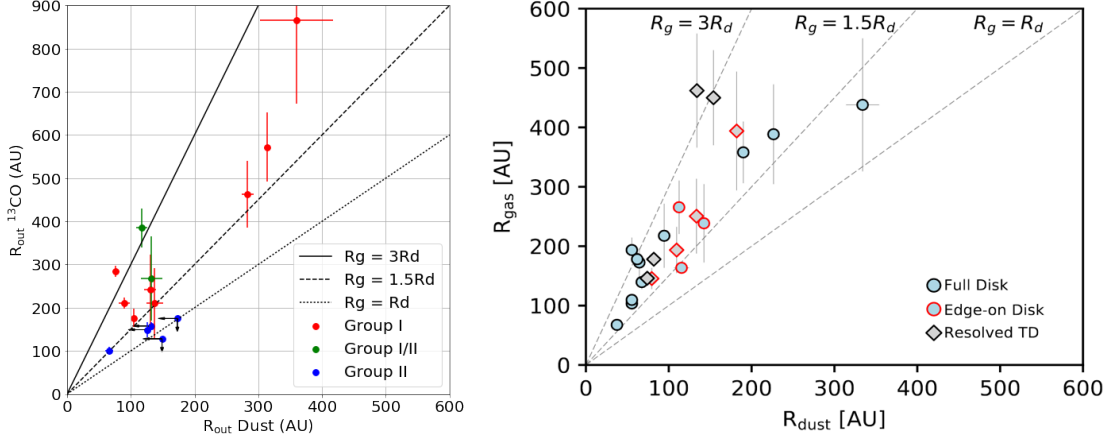
Figure 4.1: Gas versus Dust Outer Disk Radii; Left: This work. Black arrows mark upper limits; Right: Results of T Tauri disks from Lupus [Ansdell et al., 2018]; Black lines are drawn at R_{gas} = 3,1.5,1 R_{dust}.

4.2 Outer disk radii evolving in time?

In an attempt to identify a possible evolution from a Group I to a Group II disk or vice versa, we study the outer radii against the age. Most of the Herbig stars in our sample are younger than 10 Myr [Vioque et al., 2018]. A slight decreasing trend with age can be observed for dust which is consistent with the radial drift of dust (see Section 1.4). The same decreasing trend is seen for the gas disk. Since the gas disk viscously disperses in time (see Figure 1.8), one would expect the outer radius to increase. However, the observations have limited sensitivity and as the gas disk disperses, it will become fainter. Since the centre is brighter than the outer parts, in time it would appear as the disk is shrinking in size.

There are studies that describe the gas spreading through viscous evolution [Dominik, 2015b] but they do not take into account the limited sensitivity of observations. To understand how the observed outer gas disk radii will evolve with time, one has to follow in the model the evolution of a fixed column density, corresponding to the sensitivity limit of an observation. There are no such studies yet, therefore I choose to fit[1] two simple laws: a power law $R = a \times t^b$ where R is the radius and t is the age (see Figure 4.2) and an exponential law $R = a \times e^{-t/b}$ (see Figure 4.3) and I find that:

$$R_{\text{out}} \, ^{13}\text{CO} \, (\text{AU}) = 2885 \times \text{t(Myr)}^{-1.13\pm0.5} \tag{4.1}$$

---

[1]Due to a very small sample size, upper limits were taken into account in the fits as well.

$$R_{\text{out}} \text{Dust (AU)} = 806 \times \text{t(Myr)}^{-0.8 \pm 0.4} \tag{4.2}$$

$$R_{\text{out}} \, ^{13}\text{CO (AU)} = 1045 \times \text{e}^{-\text{t(Myr)}/6(\pm 3)} \tag{4.3}$$

$$R_{\text{out}} \text{Dust (AU)} = 326 \times \text{e}^{-\text{t(Myr)}/11.2(\pm 7.4)} \tag{4.4}$$

From the limited sample size, is not yet clear which law fits the data better. Overall, the decreasing trend is much tighter in the gas than in the dust. This effect is seen in the exponential law fit where the b term can be interpreted as half lifetime for disk "shrinking". The b value of 6 Myr found for the ^{13}CO is half the value of 11.2 Myr found for the dust and can be interpreted as gas disks evolving twice as fast as the dust disks, to a first order approximation. When comparing between the two Groups, it can be seen that, in ^{13}CO, Group I disks show a strong evolution with time while Group II disks do not and could even remain constant. Group II disk's evolution is not yet clear due to limited sample size and unresolved disks. In the dust, by visually inspecting the data, two distinct regions can be seen. The upper one which includes the three Group I disks with $R_{\text{out Dust}}$>270 AU and the lower region with $R_{\text{out Dust}}$<180 AU where most of the disks are located. However, it is not clear if these two regions are physically distinct or whether is an observational bias since our sample is drawn from the archival data, which is heavily biased towards nearby bright objects. In the sample of [Garufi et al., 2017], Group II disks have ages between 2 Myr and 6 Myr, whereas Group I disks have ages between 1 Myr and 15 Myr, where half of them are older than 10 Myr. This is not the case in our sample where only two disks, one Group I and one Group II are older than 10 Myr. Therefore, for a better analysis of the evolution of disks, the entire age span needs to be uniformly sampled. Yet, the biggest issue comes for the age determination of the protostars which is achieved by fitting isochrones, a curve on the Hertzsprung-Russell diagram which represents a population of stars of the same age. There are many factors that are problematic with this method, making it not yet credible. Good estimates of the effective temperature T_{eff} and bolometric luminosity L_{bol} are required to place the stars in the HR diagram. Remarkable improvements have been made in the recent years with the launch of Gaia [Gaia Collaboration, 2018] at measuring these parameters, and more developments are expected to come in the upcoming years. However, both parameters are affected by extinction, non-uniform reddening, circumstellar material and accretion [Soderblom et al., 2014]. Also, other effects such as unresolved binaries can add uncertainties in the luminosity.

4.3 Continuum and line luminosities versus outer disk radii

After measuring the flux density and using the distance measurements from GAIA, we computed the continuum and line luminosities. To understand the observed strength of emission, both in line and continuum in the framework of simple models, the luminosity is defined as the product of the intensity per unit area I_ν and the area of the disk ($\propto R^2$). For optically thick emission $I_\nu \sim B_\nu$ and $B_\nu \propto T$ in the Rayleigh–Jeans approximation for long wavelengths. We adopt a simplified temperature profile where T_{c} is the temperature at a unit radius r_{c} (usually r_{c} is taken to be 1 AU in literature, however the unit is not relevant in this work):

$$T(\text{R}) = T_{\text{c}} \times (r/r_{\text{c}})^{-\text{q}} \tag{4.5}$$

Therefore, $L \propto R^2 T \propto R^{2-q}$. We want to compare our results with previous work. [Andrews and Williams, 2007] measured the q value for a sample 24 protoplanetary disks around T Tauri stars in the Taurus-Auriga and Ophiuchus-Scorpius star-forming regions and find a value of $q \approx 0.6 \pm 0.1$.
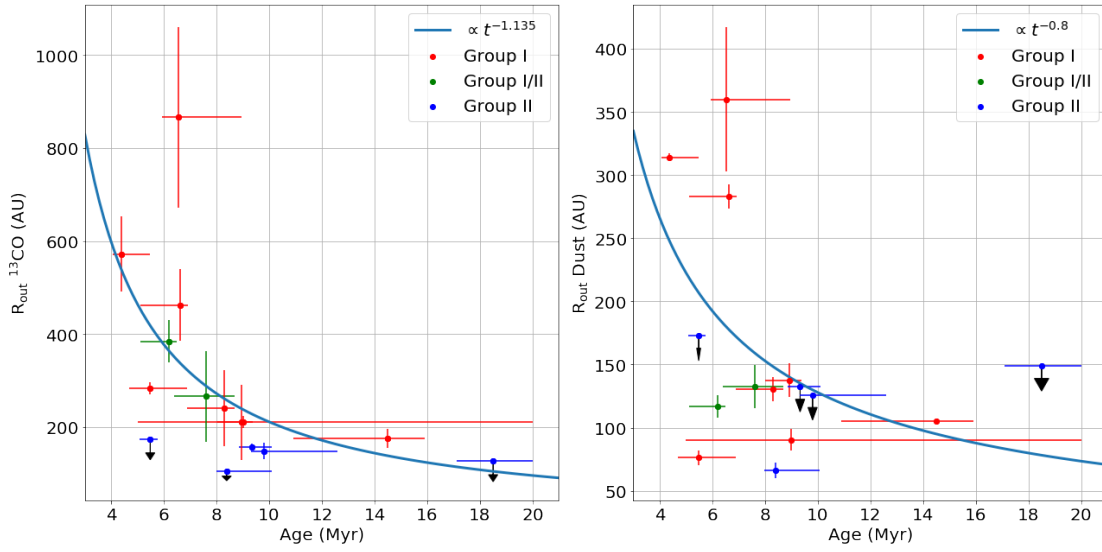
Figure 4.2: Outer disk radii versus age; A power law fit is shown. Black arrows represent upper limits on the outer disk radii estimates.
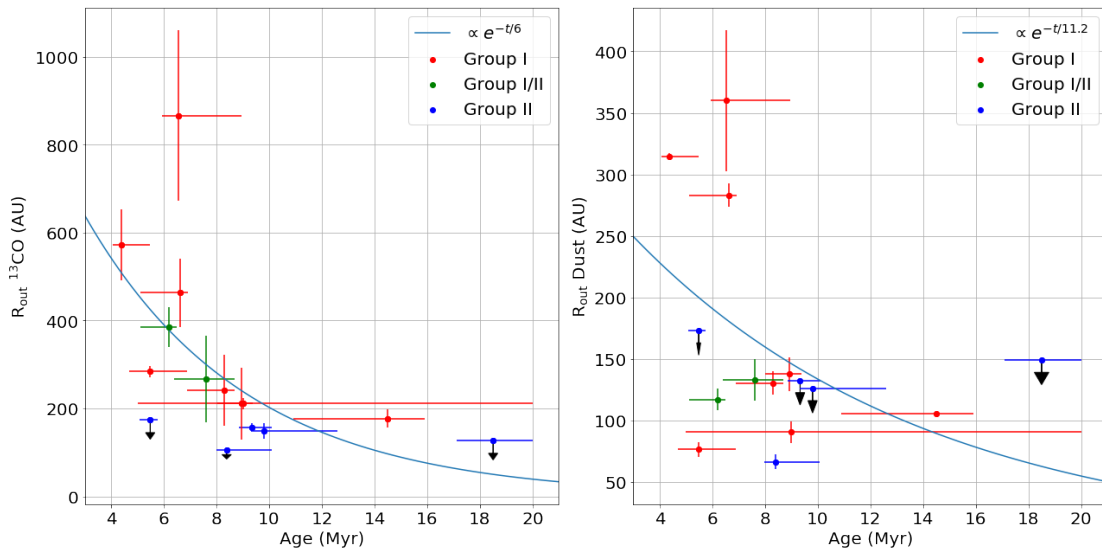
Figure 4.3: Outer disk radii versus age; An exponential law fit is shown. Black arrows represent upper limits on the outer disk radii estimates.

They use the visibilities of the continuum emission from radially resolved sources and fit a power law to derive the q value for each source. We use this study on T Tauri stars because there is no such study yet on a large sample of Herbig Ae/Be stars. Our approach is different beacuse we use the ^{13}CO luminosity of disks with different sizes to infer an average temperature profile gradient. In Figure 4.4, we show the luminosity versus outer disk radii for both gas and dust. We fit a power law of the form $L = aR^{b}$ in the ^{13}CO plot and find $\propto R^{1.3\pm0.16}$. My fit results in a q value of $q = 0.7 \pm 0.16$, which is in good agreement with the value from [Andrews and Williams, 2007], given the one σ uncertainty. However, this simple model seems to fail at fitting the lower end where the Group II disks are located and one Group I. Since these disks are small and faint, the gas content might be low and the ^{13}CO would be optically thin and therefore, our assumptions would not apply to this case.

In addition, it can be see that there is a clear separation between Group I and Group II in the ^{13}CO luminosity, where Group I disks are brighter than Group II. For the dust, it is not yet clear if any correlation with R_{out} is present since, as previously mentioned, the dust is optically thin and its luminosity is the product of the opacity, dust mass and temperature. [Garufi et al., 2017] finds a separation between the two groups, where Group II disks are fainter in 1.3mm flux than Group I disks. This is not case for our sample. The sample overlap between [Garufi et al., 2017] and this work is substantial but not complete, therefore is not yet clear if a trend is present. To be able to shed light on this issue, a complete and coherent study of all Herbig Ae/Be stars is needed.
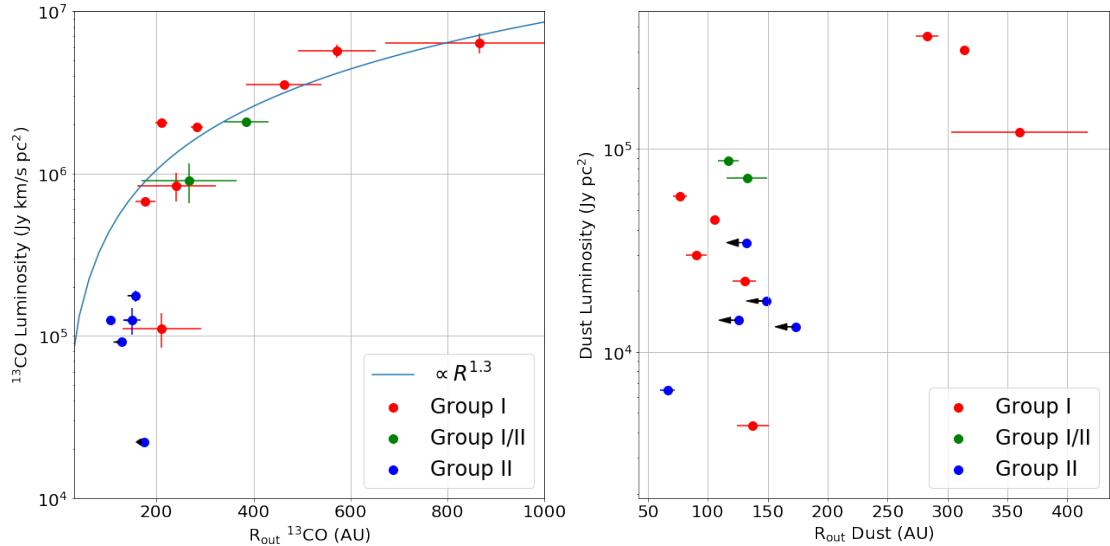
Figure 4.4: Luminosity versus outer disk radii; A power law fit is shown for the ^{13}CO luminosity. Black arrows represent upper limits on the outer disk radii estimates.

4.4   Binarity

Out of all known Herbig Ae/Be stars, more than half are binary systems [Duchêne, 2015]. Since only a limited number of targeted surveys [Wheelwright et al., 2010] have been done on the binarity of Herbig Ae/Be stars, the real number might be even larger. We acquire binary separation

Source	Group	Separation (AU)
HD 34282	I	<30 [Wheelwright et al., 2010]
HD 142527	I	14 [Christiaens et al., 2018]
HD 36112	I	370 [Thomas et al., 2007]
HD 135344B	I	21 [Varga et al., 2018]
AK Sco	II	0.12 [Alecian et al., 2013]
HD 145718	II	20 [Friedemann et al., 1996]
HD 104237	II	150 [Danks et al., 2001]
KK Oph	II	331 [Carmona et al., 2007]

Table 4.1: Binary separation. Distance measurement from [Gaia Collaboration, 2018] were used to transform from " to AU.

from the literature for our sample (see Table 4.1) and find that for Group I sources, half have a companion while out of 5 Group II sources, only one does not. In Figure 4.5, we repeat the Gas versus Dust outer disk radii plot but we mark the binaries depending on the separation: the narrow binaries, located inside the circumbinary disk at separations <30-40 AU and wide binaries located outside the disk at separations >100 AU. In the case of wide binaries, at least one of them has disk, if not both. In [Garufi et al., 2017], they state that Group I disks with companions are smaller than those without, opposite to our case, where 3 out of 4 Group I non-binary systems are smaller than those that have a companion. It is not yet clear if companions play a major role in creating a dichotomy between the two Groups. Future investigations are needed.
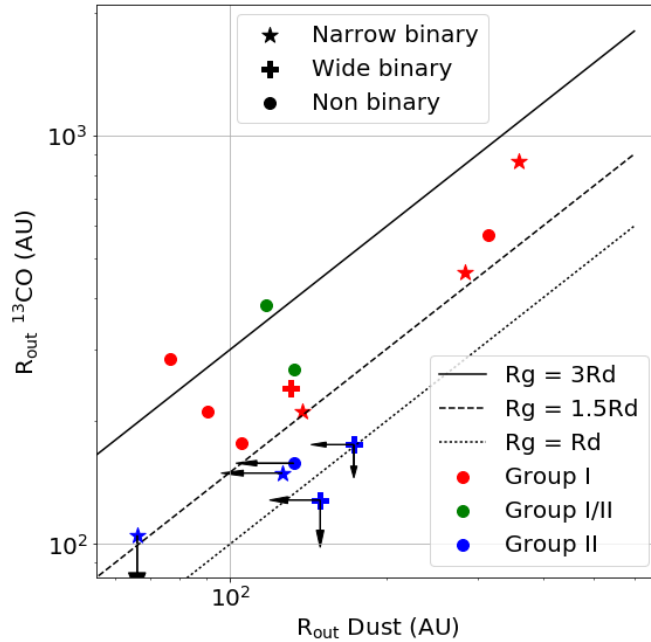
Figure 4.5: Gas versus Dust Outer Disk Radii with binary systems marked. Narrow binaries are located inside the circumbinary disk (<30-40 AU) while wide binaries have larger separations (>100 AU). A log-log scale is used for a clearer view.

4.5 Evolutionary scenarios

In general, we found that Group I disks span a large range in dust (90∼370 AU) and gas (180∼850 AU) outer disk radii while Group II disks are small, with 4 unresolved dust disks and 3 unresolved ^{13}CO gas disks. We also have the Group I/II disks which have similar sub-mm properties (gas outer radii and, continuum and CO flux) with Group I disks.

We divide the Group I disks by their size into two categories: the small (sGI) and the large (lGI) disks. The sGI disks are closer in size to GII disks. Nonetheless, the ^{13}CO radial extent seems to be larger in sGIs, while the dust radial extent cannot be compared since 4 GII disks are not resolved. Also, the ages of sGIs are covering a broad interval (from 5 to 10 Myr), similar to GII disks. Given these findings, it is unlikely that a GII disk would evolve into a sGI.

The GI/II disks in our sample (see HD 169142 & HD 31648) have extended CO emission, strong continuum flux, are relatively young (≈7 Myr) and have low scattered light emission. These disks can be interpreted as massive disks with no inner gap. If an object (e.g. planet) carves an inner hole, these disks might evolve into a sGI disk. The lGI disks are the three outliers in Figure 4.1 that have gas and dust outer radii larger than 300 AU. These disks appear to be distinct from the rest of the sample due to their large radii and fluxes. These lGI disks are also very young (<7 Myr). Either these disks follow a separate evolutionary track and can be separated from their smaller counterparts (sGI) or we are missing in our sample the intermediate GI disks that would fill the gap in terms of radial extent and, continuum and line fluxes.

We compare our results with the current view proposed by [Garufi et al., 2017] (see Figure 4.5). They divide the GII disks in three categories, the small and very small GII disks (which are the GII disks in this thesis) and the shadowed GII disks (which are the GI/II disks in this thesis). [Garufi et al., 2017] describes these GI/II disks to have (from SPHERE) low scattered light emission (GII feature, see Figure 4.6) but very high millimeter flux and extended sub-mm CO emission (GI feature). They interpret them as massive disks with no inner gap that can evolve into a GI which is similar to what we find. However, they only have one Group I/II disk in their sample (HD 163296), while we have an additional one, HD 31648. In terms of GI disks, they do not make any statement about a potential division between sGIs and lGIs. [Garufi et al., 2017] describes the GII disks as being small, which is analogous to our findings, however we cannot make any statement about the subdivison of GII disks into small and very small. [Garufi et al., 2017] states that the very small GII disks have undetected sub-mm CO, however all of our 5 Group II disks have a >3σ sub-mm CO detection. Nonetheless, the main issue is that the very small GII disks in [Garufi et al., 2017] sample are HD 150193 and HD 144668 which are not part of our sample. Therefore, for future studies, we would need to build a coherent sample from this work and [Garufi et al., 2017], as well as new objects if observations become available.

4.6 Future prospects

In the recent years, many improvements have been done in our understanding of the processes that play a role in the evolution of protoplanetary disks, however we are far from having a complete picture. We have shown that the number of protoplanetary disks observations around Herbig Ae/Be stars in the ALMA archive is not enough to draw any conclusions with large statistical significance. Issues with the ALMA archival data is that, on one hand, most of the observations are biased towards Group I disks which are brighter and on the other hand, the aim of these observations is usually to resolve the ring-like structures in the dust disk which involve very small beam size (few 10s of AU). In the case of a very small beam size, the continuum will have a relatively good SNR even with short integration times, however the gas will require longer integration times to achieve a similar SNR. Ideally, we would like to detect all three isotopologues
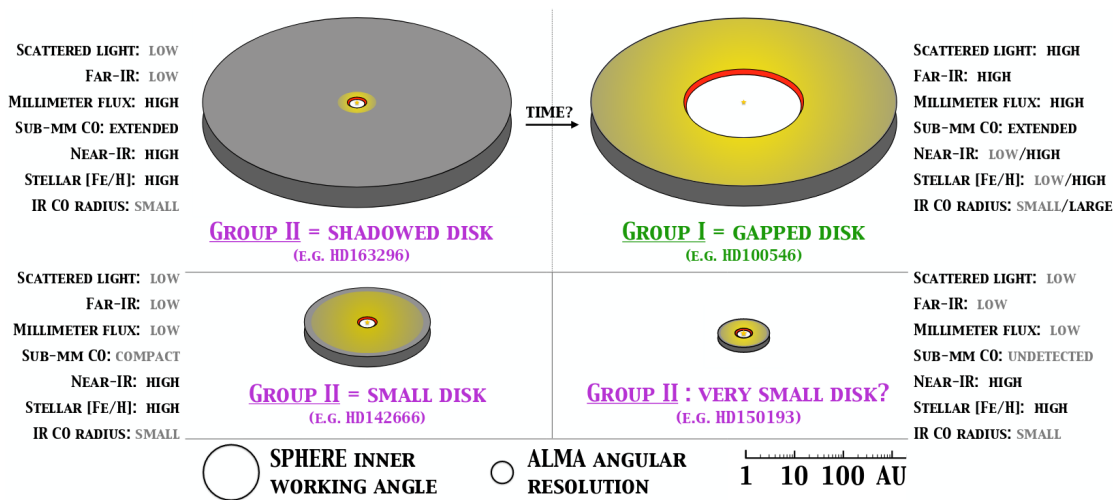
Figure 4.6: Taken from [Garufi et al., 2017] Figure 7: Summary of the properties of the sources analyzed in [Garufi et al., 2017] paper. The proposed disk geometries are shown in logarithmic scale. The SPHERE inner working angle is imposed by the angular resolution of observations in the near-IR (∼10 AU for sources at ∼150 pc). The ALMA angular resolution of ∼3 AU is achieved with the longest possible baselines, which should be used to resolve potentially very small disks.

of CO, to use ^{13}CO to understand the shape of the outer gas edge and then compare with the dust and ^{12}CO to detect possible signatures of truncation, dust radial drift or viscous spreading [Birnstiel and Andrews, 2014, Woitke et al., 2016]. Furthermore, even if the SNR is small, line fluxes of ^{13}CO and C^{18}O can be used to estimate the gas mass [Miotello et al., 2017]. For Group II disks, resolved observations of dust are necessary to check for gaps and presence of rings.

Therefore, as part of this research project, an ALMA proposal was submitted with the goal of gathering better data, especially on Group II disks where we have shown that they are mostly spatially unresolved. The proposal was unfortunately rejected. From our selection of Group II sources, a majority have a close companion at similar separations and would introduce a bias in the sample. However, there are very few Group II sources that have been observed with ALMA and we have shown that on average, these objects are small and faint. Without any prior knowledge of the fluxes and sizes of these disks, it is difficult to determine what angular resolutions and integration times are required to detect and resolve these objects. Thus, it is challenging to propose new Group II Herbigs for observations.

Nonetheless, the need for a large and as homogeneous as possible sample of Herbig Ae/Be stars is crucial. Not only ALMA observations, as previously mentioned, but also near-IR and far-IR data to untangle the entire thermal and physical structure of the disks. Moreover, the age determination of stars will be improved using asteroseismology [Soderblom et al., 2014], however this method requires very high sensitivity which is difficult to achieve at the moment but GAIA offers promising results in the next years. Finally, we are far from having a complete picture of protoplanetary disks evolution and how they result in a variety of planetary systems. If we want to achieve this, observations of disks should be less biased towards nearby bright objects.

Chapter 5

Conclusion

Recent observations on exoplanets have shown that there are a multitude of planetary systems that differ greatly from ours. To understand what are the various mechanisms that design the diversity in the planetary systems, we have to look at the earlier stages, the protoplanetary disks, and follow their evolution. The first evolutionary track proposed for protoplanetary disks around Herbig Ae/Be stars has been the evolution from a flared disk (Group I) into a flat disk (Group II) [Meeus et al., 2001]. However, this scenario has been dismissed since it was found [Maaskant et al., 2013] that Group I disks have a large inner cavity while Group II do not, which discards the evolution from a Group I into a Group II. In this thesis, we have defined a sample of dust and gas observations of protoplanetary disks around Herbig Ae/Be stars using the ALMA Archive and measured the outer radii and the fluxes for the continuum and the ^{13}CO line. From the analysis of the disks, the following conclusions can be drawn:

1. Group I disks

   (a) Mostly resolved in both gas and dust

   (b) Disks span a wide range of radii but have a gap in sizes (200-300 AU in dust & 300-400 in ^{13}CO). We divide them into small Group Is and large Group Is

2. Group II disks

   (a) 3 disks unresolved in ^{13}CO gas and 4 unresolved in dust

   (b) Continuum and line fluxes on average smaller than Group I

   (c) Very small radii (<150 AU)

3. Group I/II disks

   (a) Resolved in both gas and dust

   (b) Similar in size with small Group I, but higher continuum and line fluxes

After comparing our results with [Garufi et al., 2017], we have found that Group II disks are indeed small, on average smaller than sGIs, and have continuum and line fluxes lower than sGIs. Moreover, both groups span a wide range in ages and therefore, we conclude that an evolution from a Group II into a small Group I is very unlikely. However, the Group I/II disks are yound and show similar sub-mm radial extent and fluxes with the sGI disks but have low scattered light emission which is a feature of Group II. These Group I/II disks can be interpreted as relatively large disks with no inner gap. If a planet carves an inner gap, then it is possible that these disks

might evolve into a sGI. Concerning the large Group I disks, it is not yet clear if they belong to another category of disks or we miss, in our sample, the intermediate Group I disks that would create a link between the sGI and lGI disks. Nonetheless, the amount of data available, especially on the small and faint objects, is too low to draw any significant conclusions at this moment. For the future, we hope that the focus will be shifted on observing these fainter and less extended objects since it represents a key aspect in our understanding of protoplanetary disks evolution into the wide variety of planetary systems.

Appendix A

Appendix

A.1 Aperture Photometry Script

```python
import os
import sys
import glob
import numpy as np
#CRTF
dist = 117 #pc
step=0.03
pa=5
i=13 #degrees
ratio = np.sqrt(1-np.sin(np.pi*i/180)**2)
start=0.005
num=250
box=[]
ds9_region=['# Region file format: DS9 version 4.1']
ds9_region.append('global color=green dashlist=8 3 width=1 font="helvetica 10
    normal roman" select=1 highlite=1 dash=0 fixed=0 edit=1 move=1 delete=1
    include=1 source=1')
ds9_region.append('fk5')
region = ['#CRTFv0','global color=blue, coord=J2000']
radii = []
for aper in range(num):
    bmaj = start+step*aper
    bmin = ratio*bmaj
    item = 'ellipse[[18h24m29.776s, -29d46m49.964s], [{}arcsec, {}arcsec], {}deg]'
    .format(bmaj,bmin,pa)
    item2= 'fk5;ellipse (18:24:29.776, -29:46:49.91, {}" ,{}" , {})'.format(bmaj,
    bmin,pa)
    box.append(item)
    region.append(item)
    radii.append(bmaj*dist) #AU
    ds9_region.append(item2)
    print(item)

story = '\n'.join(region)
story2 = '\n'.join(ds9_region)
f = open('regions.txt','w')
f.write(story)
f.close()
f = open('ds9regions.tpl','w')
f.write(story2)
```

```
1036  f.close()

1038  results_12co=[]
      results_13co=[]
1040  results_c18o=[]
      results_cont=[]
1042  for A in range(num):
          fit1=imstat(imagename='12co.fits',region=box[A])
1044      fit2=imstat(imagename='13co.fits',region=box[A])
          fit3=imstat(imagename='18co.fits',region=box[A])
1046      fit4=imstat(imagename='cont.fits',region=box[A])
          try:
1048          results_12co.append(fit1['flux'][0])
              results_13co.append(fit2['flux'][0])
1050          results_c18o.append(fit3['flux'][0])
              results_cont.append(fit4['flux'][0])
1052          print(radii[A],'AU',fit1['flux'][0],fit2['flux'][0],fit3['flux'][0],fit4['
      flux'][0])
          except:
1054          pass

1056  np.savetxt('results_12co.txt',results_12co)
      np.savetxt('results_13co.txt',results_13co)
1058  np.savetxt('results_18co.txt',results_c18o)
      np.savetxt('results_cont.txt',results_cont)
1060  np.savetxt('radii.txt',radii)
```

A.2   90% Flux Uncertainty Script

```
1000  #Script that calculates the error in the flux
      region = ['#CRTFv0','global color=blue, coord=J2000']
1002  ds9_region=['# Region file format: DS9 version 4.1']
      ds9_region.append('global color=green dashlist=8 3 width=1 font="helvetica 10
          normal roman" select=1 highlite=1 dash=0 fixed=0 edit=1 move=1 delete=1
          include=1 source=1')
1004  ds9_region.append('fk5')
      # Inputs
1006  dist = 117 #pc
      r_out = 211 #Au
1008  pa = 5 # deg
      bmaj = r_out/dist
1010  i=13 #degrees
      r = np.sqrt(1-np.sin(np.pi*i/180)**2)
1012  bmin = bmaj * r
      beam_area = 84.04 # in pixels
1014  rms = 3.74e-3 # In Jy/beam or Jy/beam * km/s

1016  ellipse = 'ellipse[[18h24m29.776s, -29d46m49.91s], [{}arcsec, {}arcsec], {}deg]'.
          format(bmaj,bmin,pa)
      ds9= 'fk5;ellipse (18:24:29.776, -29:46:49.91, {}" ,{}" , {})'.format(bmaj,bmin,pa
          )
1018  region.append(ellipse)
      ds9_region.append(ds9)
1020
      save = '\n'.join(region)
1022  f = open('r_outg.txt','w')
      f.write(save)
```

```
1024  f.close()

1026  story2 = '\n'.join(ds9_region)
      f = open('ds9region_g.tpl','w')
1028  f.write(story2)
      f.close()

1030
      fit=imstat(imagename='13co.fits',region=ellipse)
1032  print(ellipse)
      N_pts = fit['npts'][0]
1034  print(N_pts)
      flux_error = N_pts/beam_area * rms
1036  print(flux_error)
```

Bibliography

[Adachi et al., 1976] Adachi, I., Hayashi, C., and Nakazawa, K. (1976). The gas drag effect on the elliptical motion of a solid body in the primordial solar nebula. *Progress of Theoretical Physics*, 56:1756–1771.

[Alecian et al., 2013] Alecian, E., Wade, G. A., Catala, C., Grunhut, J. H., Landstreet, J. D., Bagnulo, S., Böhm, T., Folsom, C. P., Marsden, S., and Waite, I. (2013). A high-resolution spectropolarimetric survey of Herbig Ae/Be stars - I. Observations and measurements. , 429(2):1001–1026.

[Andrews, 2015] Andrews, S. M. (2015). Observations of Solids in Protoplanetary Disks. , 127(956):961.

[Andrews and Williams, 2007] Andrews, S. M. and Williams, J. P. (2007). High-Resolution Submillimeter Constraints on Circumstellar Disk Structure. , 659(1):705–728.

[Ansdell et al., 2018] Ansdell, M., Williams, J. P., Trapman, L., van Terwisga, S. E., Facchini, S., Manara, C. F., van der Marel, N., Miotello, A., Tazzari, M., Hogerheijde, M., Guidi, G., Testi, L., and van Dishoeck, E. F. (2018). ALMA Survey of Lupus Protoplanetary Disks. II. Gas Disk Radii. , 859(1):21.

[Armitage, 2010] Armitage, P. J. (2010). *Astrophysics of Planet Formation.*

[Bary et al., 2000] Bary, J. S., Weintraub, D. A., and Kastner, J. H. (2000). Detections of Ro-vibrational H_2 Emission from T Tauri Stars. In *American Astronomical Society Meeting Abstracts*, volume 197, page 10.14.

[Bary et al., 2002] Bary, J. S., Weintraub, D. A., and Kastner, J. H. (2002). Detection of Molecular Hydrogen Orbiting a "Naked" T Tauri Star. , 576(1):L73–L76.

[Bary et al., 2003] Bary, J. S., Weintraub, D. A., Kastner, J. H., and Shukla, S. J. (2003). Quiescent Ro-vibrational H_2 Emission from Classical and Weak-line T Tauri Stars. In *American Astronomical Society Meeting Abstracts*, volume 203, page 147.06.

[Bary et al., 2008] Bary, J. S., Weintraub, D. A., Shukla, S. J., Leisenring, J. M., and Kastner, J. H. (2008). Quiescent H_2 Emission From Pre-Main-Sequence Stars in Chamaeleon I. , 678(2):1088–1098.

[Birnstiel and Andrews, 2014] Birnstiel, T. and Andrews, S. M. (2014). On the Outer Edges of Protoplanetary Dust Disks. , 780(2):153.

[Birnstiel et al., 2009] Birnstiel, T., Dullemond, C. P., and Brauer, F. (2009). Dust retention in protoplanetary disks. , 503(1):L5–L8.

[Blake and Boogert, 2004] Blake, G. A. and Boogert, A. C. A. (2004). High-Resolution 4.7 Micron Keck/NIRSPEC Spectroscopy of the CO Emission from the Disks Surrounding Herbig Ae Stars. , 606(1):L73–L76.

[Brandl and IRS Team, 2001] Brandl, B. and IRS Team (2001). Science with SIRTF - Some Examples. In Montmerle, T. and André, P., editors, *From Darkness to Light: Origin and Evolution of Young Stellar Clusters*, volume 243 of *Astronomical Society of the Pacific Conference Series*, page 409.

[Brauer et al., 2008] Brauer, F., Dullemond, C. P., and Henning, T. (2008). Coagulation, fragmentation and radial motion of solid particles in protoplanetary disks. , 480(3):859–877.

[Brittain et al., 2013] Brittain, S. D., Najita, J. R., Carr, J. S., Liskowsky, J., Troutman, M. R., and Doppmann, G. W. (2013). High-resolution Near-infrared Spectroscopy of HD 100546. II. Analysis of Variable Rovibrational CO Emission Lines. , 767(2):159.

[Brittain et al., 2007] Brittain, S. D., Simon, T., Najita, J. R., and Rettig, T. W. (2007). Warm Gas in the Inner Disks around Young Intermediate-Mass Stars. , 659(1):685–704.

[Calvet et al., 1991] Calvet, N., Patino, A., Magris, G. C., and D'Alessio, P. (1991). Irradiation of Accretion Disks around Young Objects. I. Near-Infrared CO Bands. , 380:617.

[Carmona, 2010] Carmona, A. (2010). Observational Diagnostics of Gas in Protoplanetary Disks. *Earth Moon and Planets*, 106(2-4):71–95.

[Carmona et al., 2007] Carmona, A., van den Ancker, M. E., Henning, T., Goto, M., Fedele, D., and Stecklum, B. (2007). A search for near-infrared molecular hydrogen emission in the CTTS LkHα 264 and the debris disk 49 Ceti. , 476(2):853–862.

[Carmona et al., 2011] Carmona, A., van der Plas, G., van den Ancker, M. E., Audard, M., Waters, L. B. F. M., Fedele, D., Acke, B., and Pantin, E. (2011). A survey for near-infrared H_2 emission in Herbig Ae/Be stars: emission from the outer disks of HD 97048 and HD 100546. , 533:A39.

[Chiang and Goldreich, 1997] Chiang, E. I. and Goldreich, P. (1997). Spectral Energy Distributions of T Tauri Stars with Passive Circumstellar Disks. , 490(1):368–376.

[Christiaens et al., 2018] Christiaens, V., Casassus, S., Absil, O., Kimeswenger, S., Gomez Gonzalez, C. A., Girard, J., Ramírez, R., Wertz, O., Zurlo, A., Wahhaj, Z., Flores, C., Salinas, V., Jordán, A., and Mawet, D. (2018). Characterization of low-mass companion HD 142527 B. , 617:A37.

[Comerón, 2008] Comerón, F. (2008). *The Lupus Clouds*, volume 5, page 295.

[D'Alessio et al., 1998] D'Alessio, P., Cantö, J., Calvet, N., and Lizano, S. (1998). Accretion Disks around Young Objects. I. The Detailed Vertical Structure. , 500(1):411–427.

[Danks et al., 2001] Danks, A., Vieira, G., Grady, C., Woodgate, B., Brown, A., Harper, G., Wilkinson, E., Herczeg, C., Sitko, M., Bauer, A., and Biggs, J. (2001). The Environment and Wind of the Herbig Ae Star HD 104237: HST/STIS Coronagraphic Imaging and HST/STIS and FUSE FUV spectroscopy. In *American Astronomical Society Meeting Abstracts*, volume 199, page 60.14.

[de Gregorio-Monsalvo et al., 2013] de Gregorio-Monsalvo, I., Ménard, F., Dent, W., Pinte, C., López, C., Klaassen, P., Hales, A., Cortés, P., Rawlings, M. G., Tachihara, K., Testi, L., Takahashi, S., Chapillon, E., Mathews, G., Juhasz, A., Akiyama, E., Higuchi, A. E., Saito, M., Nyman, L. Å., Phillips, N., Rodón, J., Corder, S., and Van Kempen, T. (2013). Unveiling the gas-and-dust disk structure in HD 163296 using ALMA observations. , 557:A133.

[Dent et al., 2005] Dent, W. R. F., Greaves, J. S., and Coulson, I. M. (2005). CO emission from discs around isolated HAeBe and Vega-excess stars. , 359(2):663–676.

[Dominik, 2015a] Dominik, C. (2015a). Disk evolution: dust and gas. In *European Physical Journal Web of Conferences*, volume 102, page 00004.

[Dominik, 2015b] Dominik, C. (2015b). Disk formation and structure. In *European Physical Journal Web of Conferences*, volume 102, page 00002.

[Draine, 2003] Draine, B. T. (2003). Interstellar Dust Grains. , 41:241–289.

[Dubrulle et al., 1995] Dubrulle, B., Morfill, G., and Sterzik, M. (1995). The dust subdisk in the protoplanetary nebula. , 114(2):237–246.

[Duchêne, 2015] Duchêne, G. (2015). Herbig AeBe stars: multiplicity and consequences. , 355(2):291–301.

[Dullemond and Dominik, 2004] Dullemond, C. P. and Dominik, C. (2004). The effect of dust settling on the appearance of protoplanetary disks. , 421:1075–1086.

[Dutrey et al., 1998] Dutrey, A., Guilloteau, S., Prato, L., Simon, M., Duvert, G., Schuster, K., and Menard, F. (1998). CO study of the GM Aurigae Keplerian disk. , 338:L63–L66.

[Eiroa et al., 2002] Eiroa, C., Oudmaijer, R. D., Davies, J. K., de Winter, D., Garzón, F., Palacios, J., Alberdi, A., Ferlet, R., Grady, C. A., Collier Cameron, A., Deeg, H. J., Harris, A. W., Horne, K., Merín, B., Miranda, L. F., Montesinos, B., Mora, A., Penny, A., Quirrenbach, A., Rauer, H., Schneider, J., Solano, E., Tsapras, Y., and Wesselius, P. R. (2002). On the simultaneous optical and near-infrared variability of pre-main sequence stars. , 384:1038–1049.

[Espaillat et al., 2014] Espaillat, C., Muzerolle, J., Najita, J., Andrews, S., Zhu, Z., Calvet, N., Kraus, S., Hashimoto, J., Kraus, A., and D'Alessio, P. (2014). An Observational Perspective of Transitional Disks. In Beuther, H., Klessen, R. S., Dullemond, C. P., and Henning, T., editors, *Protostars and Planets VI*, page 497.

[Fedele et al., 2017] Fedele, D., Carney, M., Hogerheijde, M. R., Walsh, C., Miotello, A., Klaassen, P., Bruderer, S., Henning, T., and van Dishoeck, E. F. (2017). ALMA unveils rings and gaps in the protoplanetary system <ASTROBJ>HD 169142</ASTROBJ>: signatures of two giant protoplanets. , 600:A72.

[Friedemann et al., 1996] Friedemann, C., Guertler, J., and Loewe, M. (1996). Eclipsing binaries as IRAS sources. , 117:205–225.

[Gaia Collaboration, 2018] Gaia Collaboration (2018). VizieR Online Data Catalog: Gaia DR2 (Gaia Collaboration, 2018). *VizieR Online Data Catalog*, page I/345.

[Garufi et al., 2017] Garufi, A., Meeus, G., Benisty, M., Quanz, S. P., Banzatti, A., Kama, M., Canovas, H., Eiroa, C., Schmid, H. M., Stolker, T., Pohl, A., Rigliaco, E., Ménard, F., Meyer, M. R., van Boekel, R., and Dominik, C. (2017). Evolution of protoplanetary disks from their taxonomy in scattered light: Group I vs. Group II. , 603:A21.

[Gillon et al., 2017] Gillon, M., Triaud, A. H. M. J., Demory, B.-O., Jehin, E., Agol, E., Deck, K. M., Lederer, S. M., de Wit, J., Burdanov, A., Ingalls, J. G., Bolmont, E., Leconte, J., Raymond, S. N., Selsis, F., Turbet, M., Barkaoui, K., Burgasser, A., Burleigh, M. R., Carey, S. J., Chaushev, A., Copperwheat, C. M., Delrez, L., Fernand es, C. S., Holdsworth, D. L., Kotze, E. J., Van Grootel, V., Almleaky, Y., Benkhaldoun, Z., Magain, P., and Queloz, D. (2017). Seven temperate terrestrial planets around the nearby ultracool dwarf star TRAPPIST-1. , 542(7642):456–460.

[Guilloteau et al., 2013] Guilloteau, S., Di Folco, E., Dutrey, A., Simon, M., Grosso, N., and Piétu, V. (2013). A sensitive survey for ^{13}CO, CN, H$_2$CO, and SO in the disks of T Tauri and Herbig Ae stars. , 549:A92.

[Guilloteau and Dutrey, 1998] Guilloteau, S. and Dutrey, A. (1998). Physical parameters of the Keplerian protoplanetary disk of DM Tauri. , 339:467–476.

[Hein-Bertelsen, 2015] Hein-Bertelsen, R. (2015). CO ro-vibrational emission. .

[Hein Bertelsen et al., 2014] Hein Bertelsen, R. P., Kamp, I., Goto, M., van der Plas, G., Thi, W. F., Waters, L. B. F. M., van den Ancker, M. E., and Woitke, P. (2014). CO ro-vibrational lines in HD 100546. A search for disc asymmetries and the role of fluorescence. , 561:A102.

[Herbig, 1960] Herbig, G. H. (1960). The Spectra of Be- and Ae-Type Stars Associated with Nebulosity. , 4:337.

[Hillenbrand, 1994] Hillenbrand, L. A. (1994). Isolated Herbig Ae/Be stars: rare examples of individual high-mass star-forming events. In The, P. S., Perez, M. R., and van den Heuvel, E. P. J., editors, *The Nature and Evolutionary Status of Herbig Ae/Be Stars*, volume 62 of *Astronomical Society of the Pacific Conference Series*, page 369.

[Hu et al., 1991] Hu, J. Y., Blondel, P. F. C., Catala, C., Talavera, A., The, P. S., Tjin-A-Djie, H. R. E., and de Winter, D. (1991). IUE observations of the bright Herbig AE star HD 104237. , 248:150.

[Ilee and Greaves, 2015] Ilee, J. D. and Greaves, J. S. (2015). Interferometry and the study of protoplanetary disks. In *European Physical Journal Web of Conferences*, volume 102, page 00009.

[Isella, 2006] Isella, A. (2006). *TUGBoat*, 14(3):342–351.

[Isella et al., 2007] Isella, A., Testi, L., Natta, A., Neri, R., Wilner, D., and Qi, C. (2007). Millimeter imaging of HD 163296: probing the disk structure and kinematics. , 469(1):213–222.

[Juhász et al., 2010] Juhász, A., Bouwman, J., Henning, T., Acke, B., van den Ancker, M. E., Meeus, G., Dominik, C., Min, M., Tielens, A. G. G. M., and Waters, L. B. F. M. (2010). Dust Evolution in Protoplanetary Disks Around Herbig Ae/Be Stars—the Spitzer View. , 721(1):431–455.

[Krijt et al., 2015] Krijt, S., Ormel, C. W., Dominik, C., and Tielens, A. G. G. M. (2015). Erosion and the limits to planetesimal growth. , 574:A83.

[Kusakabe et al., 2012] Kusakabe, N., Grady, C. A., Sitko, M. L., Hashimoto, J., Kudo, T., Fukagawa, M., Muto, T., Wisniewski, J. P., Min, M., Mayama, S., Werren, C., Day, A. N., Beerman, L. C., Lynch, D. K., Russell, R. W., Brafford, S. M., Kuzuhara, M., Brand t, T. D.,

Abe, L., Brandner, W., Carson, J., Egner, S., Feldt, M., Goto, M., Guyon, O., Hayano, Y., Hayashi, M., Hayashi, S. S., Henning, T., Hodapp, K. W., Ishii, M., Iye, M., Janson, M., Kand ori, R., Knapp, G. R., Matsuo, T., McElwain, M. W., Miyama, S., Morino, J. I., Moro-Martin, A., Nishimura, T., Pyo, T. S., Suto, H., Suzuki, R., Takami, M., Takato, N., Terada, H., Thalmann, C., Tomono, D., Turner, E. L., Watanabe, M., Yamada, T., Takami, H., Usuda, T., and Tamura, M. (2012). High-contrast Near-infrared Polarization Imaging of MWC480. , 753(2):153.

[Long et al., 2017] Long, F., Herczeg, G. J., Pascucci, I., Drabek-Maunder, E., Mohanty, S., Testi, L., Apai, D., Hendler, N., Henning, T., Manara, C. F., and Mulders, G. D. (2017). An ALMA Survey of CO Isotopologue Emission from Protoplanetary Disks in Chamaeleon I. , 844(2):99.

[Lynden-Bell and Pringle, 1974] Lynden-Bell, D. and Pringle, J. E. (1974). The evolution of viscous discs and the origin of the nebular variables. , 168:603–637.

[Maaskant et al., 2013] Maaskant, K. M., Honda, M., Waters, L. B. F. M., Tielens, A. G. G. M., Dominik, C., Min, M., Verhoeff, A., Meeus, G., and van den Ancker, M. E. (2013). Identifying gaps in flaring Herbig Ae/Be disks using spatially resolved mid-infrared imaging. Are all group I disks transitional? , 555:A64.

[Maud et al., 2013] Maud, L. T., Hoare, M. G., Gibb, A. G., Shepherd, D., and Indebetouw, R. (2013). High angular resolution millimetre continuum observations and modelling of S140-IRS1. , 428(1):609–624.

[Meeus et al., 2012] Meeus, G., Montesinos, B., Mendigutía, I., Kamp, I., Thi, W. F., Eiroa, C., Grady, C. A., Mathews, G., Sandell, G., Martin-Zaïdi, C., Brittain, S., Dent, W. R. F., Howard, C., Ménard, F., Pinte, C., Roberge, A., Vand enbussche, B., and Williams, J. P. (2012). Observations of Herbig Ae/Be stars with Herschel/PACS. The atomic and molecular contents of their protoplanetary discs. , 544:A78.

[Meeus et al., 2013] Meeus, G., Salyk, C., Bruderer, S., Fedele, D., Maaskant, K., Evans, N. J., van Dishoeck, E. F., Montesinos, B., Herczeg, G., Bouwman, J., Green, J. D., Dominik, C., Henning, T., and Vicente, S. (2013). DIGIT survey of far-infrared lines from protoplanetary discs. II. CO. , 559:A84.

[Meeus et al., 2001] Meeus, G., Waters, L. B. F. M., Bouwman, J., van den Ancker, M. E., Waelkens, C., and Malfait, K. (2001). ISO spectroscopy of circumstellar dust in 14 Herbig Ae/Be systems: Towards an understanding of dust processing. , 365:476–490.

[Miotello et al., 2017] Miotello, A., van Dishoeck, E. F., Williams, J. P., Ansdell, M., Guidi, G., Hogerheijde, M., Manara, C. F., Tazzari, M., Testi, L., van der Marel, N., and van Terwisga, S. (2017). Lupus disks with faint CO isotopologues: low gas/dust or high carbon depletion? , 599:A113.

[Nielsen et al., 2019] Nielsen, E. L., De Rosa, R. J., Macintosh, B., Wang, J. J., Ruffio, J.-B., Chiang, E., Marley, M. S., Saumon, D., Savransky, D., Ammons, S. M., Bailey, V. P., Barman, T., Blain, C., Bulger, J., Burrows, A., Chilcote, J., Cotten, T., Czekala, I., Doyon, R., Duchêne, G., Esposito, T. M., Fabrycky, D., Fitzgerald, M. P., Follette, K. B., Fortney, J. J., Gerard, B. L., Goodsell, S. J., Graham, J. R., Greenbaum, A. Z., Hibon, P., Hinkley, S., Hirsch, L. A., Hom, J., Hung, L.-W., Dawson, R. I., Ingraham, P., Kalas, P., Konopacky, Q., Larkin, J. E., Lee, E. J., Lin, J. W., Maire, J., Marchis, F., Marois, C., Metchev, S., Millar-Blanchaer, M. A., Morzinski, K. M., Oppenheimer, R., Palmer, D., Patience, J., Perrin, M.,

Poyneer, L., Pueyo, L., Rafikov, R. R., Rajan, A., Rameau, J., Rantakyrö, F. T., Ren, B., Schneider, A. C., Sivaramakrishnan, A., Song, I., Soummer, R., Tallis, M., Thomas, S., Ward-Duong, K., and Wolff, S. (2019). The Gemini Planet Imager Exoplanet Survey: Giant Planet and Brown Dwarf Demographics from 10 to 100 au. , 158(1):13.

[Öberg et al., 2010] Öberg, K. I., Qi, C., Fogel, J. K. J., Bergin, E. A., Andrews, S. M., Espaillat, C., van Kempen, T. A., Wilner, D. J., and Pascucci, I. (2010). The Disk Imaging Survey of Chemistry with SMA. I. Taurus Protoplanetary Disk Data. , 720(1):480–493.

[Okuzumi, 2009] Okuzumi, S. (2009). Electric Charging of Dust Aggregates and its Effect on Dust Coagulation in Protoplanetary Disks. , 698(2):1122–1135.

[Oudmaijer et al., 1992] Oudmaijer, R. D., van der Veen, W. E. C. J., Waters, L. B. F. M., Trams, N. R., Waelkens, C., and Engelsman, E. (1992). SAO stars with infrared excess in the IRAS Point Source Catalog. , 96:625–643.

[Panić and Hogerheijde, 2009] Panić, O. and Hogerheijde, M. R. (2009). Characterising discs around Herbig Ae/Be stars through modelling of low-J ^{12}CO lines. , 508(2):707–716.

[Piétu et al., 2007] Piétu, V., Dutrey, A., and Guilloteau, S. (2007). Probing the structure of protoplanetary disks: a comparative study of DM Tau, LkCa 15, and MWC 480. , 467(1):163–178.

[Piétu et al., 2005] Piétu, V., Guilloteau, S., and Dutrey, A. (2005). Sub-arcsec imaging of the AB Aur molecular disk and envelope at millimeter wavelengths: a non Keplerian disk. , 443(3):945–954.

[Raman et al., 2006] Raman, A., Lisanti, M., Wilner, D. J., Qi, C., and Hogerheijde, M. (2006). A Keplerian Disk around the Herbig Ae Star HD 169142. *The Astronomical Journal*, 131(4):2290–2293.

[Rosenfeld et al., 2013] Rosenfeld, K. A., Andrews, S. M., Hughes, A. M., Wilner, D. J., and Qi, C. (2013). A Spatially Resolved Vertical Temperature Gradient in the HD 163296 Disk. , 774(1):16.

[Sandell et al., 2011] Sandell, G., Weintraub, D. A., and Hamidouche, M. (2011). A Submillimeter Mapping Survey of Herbig AeBe Stars. , 727(1):26.

[Segura-Cox et al., 2016] Segura-Cox, D. M., Harris, R. J., Tobin, J. J., Looney, L. W., Li, Z.-Y., Chandler, C., Kratter, K., Dunham, M. M., Sadavoy, S., Perez, L., and Melis, C. (2016). The VLA Nascent Disk and Multiplicity Survey: First Look at Resolved Candidate Disks around Class 0 and I Protostars in the Perseus Molecular Cloud. , 817(2):L14.

[Seizinger et al., 2013] Seizinger, A., Krijt, S., and Kley, W. (2013). Erosion of dust aggregates. , 560:A45.

[Sitko et al., 1994] Sitko, M. L., Halbedel, E. M., Lawrence, G. F., Smith, J. A., and Yanow, K. (1994). Variable Extinction in HD 45677 and the Evolution of Dust Grains in Pre–Main-Sequence Disks. , 432:753.

[Soderblom et al., 2014] Soderblom, D. R., Hillenbrand, L. A., Jeffries, R. D., Mamajek, E. E., and Naylor, T. (2014). Ages of Young Stars. In Beuther, H., Klessen, R. S., Dullemond, C. P., and Henning, T., editors, *Protostars and Planets VI*, page 219.

[Terebey et al., 1984] Terebey, S., Shu, F. H., and Cassen, P. (1984). The collapse of the cores of slowly rotating isothermal clouds. , 286:529–551.

[Thomas et al., 2007] Thomas, S. J., van der Bliek, N. S., Rodgers, B., Doppmann, G., and Bouvier, J. (2007). Multiplicity of Herbig Ae/Be Stars. In Hartkopf, W. I., Harmanec, P., and Guinan, E. F., editors, *Binary Stars as Critical Tools & Tests in Contemporary Astrophysics*, volume 240 of *IAU Symposium*, pages 250–253.

[Tilling et al., 2012] Tilling, I., Woitke, P., Meeus, G., Mora, A., Montesinos, B., Riviere-Marichalar, P., Eiroa, C., Thi, W. F., Isella, A., Roberge, A., Martin-Zaidi, C., Kamp, I., Pinte, C., Sandell, G., Vacca, W. D., Ménard, F., Mendigutía, I., Duchêne, G., Dent, W. R. F., Aresu, G., Meijerink, R., and Spaans, M. (2012). Gas modelling in the disc of HD 163296. , 538:A20.

[Trapman et al., 2019] Trapman, L., Facchini, S., Hogerheijde, M. R., van Dishoeck, E. F., and Bruderer, S. (2019). Gas vs dust sizes of protoplanetary disks: effects of dust evolution. *arXiv e-prints*, page arXiv:1903.06190.

[van den Ancker et al., 2000] van den Ancker, M. E., Bouwman, J., Wesselius, P. R., Waters, L. B. F. M., Dougherty, S. M., and van Dishoeck, E. F. (2000). ISO spectroscopy of circumstellar dust in the Herbig Ae systems AB Aur and HD 163296. , 357:325–329.

[van der Plas et al., 2014] van der Plas, G., Casassus, S., Ménard, F., Perez, S., Thi, W. F., Pinte, C., and Christiaens, V. (2014). Spatially Resolved HCN J = 4-3 and CS J = 7-6 Emission from the Disk around HD 142527. , 792(2):L25.

[van der Plas et al., 2017] van der Plas, G., Wright, C. M., Ménard, F., Casassus, S., Canovas, H., Pinte, C., Maddison, S. T., Maaskant, K., Avenhaus, H., Cieza, L., Perez, S., and Ubach, C. (2017). Cavity and other radial substructures in the disk around HD 97048. *Astronomy and Astrophysics*, 597:A32.

[van der Wiel et al., 2013] van der Wiel, M. H. D., Naylor, D. A., Aresu, G., and Olofsson, G. (2013). Gas signatures of Herbig Ae/Be disks probed with Herschel SPIRE spectroscopy. In *Protostars and Planets VI Posters*.

[van der Wiel et al., 2014] van der Wiel, M. H. D., Naylor, D. A., Kamp, I., Ménard, F., Thi, W. F., Woitke, P., Olofsson, G., Pontoppidan, K. M., Di Francesco, J., Glauser, A. M., Greaves, J. S., and Ivison, R. J. (2014). Signatures of warm carbon monoxide in protoplanetary discs observed with Herschel SPIRE. , 444(4):3911–3925.

[Varga et al., 2018] Varga, J., Ábrahám, P., Chen, L., Ratzka, T., Gabányi, K. É., Kóspál, Á., Matter, A., van Boekel, R., Henning, T., Jaffe, W., Juhász, A., Lopez, B., Menu, J., Moór, A., Mosoni, L., and Sipos, N. (2018). VLTI/MIDI atlas of disks around low- and intermediate-mass young stellar objects. , 617:A83.

[Vioque et al., 2018] Vioque, M., Oudmaijer, R. D., Baines, D., Mendigutía, I., and Pérez-Martínez, R. (2018). Gaia DR2 study of Herbig Ae/Be stars. , 620:A128.

[Waelkens et al., 1998] Waelkens, C., Malfait, K., and Waters, L. B. F. M. (1998). ISO Observations of Isolated Herbig AE/BE Stars. , 255:25–33.

[Waters and Waelkens, 1998] Waters, L. B. F. M. and Waelkens, C. (1998). Herbig Ae/Be Stars. , 36:233–266.

[Weidenschilling, 1977] Weidenschilling, S. J. (1977). Aerodynamics of solid bodies in the solar nebula. , 180:57–70.

[Wheelwright et al., 2010] Wheelwright, H. E., Oudmaijer, R. D., and Goodwin, S. P. (2010). The mass ratio and formation mechanisms of Herbig Ae/Be star binary systems. , 401(2):1199–1218.

[Whipple, 1972] Whipple, F. L. (1972). On certain aerodynamic processes for asteroids and comets. In Elvius, A., editor, *From Plasma to Planet*, page 211.

[Wielen and Wilson, 1997] Wielen, R. and Wilson, T. L. (1997). The evolution of the C, N, and O isotope ratios from an improved comparison of the interstellar medium with the Sun. , 326:139–142.

[Wisniewski et al., 2008] Wisniewski, J. P., Clampin, M., Grady, C. A., Ardila, D. R., Ford, H. C., Golimowski, D. A., Illingworth, G. D., and Krist, J. E. (2008). The HD 163296 Circumstellar Disk in Scattered Light: Evidence of Time-Variable Self-Shadowing. , 682(1):548–558.

[Woitke et al., 2019] Woitke, P., Kamp, I., Antonellini, S., Anthonioz, F., Baldovin-Saveedra, C., Carmona, A., Dionatos, O., Dominik, C., Greaves, J., Güdel, M., Ilee, J. D., Liebhardt, A., Menard, F., Min, M., Pinte, C., Rab, C., Rigon, L., Thi, W. F., Thureau, N., and Waters, L. B. F. M. (2019). Consistent Dust and Gas Models for Protoplanetary Disks. III. Models for Selected Objects from the FP7 DIANA Project. , 131(1000):064301.

[Woitke et al., 2016] Woitke, P., Min, M., Pinte, C., Thi, W. F., Kamp, I., Rab, C., Anthonioz, F., Antonellini, S., Baldovin-Saavedra, C., Carmona, A., Dominik, C., Dionatos, O., Greaves, J., Güdel, M., Ilee, J. D., Liebhart, A., Ménard, F., Rigon, L., Waters, L. B. F. M., Aresu, G., Meijerink, R., and Spaans, M. (2016). Consistent dust and gas models for protoplanetary disks. I. Disk shape, dust settling, opacities, and PAHs. , 586:A103.

[Zsom et al., 2010] Zsom, A., Ormel, C. W., Güttler, C., Blum, J., and Dullemond, C. P. (2010). The outcome of protoplanetary dust growth: pebbles, boulders, or planetesimals? II. Introducing the bouncing barrier. , 513:A57.